Scanning Tunneling Spectroscopy of Subsurface Non-Magnetic Impurities in Copper

Dissertation

zur Erlangung des mathematisch-naturwissenschaftlichen Doktorgrades

"Doctor rerum naturalium"

der Georg-August-Universität Göttingen

im Promotionsprogramm ProPhys

der Georg-August University School of Science (GAUSS)

vorgelegt von

Thomas Ulrich Kotzott

aus Hamburg

Göttingen, 2021

Betreuungsausschuss:

PD Dr. Martin Wenderoth
IV. Physikalisches Institut,
Georg-August-Universität Göttingen

Prof. Dr. Peter E. Blöchl
Institut für Theoretische Physik,
Technische Universität Clausthal-Zellerfeld

Prof. Dr. Christian Jooß
Institut für Materialphysik,
Georg-August-Universität Göttingen

Mitglieder der Prüfungskommission:

Referent:
PD Dr. Martin Wenderoth
IV. Physikalisches Institut,
Georg-August-Universität Göttingen

Korreferent:
Prof. Dr. Christian Jooß
Institut für Materialphysik,
Georg-August-Universität Göttingen

Weitere Mitglieder der Prüfungskommission:
Prof. Dr. Fabian Heidrich-Meisner
Institut für Theoretische Physik,
Georg-August-Universität Göttingen

Prof. Dr. Hans-Christian Hofsäss
II. Physikalisches Institut,
Georg-August-Universität Göttingen

Prof. Dr. Stefan Mathias
I. Physikalisches Institut,
Georg-August-Universität Göttingen

apl. Prof. Dr. Vasily Moshnyaga
I. Physikalisches Institut,
Georg-August-Universität Göttingen

Tag der mündlichen Prüfung: 22. Juli 2021

Contents

Contents

1 Introduction

The electrons close to the Fermi level of a solid contribute crucially to the material's electronic, thermal and magnetic properties. Therefore, manifold methods have been developed to access the band structure experimentally. Quantum oscillation techniques have been used already decades ago to characterize the Fermi surface, e.g. by the de Haas-van Alphen effect [1]. Nowadays, angle-resolved photoemission spectroscopy (ARPES) is applied to a wide range of materials, especially for low dimensional sample systems, and reveals the band structure with high energy and momentum resolution in a broad energy interval constricted to occupied states [2]. A real space access provides the scanning tunneling microscope (STM), that offers to characterize a specific sample position with high spatial resolution and spectroscopy for both occupied and unoccupied states. The dispersion of a metal surface state was obtained by mapping the energy-dependent wavelength of the standing wave pattern formed by scattering from a defect such as a substrate step or adatom [3, 4]. These oscillations are called Friedel oscillations and are the response of the electronic system to a perturbation [5]. The Fourier transform of such a pattern gives insight into the 2D band structure, which is utilized by the quasiparticle interference (QPI) technique [6].

Particularly intriguing are many-body effects, which make it necessary to describe the system beyond a single-particle dispersion. So-called self-energy corrections lead to a renormalization of the band structure. For example, the interaction of electrons with phonons, i.e. lattice vibrations, causes a characteristic kink in the dispersion around the Fermi level. This was first imaged experimentally by ARPES on the Mo(110) surface state [7], and for many other metal surface states characteristic quantities like the electron-phonon coupling parameter λ, the self-energy $\Sigma(\omega)$ and the Eliashberg function $\alpha^2 F(\omega)$ were determined [8, 9]. Also the STM can be used to study such properties of electron-phonon coupling [10–14] and map many-body renormalizations in 2D systems [15, 16]. With QPI even the characteristic kink around the Fermi level was resolved in k-space for the Ag(111) surface state [17].

The spatial resolution of the STM makes it possible to determine the exact environment of where the sample is examined without averaging over different surface domains or defect types, as is the case with ARPES. Furthermore, real space scattering patterns always contain contributions from both the electronic structure as well as the scattering properties of the defect. The easiest example is a scattering phase shift that an electron undergoes due to the scattering process and is included in the square of the wave function $|\psi(\mathbf{r})|^2$ that is probed. In 2D systems, e.g., the scattering phase shifts for a single magnetic Co impurity on the Cu(111) [18] and Ag(111) [19] surface were identified. The combination of both, electron propagation on the surface and scattering at the adatom, determines the pattern on the surface. For an interpretation, these contributions have to be distinguished.

In this thesis, we translate such an experiment into three dimensions. We use an STM to map the real space signature of scattering at a bulk impurity buried below a metal surface. We will show that this yields access to both the scattering properties of the subsurface impurity as well as an insight to the electronic structure of the host, including renormalizations from many-body effects.

The ability of STM to image single subsurface impurities is due to the nanoscale electron focusing effect [20], which leads to directional electron propagation because of anisotropies in the host's band structure. The electrons scattered at the impurity and propagated to the surface interfere there constructively or destructively. They show ring-like interference patterns, which are shown for germanium atoms buried below a Cu(100) surface in Fig. 1.1. The surface signatures of subsurface impurities are Friedel oscillations, yet, they differ in one key aspect from the scattering patterns of a 2D surface state. In 2D, the full scattering pattern is imaged at the surface with multiple oscillations of the same wave. For the 3D experiment, standing wave patterns develop between each point of the surface and the impurity. Hence, the STM measurement at the surface acts like a slice in tomography, because it only maps one point of each Friedel oscillation, but for a different standing wave at each point of the surface.

Electron focusing experiments were first described for single cobalt atoms in copper by Weismann et al. [20]. By probing bulk electrons in such measurements, the anisotropic Fermi surface of Cu could be imaged in real space and later also for the superconductor Pb [21]. Single and dimer magnetic impurities were characterized as atomic Kondo systems, revealing their scattering phase shift and the Abrikosov-Suhl resonance at the Fermi level [22–24].
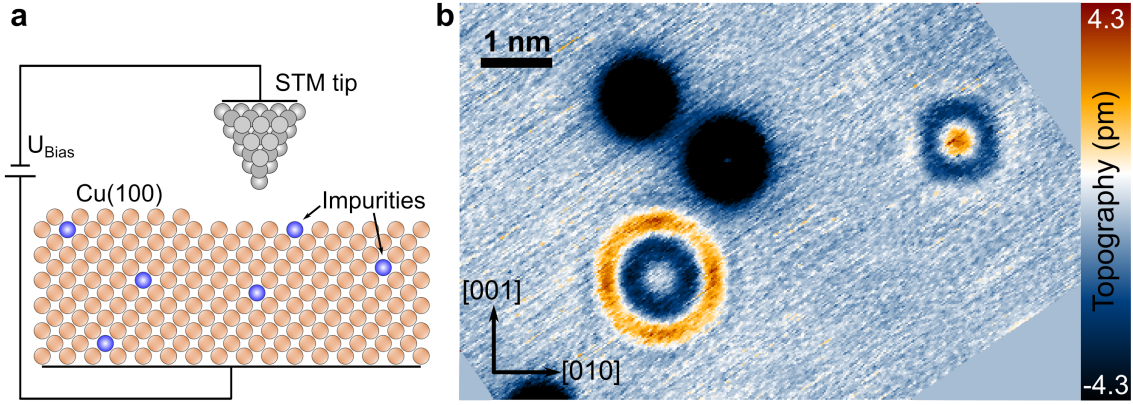
Figure 1.1: (a) Experimental setup with a scanning tunneling microscope probing the surface of a dilute surface alloy. (b) Scanning tunneling topography of subsurface Ge impurities in Cu(100). Spatially extended, oscillating interference patterns are the electron focusing signal from Ge atoms buried six (left) and three (right) layers below the surface, respectively. The dark contrasts depict surface-near impurities. In this thesis, the surface signatures of buried impurities are used to gain insight into the bulk. (Set point: $U_{\mathrm{Bias}} = 0.1\,\mathrm{V}$, $I_{\mathrm{Set}} = 0.4\,\mathrm{nA}$).

Here, we present an electron focusing experiment with non-magnetic impurities buried in Cu(100). Non-magnetic impurities are expected to be spectrally homogeneous with resonances only at species-specific energy levels. Thus, we can determine a scattering phase shift and then functionalize these subsurface defects to study the bulk propagation. For this, we compare impurities of two non-magnetic species to distinguish contributions from the impurities and from the host.

For our study, we choose two unequal impurity species. Germanium with an electronic configuration of $[\mathrm{Ar}]3d^{10}4s^24p^2$ is an sp scatterer and shows a high residual resistivity for dilute Cu-Ge alloys, as predicted in Linde's rule [25]. Yet, structurally it is similar to Cu as it is in the same period of the periodic table and only slightly heavier. We compare the species with silver[1], which is isoelectronic to Cu and also a transition metal with an electronic configuration of $[\mathrm{Kr}]4d^{10}5s^1$. Hence, weak d scattering is expected, but the Ag atom has a $70\,\%$ higher mass and is larger than the host atoms. For a full picture, we describe the data with two theoretical models, namely a plane wave tight-binding model and furthermore ab-initio calculations[2].

---

[1]The data for dilute surface alloys of Ag in Cu(100) were recorded by H. Prüser. The comparison of both non-magnetic species and the analysis with theoretical models was part of this thesis.

[2]The ab-initio calculations in the full potential Korringa-Kohn-Rostoker Green's function method were performed by M. Bouhassoune and S. Lounis at the Forschungszentrum Jülich. In this thesis, these results were discussed and compared to the experimental data acquired.

We find the spectroscopic data of the scattering patterns to be consistent with the overall Cu band structure, also known from previous electron focusing experiments. Additionally, we identify band structure renormalizations around the Fermi level that we attribute to electron-phonon coupling. Corresponding to the characteristic kink in momentum space, we detect a peculiar bending of the interference pattern at zero bias. Implementing a self-energy into the tight-binding model proves to reproduce the features found in the experimental data. Hence, within the interference patterns of buried non-magnetic atoms, we find the real space signature of many-body effects incorporated into the band structure. Using this approach, we can combine the atomic precision and the ability to resolve occupied and unoccupied states of an STM with the characterization of collective excitations within a bulk system by means of a single buried impurity atom.

This thesis is organized as follows, with the respective chapters discussing in depth the topics introduced here in the context of the literature. In Chap. 2, the techniques of scanning tunneling microscopy and spectroscopy are presented. Chap. 3 is dedicated to electron propagation and scattering in Cu. The electron focusing effect and previous experiments for 2D and 3D systems are reviewed, before the Green's function method is introduced with its implementations by the tight-binding model as well as the ab-initio calculations. Furthermore, the contributions of different electronic orbital characters to the focusing patterns are discussed. Finally, the fundamentals of electron-phonon coupling including previous experiments that quantified these many-body effects are presented. In Chap. 4, the sample preparation process of dilute surface alloys is explained. Moreover, the scattering mechanisms that lead to the impurities' residual resistivity are introduced. Subsequently, in Chap. 5, the topographic surface signatures of non-magnetic impurities in Cu(100) are presented. A single effective scattering phase shift is used to describe the patterns of both Ge and Ag and discuss deeply buried impurities. In Chap. 6, the spectroscopic data as real space signature of the host's band structure is examined and compared with the ab-initio calculations. The renormalization around the Fermi level can be described by an electron-phonon coupling parameter, which is discussed in the context of the literature. Finally, the most important findings of this thesis are summarized.

2 Scanning Tunneling Microscopy

The invention of the scanning tunneling microscope (STM) in 1982 revolutionized surface science and the whole field of condensed matter physics [26, 27]. For the first time, structural and electronic information could be recorded simultaneously on the atomic scale. Hence, it just took four years for the Nobel committee to award half of 1986's Nobel prize to Gerd Binnig and Heinrich Rohrer of IBM Zurich 'for their design of the scanning tunneling microscope'. In this thesis, we use as main measuring instrument the surface-sensitive STM, extending its typically known capabilities to exploring 3D bulk properties with atomic resolution.

Over the years, various techniques were implemented into STMs, exceeding 'simple' measurements of structural information by topographies. Scanning tunneling spectroscopy, explained in detail below, offered access to the energy-resolved density of states on the nanometer scale. In inelastic electron tunneling spectroscopy (IETS), sudden changes in the measured local density of states are attributed to inelastic tunneling processes, which reveal the vibrational modes in adsorbed molecules or surface phonon energies [28]. Spin-polarized STM (SP-STM) uses a ferromagnetic tip that favors electrons of a given spin orientation depending on an applied magnetic field [29]. It allows to detect the magnetization of surface structures and, in combination with IETS, enabled the investigation of a single-atom spin-flip on a surface and measuring its Zeeman energy [30]. Over the last decade, different ways to investigate dynamics with an STM were developed via pump-probe measurements. An all-electronic approach, with pump-probe pulses by the bias voltage, could measure the electron spin relaxation time of individual atoms on the surface [31] and paved the way of the field of electron spin resonance (ESR) STM [32] that can characterize atomic magnetism with very high energy resolution. Optically driven pump-probe schemes have to compensate for thermal instabilities due to energy transfer into the junction which were tackled by THz-STM or shaken-pulse-pair-excitation (SPPX) [33–35]. Less common, but not less powerful, is scanning tunneling potentiometry (STP) [36–38] which maps the electrochemical potential at each position of the

sample. By applying an external transport field, transport properties, e.g. of the two-dimensional material graphene, can be investigated [39–41]. STP can also be implemented in multi-tip STM setups where a cross voltage is inserted locally by two additional tips. These, and many more, experimental techniques can be applied by STM which proves to be a versatile tool to investigate a multitude of physical properties on the atomic scale. The atomic force microscope (AFM) that measures a force between tip and sample instead of a tunneling current, opens up even further paths for the investigation of nanostructures [42].

In this chapter, first the basic concepts and theoretical principles of scanning tunneling microscopy including the role of the tip as probe are briefly explained. Consequently, the measurement modes of scanning tunneling microscopy and spectroscopy as well as apparent barrier height are described as they are most relevant for the presented data. Finally, the experimental setups employed in this thesis are briefly introduced.

2.1 Theoretical Principles

Scanning tunneling microscopy is based on the quantum-mechanical tunneling effect. In classical physics, a particle cannot overcome a potential barrier if it has a lower energy than the potential. In quantum mechanics, there is a finite probability that the particle will pass to the other side of barrier. The wave function is only partially reflected and an evanescent wave decays within the potential until it is transmitted through the barrier.

This effect is exploited in an STM. An atomically sharp tip is brought very close to the surface of the sample with a vacuum (or atmosphere) barrier in between. The distance is chosen so small that the wave functions of both sides of the junction overlap. With a bias voltage applied, electrons can tunnel through the barrier creating the tunneling current which is the central quantity of measurement.

In the following, we will outline only briefly the fundamental theoretical principles to describe the tunnel current. For more detailed explanations, please refer to one of the many textbooks that have covered the topic [43–45].

Already in 1961, two decades before the invention of the STM, John Bardeen published calculations for a planar tunneling junction [46]. He introduced a transfer Hamiltonian approach in which a current I_T is generated, when a voltage V is applied

between both sides of the junction:

$$I_T = \frac{2\pi e}{\hbar} \sum_{\mu,\nu} [f(E_\mu) - f(E_\nu)]|M_{\mu\nu}|^2 \delta(E_\nu + eV - E_\mu) \tag{2.1}$$

The transition matrix element $M_{\mu\nu}$ describes the transfer probability between two states for a wave function ψ_μ in the sample and a wave function χ_ν in the tip:

$$\begin{aligned} M_{\mu\nu} &= \langle \chi_\nu | H | \psi_\mu \rangle \\ &= \frac{\hbar^2}{2m} \int_S (\psi_\mu \nabla \chi_\nu^* - \chi_\nu^* \nabla \psi_\mu) \cdot \mathrm{dS} \end{aligned} \tag{2.2}$$

The Fermi distributions f ensure tunneling from an occupied to an empty state while the delta distribution $\delta(E_\nu + eV - E_\mu)$ selects only those pairs of wave functions that interact in an elastic tunneling process.

For small bias voltages V and low temperatures, for which the Fermi distributions are replaced by step functions, the expression for the tunneling current is simplified to

$$I_T = \frac{2\pi}{\hbar} e^2 V \sum_{\mu,\nu} \delta(E_\nu - E_F)\delta(E_\mu - E_F). \tag{2.3}$$

In 1983, Tersoff and Hamann extended Bardeen's theory by introducing an STM experiment's geometry into the calculations. They assumed an *s*-wave function for the tip [47]. With this additional approximation, the tunneling current reads

$$I_T = \sum_\nu |\psi_\nu(\vec{r}_t)|^2 \delta(E_\nu - E_F) := \rho(\vec{r}_t, E_F) \tag{2.4}$$

with $\vec{r}_t$ being the center of the *s*-wave as position of the tip. The tunneling current is given by the sum over all states at the Fermi level of the sample at the spatial position of the tip. This is equivalent to the *Local Density of States* (LDOS) $\rho(\vec{r}_t, E_F)$ of the sample at the tip's location.

Making these theoretical concepts available for other energies than the Fermi level, Hamers employed an integral approach that made use of the Wentzel-Kramers-Brillouin (WKB) approximation [48]. The tunneling current is then given by an integral over all states between the bias voltage V and the Fermi level, i.e., those

states that are available for a tunneling event:

$$I_T = \int_0^{eV} \rho_{\text{sample}}(x, y, E)\rho_{\text{tip}}(-eV + E)T(E, eV, h)\,\mathrm{d}E \tag{2.5}$$

Here, ρ_{tip} denotes the tip density of states and the term ρ_{sample} is the LDOS of the sample for the energy E at the lateral position (x, y) of the sample's surface (z=0). The energy is given in reference to the individual Fermi level with $eV < 0$ for negative sample bias, i.e., when electrons tunnel into the sample. In this expression (Eq. 2.5), the dependence on the tip-sample distance h is included in the tunneling transmission probability T which is approximately given by

$$T(E, eV, h) = \exp\left(-\frac{2\sqrt{2m}}{\hbar} \cdot h \cdot \sqrt{\frac{\phi_{\text{sample}} + \phi_{\text{tip}}}{2} + \frac{eV}{2} - E}\right) \tag{2.6}$$

with the sample's and tip's work functions denoted by ϕ. In this term the exponential dependence of the tunneling current to the tip-sample distance h is obvious. It enables scanning tunneling microscopy to resolve real space structures with picometer resolution.

2.2 Scanning Tunneling Microscopy

2.2.1 Measurement Modes and Data Analysis

The most important part of an STM is the tip which is brought as a probe to a surface with subatomic precision in all spatial directions. At each data point the tunneling current and the position of the tip is recorded. As it is a *scanning* tunneling microscope, the data is acquired by raster-scanning the sample. Line by line a 'profile' of the surface with trace and retrace is recorded.

Two basic measurement modes are available in scanning tunneling microscopy, the constant height and the constant current mode. The constant height mode is simpler, as the tip height is left constant during tip movement in (x, y). In this scheme, the information about the sample is contained in the recorded tunnel current. However, due to the exponential decay of the tunneling current, this mode is only useful on flat surfaces.

More commonly used is the constant current mode. It makes use of a feedback loop that controls the tip's height so that a specific set-point current is obtained.

Depending on the set bias voltage, the height value h is recorded for each surface position (x, y). The resulting topography data is not only given by the surface morphology, but also electronic contrast because of varying LDOS over the surface. A line scan in constant current mode represents a profile of constant LDOS at the position of the tip.
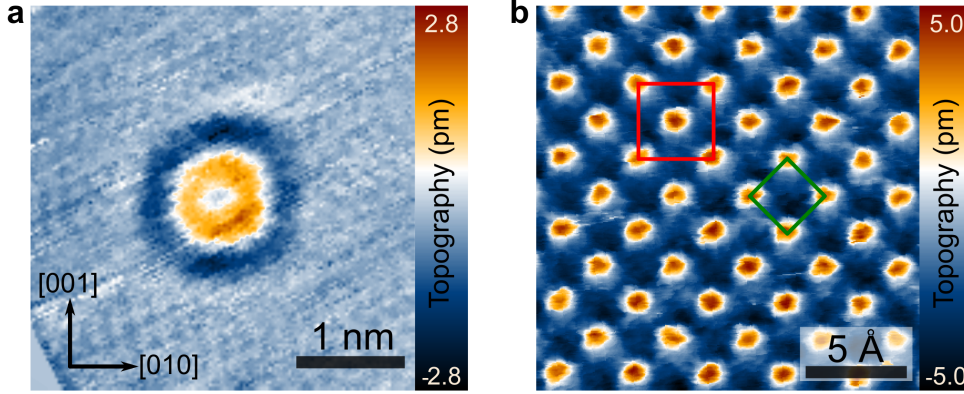

Figure 2.1: STM constant current topographies of Cu(100) surface. (a) Topography of $3.5 \times 3.5\,\text{nm}^2$ with surface signature of a Ge impurity buried in the 5th crystal monolayer below the surface imaged with setpoint ($U = 50\,\text{mV}, I = 300\,\text{pA}$). The sensitivity of an STM is demonstrated by the well-resolved purely electronic contrast of only 2.5 pm in height and laterally by the features' diameter of 1.5 nm. (b) Topography of $1.9 \times 1.9\,\text{nm}^2$ with atomic resolution of the Cu(100) surface. Each bright spot corresponds to one Cu atom. A unit cell of the crystal lattice (red) and the surface lattice (green) are labeled.

An example for STM topography data is depicted in Fig. 2.1(a). It shows the surface signature of a Ge impurity buried in the 5th monolayer below the Cu(100) surface. Due to interference of electrons at the surface (for more details, see next chapter) ring-like protrusions and depressions of a few picometers of electronic contrast are found. In comparison to the height of a crystal step of 181 pm the differences in height are only 1.4 %.

In the analysis of topography data, the images of Cu(100) surfaces are rotated so that the horizontal and vertical axes match the crystal [010] and [001] directions, respectively. The crystal axes are identified via constant current topographies with atomic resolution, of which one example is shown in Fig. 2.1(b). Every bright feature corresponds to a Cu atom. A crystal unit cell with the lattice constant $a_\text{Cu} = 361\,\text{pm}$ [49] is marked in red and a surface unit cell ($a_\text{surf} = 255\,\text{pm}$) is labeled in green. For every collection of data sets, the lateral lengths and heights are calibrated by comparison with the distances of atomic resolution and crystal step heights,

respectively. This is necessary because the constants of the piezoelectric elements of the STM head, which relate the applied voltage with the measured distances, show dependence on temperature and lifetime as well as position-dependent non-linearities.

2.2.2 Role of the Tip Orbital

When interpreting the tip height in the presented topography data, it is assumed that changes in the tunneling current correspond to variations in the sample's LDOS as described in Eq. 2.5. The model underlying the formula assumes an s-wave function for the tip which is, in more detail, a too simple approximation for the imaging mechanism in an STM. Although an s-wave tip images the sample's LDOS because of its radial symmetry, its spatial extent is too large to resolve atomic resolution at a metal surface [43].

Chen has investigated the consequences of different tip wave functions on the STM data [50]. In Tab. 2.1 the real tunneling matrix elements for different tip states are given. For s and d_{z^2} wave functions (with z being the direction perpendicular to the sample surface), the matrix element leads to imaging ψ^2, i.e. the sample's LDOS. For other orbitals, e.g. p_x or p_z, Chen found the so-called *derivative rule*. Then, the tunnel current is proportional to the derivative of the LDOS, e.g. for a p_x tip orbital $I \propto \frac{\partial}{\partial x} \rho_S$.

The d_{z^2} component enables enhanced image corrugation including atomic resolution due to a more spatially confined tip orbital while maintaining a tunneling matrix element that senses the sample's wave function and no derivative [51, 52]. In STM experiments, mostly PtIr or, like in our setup, W tips are used. These materials are especially well-suited to achieve atomic resolution because they mainly possess d electrons at the Fermi level and tungsten surfaces are known to host d_{z^2} states. One lobe of the d_{z^2} orbital is oriented towards the sample's surface and contributes – due to the tunnel current's exponential decay – more strongly than the orbital's surface-averted lobe or other orbitals, like d_{zx} or p, which are pointing in other directions or are not as close to the surface. In a simplified approximation, this mix of orbitals, dominated by a LDOS-imaging d_{z^2} tip wave function, can be described by an s-wave function.

In this thesis, it will be sufficient to assume the STM's tip as s-wave function as we only analyze data sets where we can ensure from symmetry arguments that we are measuring the sample's LDOS. In the literature, e.g. by Gross et al. [53], different orbitals were explicitly used in order to obtain high resolution data on pentacene

Tip state	Matrix element
s	$\gamma\psi(\mathbf{r}_0)$
p_x	$\gamma\frac{\partial\psi}{\partial x}(\mathbf{r}_0)$
p_z	$\gamma\frac{\partial\psi}{\partial z}(\mathbf{r}_0)$
d_{zx}	$\gamma\frac{\partial^2\psi}{\partial z\partial x}(\mathbf{r}_0)$
$d_{z^2-\frac{1}{3}r^2}$	$\gamma\left(\frac{\partial^2\psi}{\partial z^2}-\frac{1}{3}\kappa^2\psi\right)(\mathbf{r}_0)$

Table 2.1: Real tunneling matrix elements for different tip wave functions. The prefactor γ is a constant defined as $\gamma := 2\pi C\hbar^2/(\kappa m)$ with decay constant κ determined by the work function, electron mass m, and C as coefficient of the spherical-harmonic expansion of the tip wave function. Taken from [43].

molecules. As an s-wave-like probe they used PtIr tips that have been prepared by controlled contact with the Cu(111) surface and for p-wave tips they functionalized their tips with single CO molecules. In this manner, they could map LDOS images, derivative images, and images taken with a mix of orbitals. A tungsten wire (with possibly additional Cu atoms) was used as well in order to investigate the same molecules with an s-like tip [54].

If a state with magnetic quantum number $m \neq 0$ dominates the tip, then the atomic corrugation of metal surfaces can even appear to be inverted due to terms in the tunneling matrix elements mapping the derivative of the LDOS [55]. These changes can happen even during one scan due to spontaneous changes in the atomic structure of the tip or the chemical identity of the apex atom. We also obtained such an apparent inversion of contrast in subsequent scans at the same sample position, as presented in Fig. 2.2. The instability of the tip is reflected in the abrupt changes in the images that correspond to tip structure modifications (different heights in the scans have been removed in post-processing). One finds for Fig. 2.2(a) and Fig. 2.2(b) very good agreement, if one of both scans is inverted. It is likely, that an adatom to the tip's apex caused these different orbital imaging conditions.

For this thesis, the imaging conditions are crucially important, as for both topography and spectroscopy, we work at the resolution limits of the experimental setups. This is why for all measurements the tip is treated for obtaining stable imaging conditions mapping the LDOS of the sample which can be verified by the lateral resolution and the pattern's symmetry. As tip preparation, the tip is exposed to pulses of the bias voltage of up to $9\,\mathrm{V}$ and is carefully dipped into the crystal
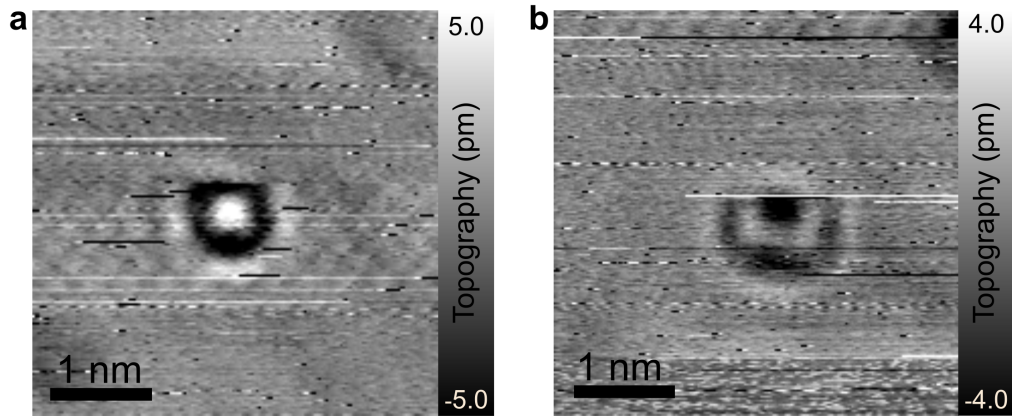
Figure 2.2: Topography inversion for surface signature of Ge impurity in 3rd layer buried in Cu(100). Both images are recorded at the same set point ($U = -100\,\text{mV}, I = 500\,\text{pA}$) and same position in immediately subsequent data sets. (a) Regular LDOS surface pattern as mapped by an s-like tip. (b) Inverted surface signature as mapped by a tip dominated by ($m \neq 0$) states with tunneling matrix elements comprising derivatives of the LDOS. The assignment of 'correct' and 'inverted' topography is based on reproducibility and stability of the measurement.

by controlled z-movements, until reproducible imaging conditions with high lateral resolution are reached.

2.3 Scanning Tunneling Spectroscopy

2.3.1 Fundamentals

Since the early years of STM, its capabilities were regularly extended to further applications by new measurement modes and techniques. Special about scanning tunneling spectroscopy (STS) is its capability to record topographic and electronic information simultaneously on the atomic scale. Other techniques are often limited to either occupied or unoccupied states or are averaging over larger sample regions. For example, it was possible to disentangle spatially the electronic information detected by angle-resolved photoemission spectroscopy on Na_2IrO_3 by means of STS to two different surface reconstructions [56].

The simplest extension of regular constant current mode measurements are *multi-bias topographies*. Within one data set, each pair of trace and retrace is recorded with different bias voltages. As all states from the Fermi energy up to the bias voltage contribute to the topography, the comparison of the line profiles contains information

about the sample's electronic structure. Because the data is recorded for different voltages line by line, disturbing factors like thermal drift are minimized.

More elaborately, *scanning tunneling spectroscopy* reveals the energy-dependence of the sample's LDOS(E) in the current-voltage characteristic, namely $\mathrm{d}I/\mathrm{d}V(V)$. This is described by the derivative of Eq. 2.5 using Leibnitz's rule [48]:

$$
\begin{aligned}
\frac{\mathrm{d}I}{\mathrm{d}V}(V,x,y,h) \propto & \rho_S(x,y,eV)\rho_T(0)T(eV,eV,h) \\
& + \int_0^{eV} \rho_S(x,y,E)\rho_T(E-eV)\frac{\mathrm{d}T(E,eV,h)}{\mathrm{d}V}\,\mathrm{d}E
\end{aligned}
\tag{2.7}
$$

Here, ρ_S denotes the LDOS of the sample while the expression is simplified by assuming a constant DOS of the tip ρ_T. For sufficiently small bias voltages V, also the transmission probability T is constant. Then the second term vanishes and the differential conductivity $\mathrm{d}I/\mathrm{d}V$ is proportional to the sample's LDOS at a specific position and energy:

$$
\frac{\mathrm{d}I}{\mathrm{d}V}(V,x,y,h) \propto \rho_S(x,y,eV)
\tag{2.8}
$$

In this thesis, STS is used to describe the surface signature of buried impurity atoms. This is why we analyze not so much the electronic structure of the crystal surface itself, but rather its change due to the subsurface scatterers. For this, we subtract the background differential conductivity $\mathrm{d}I_0/\mathrm{d}V$ of the pristine crystal surface (often averaged over a larger surface region):

$$
\frac{\Delta \mathrm{d}I}{\mathrm{d}V} = \frac{\mathrm{d}I}{\mathrm{d}V}(x,y,V) - \frac{\mathrm{d}I_0}{\mathrm{d}V}(V) \propto \Delta\rho_S(x,y,eV)
\tag{2.9}
$$

Hence, we measure the change in the LDOS with respect to the unperturbed surface.

In the experiment, for STS the tip is adjusted at one measurement point (x,y) to the set point (V_B, I_{set}) and the feedback loop is opened. Then, the bias voltage V_B is ramped through the set range, while the current I is recorded. Thus, one obtains an $I(V)$ curve for every point of the surface and the derivative $\mathrm{d}I/\mathrm{d}V(x,y,V)$ can be obtained numerically.

In Fig. 2.3 an exemplary STS data set is shown for the pristine Cu(100) surface measured with a W tip. In the $I(V)$ curve, shown in (a), a linear behavior around zero bias is found which is typical for a metal. For higher voltages the current increases more strongly, although the material's LDOS is approximately constant.
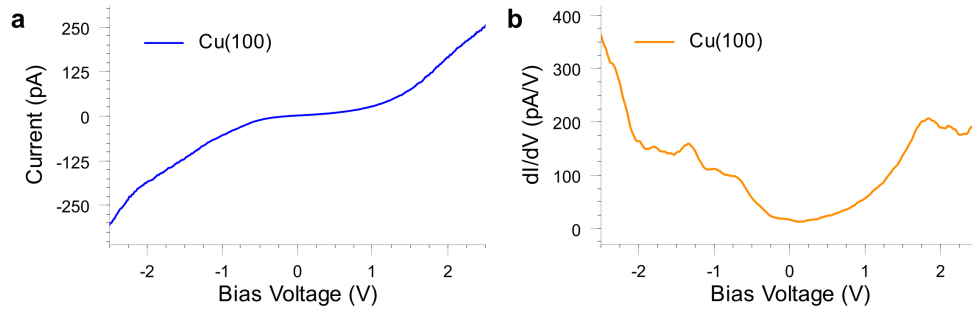
Figure 2.3: Exemplary STS data for pristine Cu(100) measured with a tungsten tip. (a) $I(V)$ curve. (b) Differential conductivity $\mathrm{d}I/\mathrm{d}V$.

This is because of an increased transmission probability T which leads to a steeper current-voltage characteristic. For a metal, for which the LDOS around the Fermi level is approximately constant and, hence, the $I(V)$ curve linear, an additional cubic factor is introduced for higher voltages. Furthermore, the strong increase in $\mathrm{d}I/\mathrm{d}V$ for $V < -2\,\mathrm{V}$ is not related to the transmission and can be explained by the onset of the Cu d band.

In order to cancel contributions of an energy-dependent transmission T, Feenstra introduced a normalization of the differential conductance $\mathrm{d}I/\mathrm{d}V$ by the conductivity (I/V) [57, 58]. However, as we investigate features close around the Fermi level, this normalization is not applied for the data of this thesis. Instead, in order to deal with various tip heights at different positions of the measurement, we run a topography normalization with the apparent barrier height, as explained below.

2.3.2 Lock-in Technique

Generally, for the analysis of STS data, one could take the values of a recorded $I(V)$ curve and calculate the numerical derivative. However, the tunnel current contains noise that follows a $1/f$-law, with f being the frequency within the current signal. In order to obtain a useful signal-to-noise ratio, one would have to average over long times for every data point. As the measurement of an STS map can easily take hours, this is not a suitable way. Instead, we use a *lock-in amplifier* for acquiring STS data.

With the lock-in technique, an AC modulation voltage $V_{\mathrm{mod}} = V_{\mathrm{mod}}^0 \sin(\omega_{\mathrm{mod}} t)$ is added to the bias voltage at every step while ramping through the $I(V)$ curve. This voltage V_{mod} causes a modulation with identical frequency ω_{mod} in the tunneling current I. By multiplying the resulting tunneling current with the modulation voltage
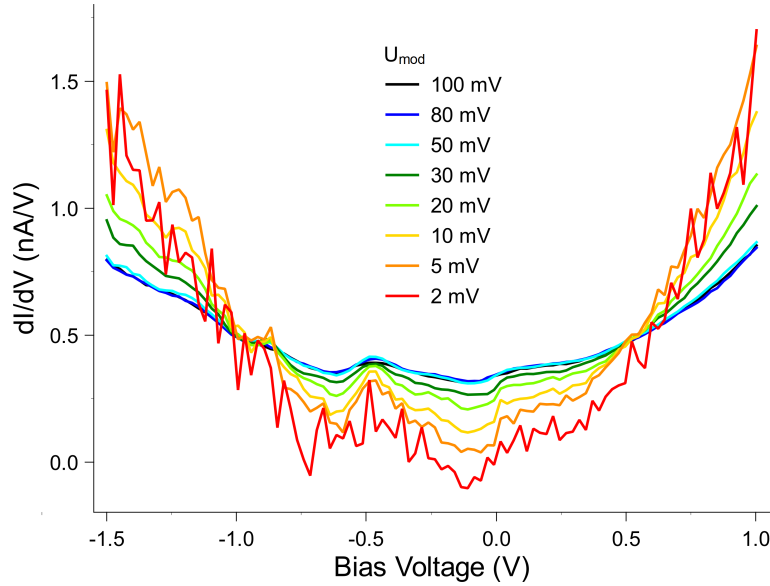
Figure 2.4: Comparison of modulation voltages in lock-in assisted STS on Cu(100). Single $\mathrm{d}I/\mathrm{d}V$ spectra at the same position with varying modulation voltages ($V_{\mathrm{mod}} = 2...100\,\mathrm{mV}$). Other parameters like $\omega_{\mathrm{mod}} = 2\,\mathrm{kHz}$, bias voltage step size ($V_{\mathrm{step}} = 25\,\mathrm{mV}$), number of oscillations per bias step ($N = 10$) and set point ($V = -1.5\,\mathrm{V}, I = 0.7\,\mathrm{nA}$) are kept constant. Each curve is an average over 100 spectra. Higher modulation voltages lead to less noise at the expense of resolution for small energetic features.

as reference signal, the lock-in amplifier gives direct access to the first derivative of the $I(V)$ curve:

$$\frac{\mathrm{d}I}{\mathrm{d}V}(V) = \frac{2}{V_{\mathrm{mod}}^0 \tau} \int_0^\tau \sin(\omega_{\mathrm{mod}} t + \varphi) I(t)\,\mathrm{d}t \qquad (2.10)$$

Here, τ is the integration time of the measurement and the sinusoidal oscillation is the reference signal including the phase shift φ. This equation is an approximation that holds if for every probed bias voltage the differential conductivity is approximately linear in an interval $[V - V_{\mathrm{mod}}^0, V + V_{\mathrm{mod}}^0]$, which is true for the metallic system of Cu. A more thorough mathematical description of the lock-in technique and its implementation in our setup can be found in other works [59, 60].

In our experiment, we use $\omega_{\mathrm{mod}} = 2\,\mathrm{kHz}$ as modulation frequency. For such frequencies, the noise in the tunneling current is substantially reduced. We further improve signal-to-noise ratio by using a bandpass-filtered signal ('ISO-Out') as input for the lock-in amplifier. The choice of modulation voltage amplitude V_{mod} influences the data obtained as $\mathrm{d}I/\mathrm{d}V$. While a larger modulation voltage leads to a stronger

signal, for small modulation voltages also features on small energy scales can be mapped. This is visualized in Fig. 2.4 where the results of the same measurement are shown for different modulation voltages. Energetically confined structures like the step at zero bias are smeared out for high modulation voltages.

In a lock-in assisted measurement, the effects of the capacitance of the setup, electronic wiring, and the tip-sample system have to be taken into account. This 'capacitive cross talk' from ω_{mod} leads to an additional signal in the lock-in $\mathrm{d}I/\mathrm{d}V$ output – almost independent of energy, but in the same order of magnitude or higher than the sample's signal – which is also present if the distance between tip and sample is too large for a tunneling current. This can be exploited to obtain undisturbed data: before the measurement, the tip is retracted 10 nm and a lock-in spectrum is acquired. Then, the phase shift is adjusted, so that the capacitive signal vanishes in the lock-in signal (or, for a two-phase lock-in amplifier, in one of the reference channels sine/cosine). Consequently, for data acquired in tunnel contact, this channel only contains data from the tunneling current.

In our setup, the voltage modulation is generated by a digital signal processor (DSP), which also operates as lock-in amplifier. In order to reduce noise collected during the transmission to the sample, the measurement electronics divide the modulation voltage by 1:10 just before the output to the sample. A full data set with typical parameters (200×200 pixel, 10 lock-in oscillations per bias step) requires several hours to be recorded. As the lock-in technique does not offer an absolute scale of the data, a scaling factor is calculated from the numerical derivative of the $I(V)$ curve to adjust the data scale.

2.3.3 Apparent Barrier Height

In the preceding section, Hamers' approximation for the tunneling current (Eq. 2.5) and the tunneling probability (Eq. 2.6) were discussed in the context of constant current topographies. In another measurement mode, the STM can be used to obtain the *apparent barrier height* Φ which is a quantity that describes the energy barrier that an electron experiences due to the junction and is related to the work functions ϕ of both tip and sample [43]. The tunneling probability can be written, consistent with Eq. 2.6, with the decay constant $\kappa = \frac{\sqrt{2m\Phi}}{\hbar}$ as
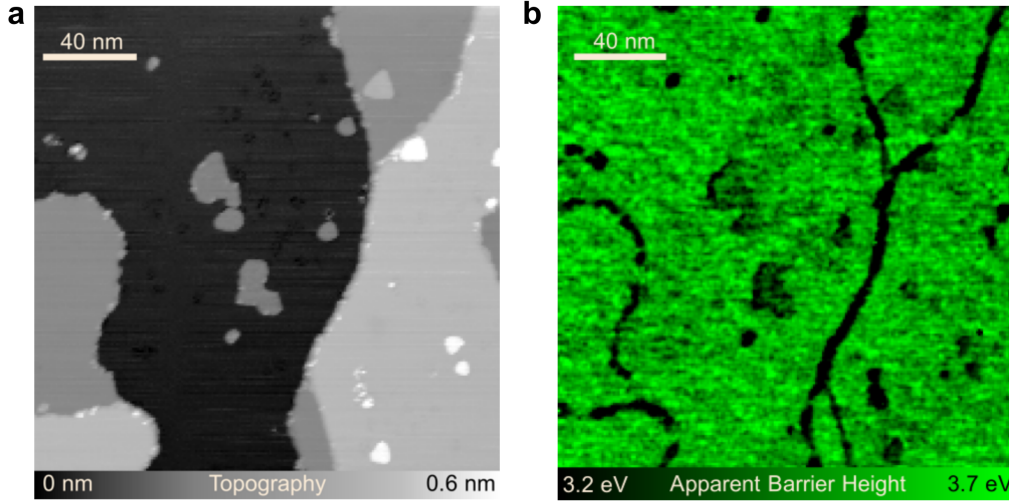
$$T = \exp(-2\kappa h). \tag{2.11}$$

Figure 2.5: Ge-Cu-alloy islands on Cu(111). (a) Topography ($V = 1\,\text{V}, I = 0.1\,\text{nA}$) with various crystal steps and approximately triangular shaped islands. (b) Apparent barrier height map clearly showing two distinct values for pristine surface and islands.

Solving these equations for the apparent barrier height Φ, one finds

$$\Phi = \frac{\hbar^2}{8m}\left(\frac{\mathrm{d}\ln I}{\mathrm{d}h}\right)^2 \approx \frac{\hbar^2}{8m}\left(\frac{\ln(\Delta I)}{\Delta h}\right)^2 \tag{2.12}$$

which suggests the experimental access to Φ: the tip is moved by a predefined distance Δh closer to the surface, usually around $0.5\,\text{Å}$, and the difference in tunneling current ΔI is recorded. With Eq. 2.12 the apparent barrier height is calculated.

An example for a barrier height measurement is presented in Fig. 2.5 with a topography of Cu(111) with Ge-Cu-alloy islands on its surface and a corresponding apparent barrier height measurement. For the Cu surface, an average barrier height of $\Phi_{\text{Cu}} = 3.6\,\text{eV}$ is measured, while for the islands a value of $\Phi_{\text{Island}} = 3.3\,\text{eV}$ is obtained. In this data set, this measurement mode allows to distinguish between the Cu surface and the Ge-Cu-alloy islands. At the steps, the values diverge to smaller values, which can be explained by two effects. First, the geometry at step edges leads to a stronger increase of tunneling current when moving the tip towards the surface (tunneling does not only occur perpendicularly to the surface). Second, the Smulochwski effect describes the creation of dipoles at steps that originate from the electronic charge redistribution near atomically sharp surface corrugations in order to smoothen the abrupt variation of crystal potential [61].

Besides local variation, as the apparent barrier height is a quantity that describes

the tunneling process, it can also change depending on the bias voltage. However, for metals in an energy interval as small as considered in this thesis, it can be assumed to be constant. The apparent barrier height comes in handy for the analysis of STS data as it allows for the topography normalization that is described in the following subsection.

2.3.4 Topography Normalization

As explained above, the data of an STM measurement is a superposition of surface morphology and electronic information. While for topography measurements one has to consider electronic contributions to the height information, the same is necessary for spectroscopy measurements where height contributions have to be considered in the electronic dI/dV signal.

Before every STS measurement, the tip height is adjusted according to the (constant current) set point $(V_{\mathrm{Set}}, I_{\mathrm{Set}})$, which corresponds to the integral of dI/dV between $V = 0\,\mathrm{V}$ and V_{Set}. This causes difficulties for the interpretation of the $dI/dV(x, y)$ data which correspond to the sample's LDOS. In surface regions with a high LDOS, the tip is retracted in order to maintain the same set point current. Then, although the electronic structure is different, the spectrum might be similar to a position with lower LDOS. This problem occurs especially for bias voltages with the same sign as the set point voltage. For voltages on the other side of the Fermi energy, the constraint of the set point is not given and therefore the dI/dV shows more structure. However, also there the measurement is affected by the tip-sample distance.

A simple, first approach are two measurements of the same surface area with set points on both sides of the Fermi level. However, this does not compensate for all effects of the mix of morphologic and electronic structure.

A solution is a *topography normalization*, which is a projection of the dI/dV data to a constant height contour. Every spectrum is multiplied by a scalar factor in order to appear as if it was recorded in constant height mode. This technique was proposed by Garleff et al. [62].

The topography normalization is based on the exponential dependence of the tunneling current on the tip-sample distance, as described in Eq. 2.5. The normalized spectrum is given, in the spirit of Hamers' model, by

$$\frac{dI}{dV}(V, x, y)\big|_{h=h^*} = \frac{dI}{dV}(V, x, y) \cdot \exp(2\kappa[h(x, y) - h^*]) \qquad (2.13)$$

Here, κ is the decay constant, which was introduced in Sec. 2.3.3 and includes the apparent barrier height Φ. Thus, for the topography normalization an STS measurement should be accompanied by an apparent barrier height measurement in order to obtain local data. Alternatively, an average value for Φ can be used.

The described topography normalization is performed for all data sets shown in this thesis if not noted otherwise. The usage of this tool is only reasonable for structurally flat surfaces with only electronic contrast in the constant current topography. In other words, when crystal steps are mapped, a normalization to a constant height is possible, but not meaningful.

2.4 Experimental Setup

In this thesis, two home-built ultra-high vacuum (UHV) low-temperature (LT) scanning tunneling microscopes have been used for data acquisition. Both chambers are equipped with an ion getter pump as well as a titanium sublimation pump in order to keep a base pressure of $p \approx 5 \times 10^{-11}$ mbar. They accommodate Besocke type STM heads [63], where three piezo elements, each equipped with four high-voltage contacts, are used for lateral movement in the (x, y)-plane and an additional piezo element serves for the z-movement of the tip. Both setups contain tanks for liquid helium (LHe) and liquid nitrogen (LN$_2$) allowing measurements at room temperature, $T = 80$ K and $T = 6$ K. All data presented in this thesis were obtained at LHe-temperature (6 K). The systems keep the temperature for times of 18 h and 28 h, respectively, with one filling when operated with LHe. As an STM offers atomic resolution (the setups used here have lateral step sizes of ~ 3 pm and ~ 0.12 pm in height), the systems have to be decoupled from any perturbations from the environment, like mechanical vibrations. With several damping stages, one setup even has its own foundation to be separated from the building.

The tips acting as the probes play a very important role in the STM measurement process. We use electrochemically etched tungsten tips. In a UHV preparation step, the tips are annealed and sputtered in order to obtain long-term stability as required for STS measurements, before the tip's quality is checked by field emission. Further details of the tip preparation process is found in [64, 65].

The electronics of the setup are controlled by a computer with the measurement software `GoeSTM` and two digital signal processors (DSP). The bias voltage as well as x and y control voltages are operated by 16-bit digital-to-analog converters (DAC),

while the z movement is controlled by an 18-bit DAC. The spatial resolution is further advanced by the use of high-voltage attenuators at the UHV feedthrough which limit the total measurement range, but reduce the step size between neighboring data points. A further description of the electronic setup is found in previous work [37–39].

3 Electron Propagation and Scattering in Cu

The sample systems investigated in this thesis are noble metals with single atoms of another species buried below the surface. These impurities introduce a perturbation into the system that is screened by the charge carriers, i.e. the electrons, which are present with a high density in a metal. In this chapter, we describe the electronic structure and its response to the perturbation of the impurity. Of special interest is the *electron focusing* effect which explains long-range propagation in certain spatial directions by anisotropies in the host's band structure and allows to investigate buried impurities via their scattering patterns at the surface. We use a plane wave tight-binding model to calculate the electronic structure of Cu and simulate the experimental surface interference patterns. As a complementary approach, M. Bouhassoune and S. Lounis at FZ Jülich have performed ab-initio calculations using density functional theory (DFT) with the Korringa-Kohn-Rostoker (KKR) method. Another characteristic in the electronic structure of a solid, not limited to dilute alloys, is electron-phonon coupling. Described as many-body effect with a self-energy, it leads to a renormalization of the solid's dispersion.

In this chapter, first, we briefly describe textbook mechanisms of screening in metals. Subsequently, we review STM experiments from the literature that investigate scattering patterns in two-dimensional systems, in particular metal surface states. Thirdly, we introduce the concepts of electron focusing in a three-dimensional bulk and discuss the hitherto existing experiments that exploit this effect. Then, we introduce the Green's function method as the theoretical background of the numerical calculations before we present the tight-binding model and its application to identify the contributions from different orbital characters to the Fermi surface and the interference patterns. Subsequently, the results of the KKR-DFT calculations are briefly introduced. Finally, we introduce electron-phonon coupling in its many-body description and review related previous findings from the literature.

3.1 Screening in Metals

The charge carriers in a solid respond to perturbations by screening the external potential. These mechanisms are covered in detail in solid state physics textbooks, e.g. [66, 67], and are only briefly discussed here. In general, the dielectric function $\epsilon(\mathbf{q}, \omega)$ describes how the total potential is modified due to the screening of an external (perturbative) potential with wave vector $\mathbf{q}$ and frequency ω:

$$\Phi_0^{\text{total}} = \frac{\Phi_0^{\text{ext}}}{\epsilon(\mathbf{q}, \omega)} \tag{3.1}$$

The Lindhard theory [68] describes the screening process by quantum-mechanical first-order perturbation theory and the random phase approximation. Then, the dielectric function for a static perturbation ($\omega = 0$) is given by

$$\epsilon(\mathbf{q}, \omega = 0) = 1 + \frac{e^2}{q^2 \epsilon_0} \sum_{\mathbf{k}} \frac{f_0(\mathbf{k}) - f_0(\mathbf{k} + \mathbf{q})}{E(\mathbf{k} + \mathbf{q})} \tag{3.2}$$

with f_0 being the Fermi-Dirac distribution function in thermal equilibrium and the electron dispersion $E(\mathbf{k})$.

A special case in Lindhard screening theory is Thomas-Fermi screening that describes a static perturbation in the long wavelength limit, i.e. the perturbing potential changes slowly on the length scale of the Fermi wave length ($q \ll k_F$). The dielectric function is then given with few approximations including a linearization of the electron density at the Fermi level by

$$\epsilon(\mathbf{q}, 0) = 1 + \frac{D(E_F)e^2}{\epsilon_0 V} \frac{1}{q^2} = 1 + \frac{k_s^2}{q^2}. \tag{3.3}$$

Here, k_s denotes the Thomas-Fermi wave vector with the density of states $D(E_F)$

$$k_s = \sqrt{\frac{e^2}{\epsilon_0} \frac{D(E_F)}{V}}. \tag{3.4}$$

The resulting so-called Yukawa potential is given by

$$\Phi^{\text{total}}(\mathbf{r}) = \frac{Q}{\epsilon_0 r} e^{-k_s r} \tag{3.5}$$

which consists of a Coulomb potential and an exponential decay as a function of

the distance from the point charge Q. For Cu with a conduction band electron density of $n = 8.47 \times 10^{22}\,\mathrm{cm}^{-3}$, the corresponding Thomas-Fermi screening length is $\lambda_{\mathrm{TF}} = 0.55\,\text{Å}$ [67]. This means that in this approximation already at the nearest neighbor in the Cu fcc crystal lattice ($d = 255\,\mathrm{pm}$) the perturbation is almost completely screened due to the high charge carrier density.

For the static case at $T = 0$, also the more general Lindhard calculation can be performed explicitly, yielding

$$\epsilon(\mathbf{q}, 0) = 1 + \frac{e^2 D(E_F)}{q^2 \epsilon_0 V}\left[\frac{1}{2} + \frac{1 - x^2}{4x}\ln\left|\frac{1 + x}{1 - x}\right|\right] \quad \text{with} \quad x = \frac{q}{2k_F} \tag{3.6}$$

The last term in brackets can be interpreted as the Lindhard correction to the Thomas-Fermi formula, which becomes relevant for $x \neq 0$. In this solution, the dielectric function is not analytical for $q = 2k_F$. It can be shown that this leads for the screened Coulomb potential of a point charge to an oscillating potential

$$\Phi^{\mathrm{total}}(\mathbf{r}) = \frac{1}{r^3}\cos(2k_F r). \tag{3.7}$$

These oscillations are called *Friedel oscillations*. For the charge, which rearranges in order to cause the screening effect, a corresponding periodicity is found with Δn being the charge difference with respect to the undisturbed surface:

$$\Delta n(\mathbf{r}) \propto \frac{\cos(2k_F r + \varphi)}{r^3} \tag{3.8}$$

Here, φ is a scattering phase shift which is a property of the impurity. The periodicity in k_F is only given by the host. While in the Thomas-Fermi approximation an exponential term describes the screening, the Friedel oscillations show a long-range effect on the potential landscape.

3.2 2D: Surface State Scattering

The surface state on the (111) surface of noble metals like Ag, Au, or Cu is a prototypical system of a 2D electron gas. When electrons are scattered at substrate steps or single adatoms, standing wave patterns form in the local density of states. These are Friedel oscillations as response of the electronic system to the perturbation of the defect. Already in the early days of STM, this phenomenon was imaged with the famous 'quantum corrals', illustrating impressively the wave-like nature of
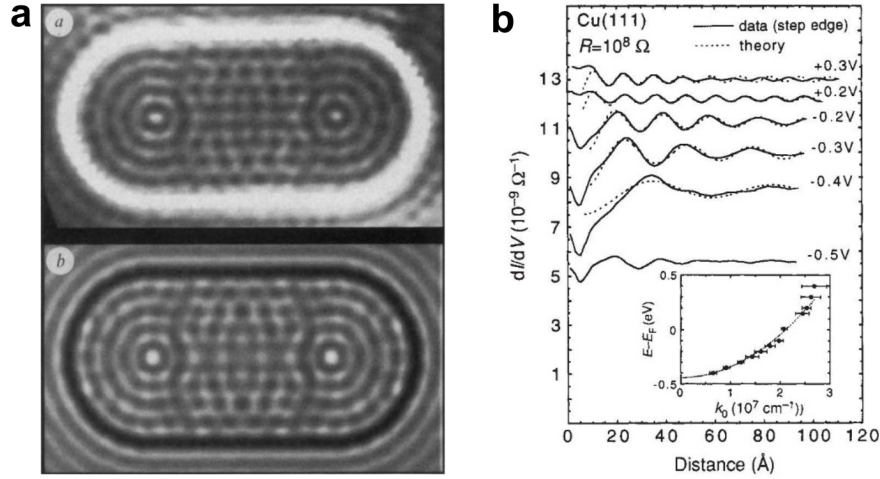
Figure 3.1: Studying standing wave patterns on Cu(111). (a) Experiment ($U_B = 10\,\mathrm{mV}$) and theory of LDOS near E_F for a 76 Fe atom 'stadium' with size $141 \times 285\,\text{Å}^2$. Reprinted by permission from Springer Nature: Nature, Heller et al. [70], copyright (1994). (b) Spatial dependence of $\mathrm{d}I/\mathrm{d}V$ as a function of distance from step edge at different bias voltages. Inset: surface state dispersion. Reprinted by permission from Springer Nature: Nature, Crommie et al. [3], copyright (1993).

electrons [69–72] (Fig. 3.1a). These investigations opened up a wide field of research, which has been discussed elsewhere, e.g. [73–76], and is here only reviewed more specifically.

In contrast to momentum space-based techniques like ARPES, resolving Friedel oscillations with an STM allows for investigations in real space, which makes it possible to directly link electronic characteristics with local structural properties. The atomic resolution provides the ability to identify and examine individual features without averaging over multiple defects or surface structures.

Analyzing the energy-dependent wave lengths in the scattering pattern reveals the dispersion relation $E(\lambda)$ and, thus, $E(k)$ [3, 4, 77, 78]. The almost-parabolic dispersion of the surface state is shown in Fig. 3.1(b). For the oscillations at a step edge, the amplitude decays with distance from the scatterer even without inelastic scattering due to the properties of the 2D electron gas. From an additional decay of the pattern's amplitude with respect to the model, phase relaxation lengths can be extracted. They were estimated at the Fermi energy for different temperatures [79] and with energy-dependence for low temperature [11]. While the energy-dependent lifetime is interpreted as electron-electron scattering, i.e. interaction of the surface state with the underlying bulk electrons, the temperature-dependence is considered to
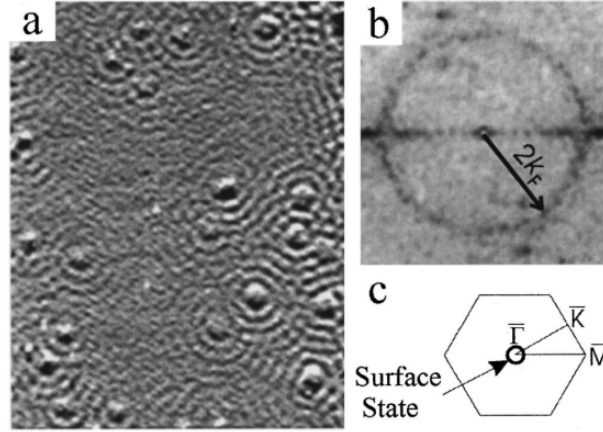
Figure 3.2: (a) Constant-current topography ($425 \times 550\,\text{Å}^2$) of Cu(111) obtained at $U_B = -5\,\text{mV}, T = 150\,\text{K}$, showing a complex pattern of circular waves extending out from point defects. (b) 2D Fourier transform of the image in (a). (c) Sketch of the surface Brillouin zone of Cu(111) with the Fermi contour. Reprinted figure with permission from Petersen et al. [83]. Copyright (1998) by the American Physical Society.

quantify the interaction with phonons [80]. The scattering patterns also revealed the electron potential landscape on Au(111), including modulations due to a 'herringbone' reconstruction [81].

While in the scattering pattern of a single defect, e.g. a step, mostly one dominant wave vector is analyzed, Fourier-transformed constant-current STM images or STS data show the full Fermi contour of the surface. This was first performed for the Friedel oscillations on the Be(0001) [82] and Cu(111) surfaces [83], revealing the Friedel oscillations' $2k_F$ wave vector, as depicted in Fig. 3.2. This technique is termed Fourier-transform STM (FT-STM) or quasiparticle interference (QPI) and gave insight into more complex 2D band structures of the high-T_c superconductor $\text{Bi}_2\text{Sr}_2\text{CaCu}_2\text{O}_{8+\delta}$ [6, 84] and the semi-metal ErSi_2 [85, 86]. It was also found to enable the investigation of the spin character of the quasiparticles with a non-magnetic STM [87]. QPI has evolved to a standard STM technique to investigate 2D systems concerning band structure, doping level or scattering properties, e.g. topological insulators [88, 89], transition metal dichalcogenide monolayers (TMDCs) [90] or graphene [91, 92]. Its importance to detect and quantify band structure renormalizations due to quasiparticles is later discussed in Sec. 3.8.2.

For the Be($10\bar{1}0$) surface, the scattering at surface defects by Friedel oscillations was found to be anisotropic, which was linked to the two-dimensional band structure [93]. This means that the scattered surface state will not propagate in every direction,

if the band structure is not isotropic. This finding in 2D will become crucially important for the 3D experiments of this thesis. The electron focusing mechanism, as described in Sec. 3.3, relies on an anisotropic electronic structure.

The standing wave patterns of the surface states can transmit long-range interactions between adsorbates [94–96]. This is exploited by the molecular nanoprobe (MONA) technique, where hot electrons induced by the tip are used to switch remotely the tautomerization of single molecules deposited at a different position of the surface [97, 98].

Finally, the standing wave patterns of surface states can be utilized to characterize the scattering properties of surface defects, e.g. measuring the phase shifts and therefore the reflectivity of different facets of substrate steps of Au [4]. As another example, the Kondo signature of a single surface magnetic impurity on Cu was analyzed in rigorous detail [18, 19, 99–105], revealing the Kondo phase shift and the Kondo resonance. This is possible because the scattering patterns always consist of components given by the scattering event as well as the propagation. In this fashion, also in the 3D experiments of this thesis we can obtain insights into the scatterer and the scattered electrons.

3.3 3D: Electron Focusing

Although the STM is a surface-sensitive technique, it can reveal information about the bulk. For this, the electrons measured at the surface by the STM as LDOS act as messenger and contain the information from the bulk.

The 2D surface state discussed in the previous section is mostly located at the surface, but also reaches with its wave function into the bulk where it can interact with impurities, which was already suggested by Crampin in 1994 [106]. In addition to the Fermi surface of the surface state, Fourier-STM also revealed selected bulk contributions, showing two different k_F in the spectra. Because of their high $k_{||}$ component, the parts close to the 'neck' of the Cu and Au Fermi surface were found for Cu(111) and Au(111) [107, 108]. Also for Ag(110) certain bulk contributions could be identified [109]. Recently, QPI was used to characterize the bulk electronic structure of galena (PbS), which was enabled by its disconnected Fermi surface without in-plane states at $k_z = 0$ [110].

First investigations with states in three dimensions were performed with quantum well states and resonances in thin metal films [111, 112]. Depending on the depths

of the film, the confined states show constructive and destructive interference fringes at the surface [113] and could be used to map a buried Si-(7 × 7) interfacial atomic lattice [114], to measure subsurface reflection phases [115], or to characterize the influence of the interface quality for confined states [116].

The surface signature of confined subsurface objects was first found by Schmid et al. for noble gas cavities in Al(111) [117]. Such Ar bubbles can be introduced by sputtering and annealing when preparing the surface for the STM experiment. Later, similar features were found for Cu(111) and Cu(100), which were linked to an anisotropic electron propagation due to the electronic structure, as it was found before in transport experiments like ballistic electron emission microscopy [118–121]. The investigation of subsurface nanocavities in Cu was thoroughly continued by Kurnosikov and co-workers, characterizing their growth [122, 123] as well as the influence on the surface pattern by the specific shape of the cavity and the anisotropy of the band structure [124–126]. More recently, subsurface Co nanoclusters in Cu(001) and near-surface diffusion were investigated [127, 128].

Weismann and colleagues showed that the investigation of a single subsurface impurity is possible [20]. For this, it was made use of the Friedel oscillations around a Co atom buried in Cu, which show a strong directionality due to the host's anisotropic band structure. This nanoscale electron focusing effect is discussed in detail below as it is the pivotal mechanism for the measurements in this thesis. The investigation of point-like defects of single residual sputter Ag and Ne gas atoms buried in Ag showed how crucially such measurements depend on the properties of the STM tip [129].

The theoretical background of electron focusing was studied [130–132] and different systems were investigated experimentally. Especially the Kondo effect was characterized at single magnetic atoms, e.g. Fe or Co buried in Cu [22–24]. The STM enables to investigate the itinerant electrons around such a Kondo system and the interaction of multiple impurities with atomic precision. Electron focusing could also be applied to study the two-band superconducting gap of Pb [21] and spin-filtered Friedel oscillations in thin films [133]. Within this thesis, we will discuss the signature of non-magnetic impurities.

The electron focusing effect describes the directional propagation of electrons within a solid due to an anisotropic band structure. An electron has a wave vector **k**, but propagates within the solid according to its group velocity that is given by the
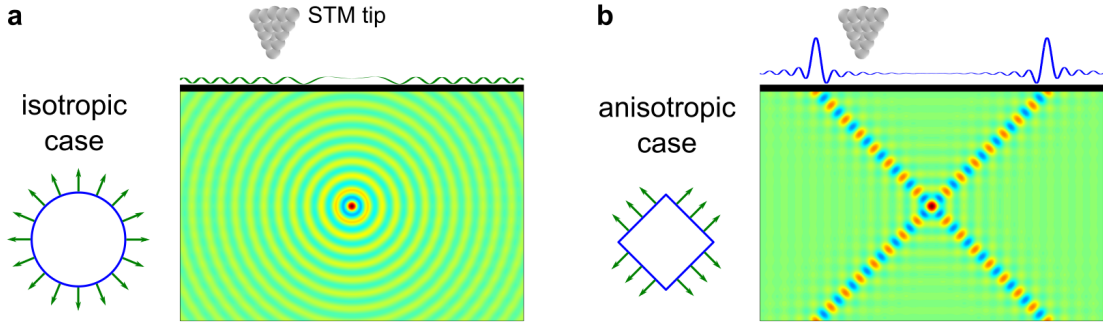
Figure 3.3: Illustration of the electron focusing effect. (a) For an isotropic isoenergy contour (blue) the group velocity vectors (green) point in all spatial directions. The electron propagation is equally isotropic and causes no significant signal at the surface. (b) For an anisotropic isoenergy contour, the electrons propagate in distinct directions without decay. The corresponding electronic contrast can be recorded at the surface by an STM. Figure inspired by [59, 134].

gradient of the band structure:

$$\mathbf{v}_{\mathrm{gr}}(\mathbf{k}) = \frac{1}{\hbar}\nabla_{\mathbf{k}}E(\mathbf{k}) \qquad (3.9)$$

The consequences for electron propagation are illustrated in Fig. 3.3. First, we consider an isotropic isoenergy contour, e.g. the Fermi surface, depicted in Fig. 3.3(a). Then, according to Eq. 3.9, the group velocity vectors point equally distributed in all directions and the electron propagation in real space is isotropic. It is a superposition of all electrons of the given energy and can be described by a spherical wave that decays with r^{-1} in 3D, where r is the distance from the starting point. It follows that hardly any signal is obtained at the surface. For such a system, a perturbation like an impurity is screened as in the textbook description from Sec. 3.1, i.e., 3D Friedel oscillations $\propto r^{-3}$ are formed.

For an anisotropic isoenergy contour (Fig. 3.3b), flat regions show an accumulation of group velocity vectors and cause an enhanced electron flux in certain directions. The electron propagation follows distinct beam-like paths with almost no decay, so that a signal is found at the surface. Although the depicted anisotropic is an extreme example, even a simple noble metal like Cu shows electron focusing behavior. We use this to image at the surface the signal from subsurface impurities. For the surface pattern of such a scattering center, the incoming and outgoing electron waves interfere at the surface constructively or destructively, depending on their phase difference, causing a protrusion or depression.

3.4 Green's Function Method

The propagation of electrons in a solid can be expressed in many-body theory by the single-particle Green's function G. It acts as quantum-mechanical propagator and specifies the probability of a particle to travel from one position $\mathbf{x}'$ to another position $\mathbf{x}$ in a given time $t - t'$ or to travel with certain momentum $\mathbf{k}$ and energy ε. The applications of Green's functions are widely spread and are therefore discussed in depth in the literature, e.g. Mahan's classic [135], Mattuck's pedagogical introduction [136], or more recent textbooks [137–140]. Here, we will focus on the most important relations that are relevant for the simulations.

3.4.1 Single-Electron Propagator G_0

The time-dependent Schrödinger equation determines the time evolution of an electron's wave function $\psi(t)$ for a Hamiltonian H:

$$i\hbar\frac{\partial}{\partial t}\psi(t) = H\psi(t) \tag{3.10}$$

Two propagators, the retarded Green's function $G^R(t)$ and the advanced Green's function $G^A(t)$, can be defined with the boundary conditions $G^R(t) = 0$ for $t < 0$ and $G^A(t) = 0$ for $t > 0$:

$$\left(i\hbar\frac{\partial}{\partial t} - H\right)G^{R,A}(t) = \delta(t) \tag{3.11}$$

More generally, the Green's function could be defined for any operators $\hat{A}$ and $\hat{B}$. The single-particle propagator used here is the Green's function for the electron creation and annihilation operators $\hat{c}$ and $\hat{c}^\dagger$. The propagators act on the wave function, similarly to the time evolution operator e^{-iHt}, by moving it forward (retarded) and backward (advanced) in time:

$$\psi(t) = iG^R(t - t')\psi(t') \quad \text{for} \quad t' < t \tag{3.12}$$

$$\psi(t) = iG^A(t - t')\psi(t') \quad \text{for} \quad t' > t \tag{3.13}$$

Here, we are only interested in the retarded Green's function and will drop the index R. The index 0 will denote the unperturbed propagator without interactions. From the Fourier transform of the time-dependent Green's function $G_0(t) = -i\Theta(t)\exp(-iHt)$,

we obtain a formal solution for an energy-dependent propagator $G_0(\mathbf{k}, \varepsilon)$ with wave vector $\mathbf{k}$

$$G_0(\mathbf{k}, \varepsilon) = \frac{1}{\varepsilon - E(\mathbf{k}) + i\eta} \tag{3.14}$$

Here, the Hamiltonian H is replaced with the dispersion relation $E(\mathbf{k})$ and an infinitesimally small η is introduced to ensure convergence of the integral. This term can be expanded for the energies

$$G_0(\mathbf{k}, \varepsilon) = \int_{-\infty}^{\infty} \frac{A(\mathbf{k}, \hbar\omega')}{\varepsilon - \hbar\omega' + i\eta} \, d\omega' \tag{3.15}$$

with the spectral density function $A(\mathbf{k}, \hbar\omega)$. This quantity determines which frequencies and thus energies are most represented for this wave vector. For electrons, $A(\mathbf{k}, \hbar\omega)$ is always positive and acts as probability density following the relation

$$1 = \int_{-\infty}^{\infty} \frac{d\omega}{2\pi} A(\mathbf{k}, \hbar\omega) \tag{3.16}$$

Even more importantly, by applying the Dirac identity, which reads in simplified terms

$$\lim_{\eta \to 0} \frac{1}{x \pm i\eta} = \mathcal{P}\left(\frac{1}{x}\right) \mp i\pi\delta(x) \tag{3.17}$$

with $\mathcal{P}$ as Cauchy principal value of an integral and δ as Dirac distribution, the spectral function can be related with the imaginary part of the propagator by

$$A(\mathbf{k}, \hbar\omega) = -\frac{1}{\pi} \operatorname{Im} G(\mathbf{k}, \hbar\omega) \tag{3.18}$$

When we consider the Green's function in real space, i.e. the propagator that gives the probability for an electron to move from an position $\mathbf{x}'$ to $\mathbf{x}$, we obtain in spectral representation with the eigenfunctions $\Psi_{\mathbf{k}}(\mathbf{x})$

$$G_0(\mathbf{x}, \mathbf{x}', \varepsilon) = \lim_{\eta \to 0} \int_{\mathbf{k} \in \text{FBZ}} \frac{\Psi_{\mathbf{k}}(\mathbf{x})\Psi_{\mathbf{k}}^*(\mathbf{x}')}{\varepsilon - E(\mathbf{k}) + i\eta} \, d\mathbf{k} \tag{3.19}$$

Also this integral over the first Brillouin zone (FBZ) can be approached by the Dirac identity, similarly to the spectral function in momentum space. Here, the wave functions act as spectral weight in the summation over $\mathbf{k}$. This yields a link between

the imaginary part of the propagator at one position $\mathbf{x}$ and the LDOS, which is nothing else than an energy-selected sum over the wave function (Eq. 2.4):

$$\rho(\mathbf{x}, \varepsilon) = \sum_{\mathbf{k}} |\Psi_{\mathbf{k}}(\mathbf{x})|^2 \delta(\varepsilon - E(\mathbf{k})) = -\frac{1}{\pi} \operatorname{Im} G_0(\mathbf{x}, \mathbf{x}, \varepsilon) \tag{3.20}$$

The specific form of the Green's function depends on how the electronic band structure is calculated and thus the chosen model. Two approaches, the tight-binding model and the KKR ab-initio calculations, will be discussed in the course of this chapter.

3.4.2 Impurity Scattering

So far, we have characterized the free electron propagation within the host with the propagator G_0. In order to describe our experiment, we have to implement the scattering at the impurity site, too. This is included in the propagator G (without index) which is called 'dressed', because apart from free propagation it also contains these interactions.

Scattering occurs because the crystal potential is perturbed at the impurity by a potential difference $\Delta V = V_{\text{imp}} - V_{\text{Cu}}$ compared to the host solid. The propagators for the perturbed system G with Hamiltonian $H = H_0 + \Delta V$ and the unperturbed system $G_0 = (\varepsilon - H_0 + i\eta)^{-1}$ are connected by the Dyson equation

$$G = [1 - G_0 \Delta V]^{-1} G_0 \tag{3.21}$$
$$= G_0 + G_0 \Delta V G \tag{3.22}$$

If we insert G again on the right-hand side, we can visualize its meaning by expanding the equation into a Born series of multiple scattering events with ΔV:

$$G = G_0 + G_0 \Delta V G_0 + G_0 \Delta V G_0 \Delta V G_0 + \dots \tag{3.23}$$

We can simplify the calculation by introducing a scattering matrix T (also called *transition matrix* and thus the notation) that connects the states of the perturbed and unperturbed systems by $\Delta V |\psi\rangle = T|\psi_0\rangle$. The Dyson equation then reads

$$G = G_0 + G_0 \Delta V G \tag{3.24}$$
$$= G_0 + G_0 T G_0 \tag{3.25}$$

and the scattering matrix T can be expressed as a series of ΔV

$$T(\Delta V) = \Delta V + \Delta V G_0 T(\Delta V) \tag{3.26}$$

$$= \Delta V + \Delta V G_0 \Delta V + \Delta V G_0 \Delta V G_0 \Delta V + ... \tag{3.27}$$

This shows that for small perturbations, a first order Born approximation holds and $T \approx \Delta V$.

Depending on the calculation, the scattering matrix is expressed differently. In the following, we present a simpler tight-binding model and show the results of more elaborated ab-initio calculations in the KKR formalism. In the respective sections, we discuss the details of these implementations.

3.5 Tight-Binding Model

Our main approach to implement the Green's function method is a plane wave tight-binding model. First, the band structure of Cu is calculated and is then used to determine the single-particle propagator $G(\mathbf{x}, \mathbf{x}', \varepsilon)$. The model was developed and described in detail by A. Weismann [134]. In the following subsections, we give an overview of the most important aspects and refer for the technical details to the literature. In this thesis, the model was extended for orbital-resolved calculations and employed to extract an effective scattering phase shift of the impurities. Despite a few simplifications that will be outlined, the simulations prove to predict the experimental data accurately while being easily executed on a common desktop computer using MATLAB.

3.5.1 Band Structure of Cu

The band structure $E(\mathbf{k})$ of Cu is calculated in a tight-binding model using the linear combination of atomic orbitals (LCAO) technique [141, 142]. The required parameters and matrix elements of the Hamiltonian $H_{ij}(\mathbf{k})$ and overlap matrix $S_{ij}(\mathbf{k})$ for the fcc crystal are tabulated in [143] for the employed basis set of nine orbitals $(s, p_x, p_y, p_z, d_{xy}, d_{yz}, d_{zx}, d_{x^2-z^2}, d_{z^2-r^2})$. This approach is well-chosen because it can reproduce full ab-initio calculations precisely with an average deviation of $7\,\mathrm{meV}$ and a maximum error of $15\,\mathrm{meV}$.

The fundamental idea of the tight-binding approach is to expand the Bloch electrons of the solid $\Psi_{\mathbf{k}}(\mathbf{r})$ by a linear combination of atomic orbital wave functions $\varphi_n(\mathbf{r})$.

With quantum numbers $n = 1...9$, the coefficients $b_n(\mathbf{k})$ and the atomic positions $\mathbf{R_i}$, the wave function is given by

$$\Psi_\mathbf{k}(\mathbf{r}) = \sum_{\mathbf{R_i}} e^{i\mathbf{k}\mathbf{R_i}} \phi(\mathbf{r} - \mathbf{R_i}) \tag{3.28}$$

$$= \sum_{\mathbf{R_i}} e^{i\mathbf{k}\mathbf{R_i}} \sum_n b_n(\mathbf{k}) \varphi_n(\mathbf{r} - \mathbf{R_i}) \tag{3.29}$$

With this ansatz for the wave functions, the Hamiltonian and overlap matrices $H_{m,n}(\mathbf{k})$ and $S_{m,n}(\mathbf{k})$ are calculated. For each $\mathbf{k}$, we obtain as a result nine energies (for nine energy bands) and nine eigenvectors, which consist of coefficients that determine how strongly each orbital contributes to this state $E_n(\mathbf{k})$. The band of particular interest is the 6th band because here the Fermi level is found ($E_6 = -2.3\,\text{eV}$ to $4.0\,\text{eV}$). The computation time is short because the calculation involves only $9{\times}9$ matrices. Furthermore, the Brillouin zone (BZ) can be reduced to an irreducible part which reproduces the full symmetry by 48 different rotations.

For every $\mathbf{k}$-direction the length that matches a given energy $E(\mathbf{k}) = \varepsilon$ is determined via a root-finding algorithm. This way, we obtain an isoenergy contour in k-space from which the Green's function as single-particle propagator can be calculated using Eq. 3.19, as described in the following subsection. The results for the band structure are discussed in Sec. 3.6.

The density of states for an energy ε is given by

$$\text{DOS}(\varepsilon) = \frac{2}{(2\pi)^3} \cdot \sum_{\mathbf{k}|E(\mathbf{k})=\varepsilon} \frac{J(\mathbf{k})}{|\mathbf{v}_{\text{Gr}}(\mathbf{k})|} \tag{3.30}$$

Here, the Jacobian matrix for each k-space element is denoted by $J(\mathbf{k})$. The coefficient of Jacobian and group velocity determines the size of the k-space element.

3.5.2 Single-Particle Propagator

The imaginary part of the propagator is connected to the states of the band structure by Eq. 3.20. Inserting two positions $\mathbf{x}$ and $\mathbf{x}'$ and replacing the Bloch waves $\Psi_\mathbf{k}$ with

a lattice periodic part $u_{\mathbf{k}}(\mathbf{x})$ and an exponential term as phase yields

$$\operatorname{Im} G_0(\mathbf{x}, \mathbf{x}', \varepsilon) = -\pi \sum_{\mathbf{k}} \Psi_{\mathbf{k}}(\mathbf{x}) \Psi_{\mathbf{k}}^*(\mathbf{x}') \delta(\varepsilon - E(\mathbf{k})) \tag{3.31}$$

$$= -\pi \sum_{\mathbf{k}|E(\mathbf{k})=\varepsilon} u_{\mathbf{k}}(\mathbf{x}) u_{\mathbf{k}}^*(\mathbf{x}') e^{i\mathbf{k}(\mathbf{x}-\mathbf{x}')} \tag{3.32}$$

At this point a significant simplification is introduced: the lattice periodic part is omitted. This is why we call this model a *plane wave tight-binding model*. As the propagator only depends on the difference $\mathbf{x} - \mathbf{x}'$, its imaginary part is then given with a coefficient describing the spectral weight by

$$\operatorname{Im} G_0(\mathbf{x} - \mathbf{x}', \varepsilon) = -i\pi \sum_{\mathbf{k}|E(\mathbf{k})=\varepsilon} \frac{J(\mathbf{k})}{|\mathbf{v}_{\mathrm{Gr}}(\mathbf{k})|} e^{i\mathbf{k}(\mathbf{x}-\mathbf{x}')} \tag{3.33}$$

The real part of G_0, which is needed for the calculation of the scattering term $G_0 T G_0$, can be obtained by the Kramers-Kronig relation [144, 145] that connects the real and imaginary part of a complex function that is analytic in the upper half-plane:

$$\operatorname{Re} G_0(\mathbf{x}, \mathbf{x}', \varepsilon) = \frac{1}{\pi} \mathcal{P} \int_{-\infty}^{\infty} \frac{\operatorname{Im} G_0(\mathbf{x}, \mathbf{x}', \varepsilon)}{\varepsilon - \varepsilon'} \, \mathrm{d}\varepsilon' \tag{3.34}$$

For this, $\operatorname{Im} G_0$ has to be calculated for the whole energy range, which increases the computation time significantly, but leads to the most accurate results. This is why for most of the data shown in this thesis, this approach is employed. An alternative, for which the calculation of only one isoenergy contour is necessary, is a heuristic approximation of the real part, which has shown to be appropriate [134]:

$$G_0(\mathbf{x}, \mathbf{x}', \varepsilon) \approx -i\pi \sum_{\mathbf{k}|E(\mathbf{k})=\varepsilon} \frac{J(\mathbf{k})}{|\mathbf{v}_{\mathrm{Gr}}(\mathbf{k})|} |a(\mathbf{k})| \left[e^{i|\mathbf{k}(\mathbf{x}-\mathbf{x}')+\arg(a(\mathbf{k}))|} - \frac{i}{|\mathbf{k}||\mathbf{x}-\mathbf{x}'|} \right] \tag{3.35}$$

Here, $a(\mathbf{k})$ denotes a complex coefficient for scaling and $\arg(a(\mathbf{k}))$ its complex phase. In comparison to experimental topographies, it is found that both ways to calculate $\operatorname{Re} G_0$ yield similar results for fitted quantities like the effective scattering phase shift η or the surface parameter a_{surf}, which are introduced below. This underlines the quality of the approximative approach. The largest differences between both methods are encountered in the proportions of the peak amplitudes where the full solution fits more accurately to the experimental data.

The scattering matrix T describes in our context a single point scatterer at

position $\mathbf{x_i}$ and is assumed to scatter all states in an identical manner. Thus, it can be written as a single complex number $t_{\mathrm{imp}}(\varepsilon)$. Its amplitude and phase describe the scattering amplitude and scattering phase shift of the interaction of electrons and impurity. Hence, according to Eq. 3.25, the full propagator from a position $\mathbf{x}'$ to $\mathbf{x}$ is a sum of a free propagation for this path and propagation to the impurity, a scattering event, and subsequently to the final position:

$$G(\mathbf{x}, \mathbf{x}', \varepsilon) = G_0(\mathbf{x}, \mathbf{x}', \varepsilon) + G_0(\mathbf{x}, \mathbf{x_i}, \varepsilon) t_{\mathrm{imp}}(\varepsilon) G_0(\mathbf{x_i}, \mathbf{x}', \varepsilon) \qquad (3.36)$$

In the STM experiment, we probe the standing wave patterns of the propagation from a point on the surface $\mathbf{x}$ to the impurity at $\mathbf{x_i}$ and back to the same position. This is why we have to consider $G(\mathbf{x}, \mathbf{x}, \varepsilon)$ that yields

$$\varrho(\mathbf{x}, \varepsilon) = -\frac{1}{\pi} \operatorname{Im} G(\mathbf{x}, \mathbf{x}, \varepsilon) = \varrho_0(\varepsilon) + \Delta\varrho(\mathbf{x}, \epsilon) \qquad (3.37)$$

The first summand originates from the free propagation and is constant because the lattice periodic part of the propagator is omitted. It relates to a constant background of DOS in the STM data, while the second term equals the measured ΔLDOS of the interference patterns at the surface. Because G_0 is identical for the propagations from and to the impurity due to time-inversion symmetry, the surface signatures are described by

$$\Delta\varrho(\mathbf{x}, \varepsilon) = -\frac{1}{\pi} \operatorname{Im}[t_{\mathrm{imp}}(\varepsilon) G_0(\mathbf{x_i}, \mathbf{x}, \varepsilon)^2] \qquad (3.38)$$

The scattering matrix $t_{\mathrm{imp}}(\varepsilon)$ is introduced as energy-dependent complex number with constant amplitude and phase for all scattered waves. In the following, we will parametrize the t-matrix with an effective scattering phase shift η for which holds

$$t_{\mathrm{imp}} = 1 \cdot \exp(i\eta) \qquad (3.39)$$

Since t_{imp} now consists of only one complex phase, this implies a number of simplifications for the scattering process. We neglect the scattering amplitude which is responsible for the absolute height of the calculated ΔLDOS. For comparisons with experimental data, the simulated signal is scaled accordingly, so in principle it would be possible to obtain a value. However, quantifying a comparison of different experimental data sets is difficult because the topographic heights depend on many

parameters like set point and tip quality, so that an extracted value of the scattering amplitude would not be very meaningful.

Furthermore, η is chosen independent of energy. For the small energy interval of approximately $\pm 300\,\mathrm{mV}$ that we usually consider in STS data, this assumption is reasonable because we cannot identify resonances in this energy range in either the experimental data or the ab-initio data (c.f. Sec. 3.7), which would introduce a phase shift. Moreover, assuming no dependence on energy is convenient for the comparison of topography data of different bias voltages.

3.5.3 Surface and Vacuum Barrier

Equation 3.38 yields the change in LDOS within the sample or exactly at the surface because the propagator G_0 belongs to the crystal and thus does not describe the vacuum barrier. Hence, in order to simulate the STM data, the **k**-dependent decay into the vacuum has to be included. The momentum component parallel to the surface $\mathbf{k}_{||}$ is assumed to be conserved while the decay constant perpendicular to the surface κ is given by

$$\kappa(\mathbf{k}_{||}, E) = \sqrt{\frac{2m}{\hbar}(\Phi - (E - \mu)) + \mathbf{k}_{||}} \tag{3.40}$$

with the work function Φ as potential barrier between sample and vacuum and $(E - \mu)$ as difference between the electron energy and the electrochemical potential. This equation describes which lateral frequencies are mapped by the STM. For high $\mathbf{k}_{||}$, one obtains a larger κ and therefore a quicker decay into the vacuum. This means that lateral oscillations with high frequency are less likely to be detected at higher tip heights h. Oscillations with low frequency and longer wavelengths are visible even for larger distances.

It can be shown that increasing the tip height h acts approximately like a Gaussian filter to the measured signal [130]. With this in mind, it is intuitive that features with small wavelengths are blurred first. Furthermore, this means that the set point $(U_{\mathrm{Bias}}/I_{\mathrm{Set}})$, which is decisive for the tip height, plays a similar role for the resolved lateral patterns as the bluntness of the tip. Of course, optimal imaging conditions with the least possible loss of signal due to decay in the vacuum are given with small bias voltages, high tunneling currents and sharp tips.

The effect of different tip heights is visualized in Fig. 3.4. The details of the interference patterns, shown in 2D in (a-d) and in lateral sections in (e), will be
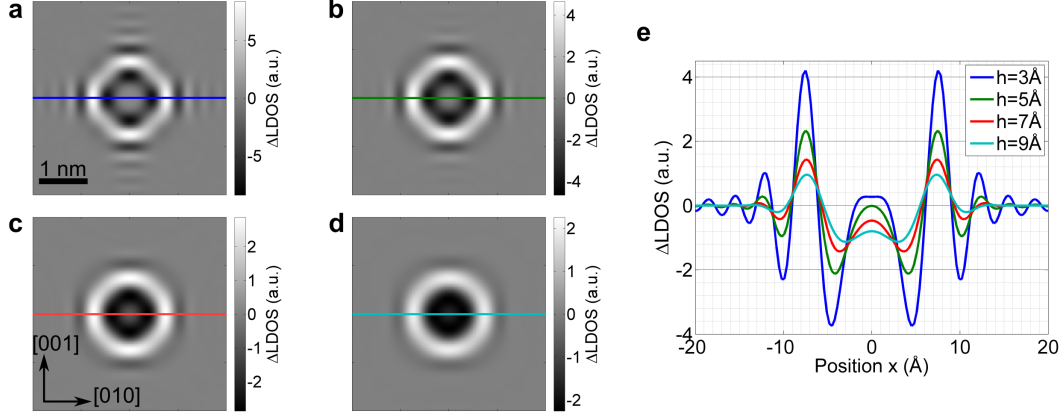
Figure 3.4: Effect of the tip height h on the STM data. (a–d) Simulated interference patterns ($4 \times 4\,\mathrm{nm}^2$, $E = 0\,\mathrm{eV}$) for an exemplary impurity in the 7th monolayer of Cu(100) for $h = \{3, 5, 7, 9\}\,\text{Å}$. (e) Sections along [010] direction as labeled in the 2D graphs. For higher distances from the surface, the measurement signal decreases in amplitude and features appear broader.

discussed later in Chap. 5. Nevertheless, we can already see at this point that a larger distance from the surface leads to a smaller amplitude of the signal, less high-frequency features and a generally blurrier picture.

Having described both the propagation in the crystal and the decay of states into the vacuum separately, these processes have to be combined for a full simulation of the STM data. For the implementation of such a semi-infinite crystal geometry, the wave functions inside the crystal $\Psi_{\mathbf{k}}^C$ and within the vacuum $\Psi_{\mathbf{k}}^V$ are given with a normalization constant $n(\mathbf{k}) = (V(1 + |a(\mathbf{k})|^2))^{-\frac{1}{2}}$ with crystal volume V and the reflection and transmission coefficients $a(\mathbf{k})$ and $b(\mathbf{k})$ at the (100) surface by

$$\Psi_{\mathbf{k}}^C(x, y, d) = n(\mathbf{k})e^{i(k_x x + k_y y)} \left[e^{-ik_z d} + a(\mathbf{k})e^{ik_z d} \right] \tag{3.41}$$

$$\Psi_{\mathbf{k}}^V(x, y, h) = n(\mathbf{k})b(\mathbf{k})e^{i(k_x x + k_y y) - \kappa(\mathbf{k})h} \tag{3.42}$$

These wave functions can be inserted into the spectral representation of G_0 in Eq. 3.19. Hence, we obtain the Green's functions for propagations from the crystal into vacuum (CV) (impurity $\mathbf{x_i}$ to tip $\mathbf{x_t}$) and from vacuum to vacuum (VV) (without scattering, at the tip's position)

$$G^{CV}(\mathbf{x_t}, \mathbf{x_i}, \varepsilon) = \int_{\mathbf{k}} d\mathbf{k} G_0(\mathbf{k}, \varepsilon) \Psi_{\mathbf{k}}^V(\mathbf{x_t}) \Psi_{\mathbf{k}}^{*C}(\mathbf{x_i}) \tag{3.43}$$

$$G^{VV}(\mathbf{x_t}, \mathbf{x_t}, \varepsilon) = \int_{\mathbf{k}} d\mathbf{k} G_0(\mathbf{k}, \varepsilon) \Psi_{\mathbf{k}}^V(\mathbf{x_t}) \Psi_{\mathbf{k}}^{V*}(\mathbf{x_t}) \tag{3.44}$$

Inserting the wave function into G^{VV} yields the LDOS at the position of the tip $\mathbf{x}$ in height h for the sample without the impurity:

$$\varrho_0(h, \epsilon) = -\frac{1}{\pi} \operatorname{Im} G^{VV}(\mathbf{x}, \mathbf{x}, \varepsilon) = \int_{\mathbf{k}} d\mathbf{k} \delta(\varepsilon - E(\mathbf{k})) |n(\mathbf{k})b(\mathbf{k})|^2 e^{-2\kappa(\mathbf{k}h)} \qquad (3.45)$$

For the propagation from an impurity located at $(x, y, d) = (0, 0, d)$ to the tip at (x, y, h), the propagator reads

$$G^{CV}(x, y, h, d, \varepsilon) = \int_{\mathbf{k}} d\mathbf{k} G_0(\mathbf{k}, \varepsilon) |n(\mathbf{k})|^2 b(\mathbf{k}) e^{i(k_x x + k_y y + k_z d) - \kappa(\mathbf{k})h} \qquad (3.46)$$

Thus, the local density of states measured by the tip with scattering at an impurity with scattering matrix t_{imp} is given by

$$\varrho(x, y, h, \varepsilon) = \varrho_0(h, \varepsilon) + \left(-\frac{1}{\pi} \operatorname{Im} \left[(G^{CV}(x, y, h, d, \varepsilon))^2 t_{\text{imp}} \right] \right) \qquad (3.47)$$

3.5.4 Implementation

The expression in Eq. 3.47 is used to simulate STS data resolving the energy-dependence of an impurity's interference pattern. We only consider the second term which describes the defect-induced oscillations on the constant background of the first term. For the calculation of topography data, we use the simplest approach available by summing all contributions between $E = E_F$ and the set point $E = E_F + eU_{\text{Bias}}$. This way we neglect any energy-dependent transmission. This approximation holds best for bias voltages close to $U_{\text{Bias}} = 0\,\text{V}$, but proves to be suitable for energies at least within $E = \pm 300\,\text{meV}$. A typical energy step for the calculation is $\Delta E = 25\,\text{meV}$.

All parameters of the plane wave tight-binding model are depicted in the sketch in Fig. 3.5. Typical distances for the tip height h are $5 - 8\,\text{Å}$ [43]. The impurity has an effective scattering phase shift η that can take values from 0π to 2π. When located in the nth monolayer (ML), the depth d is given by $d = (\text{ML} - 1)a_{[100]} + a_{\text{surf}}$ because impurity atoms are assumed to sit substitutionally in the Cu single crystal. The lattice parameter is $a_{\text{Cu}} = 3.61\,\text{Å}$ and for Cu(100) the monolayer distance reads $a_{[100]} = 0.5a_{\text{Cu}} = 181\,\text{pm}$. The surface layer is referred to as 'first layer'.

In contrast to $a_{[100]}$, the value of a_{surf} is initially not known and has to be estimated. A rough approximation is given by the spatial extent of the crystal potential with $a_{\text{surf}} = 1.0a_{[100]}$ [146]. In Chap. 5, by comparison with experimental data, it is shown
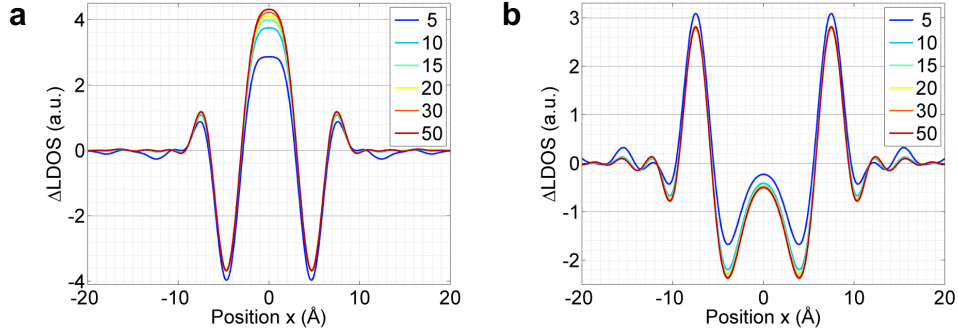
Figure 3.5: Sketch of the plane wave tight-binding model. The tip probes the ΔLDOS in height h above the sample. The impurity with an effective scattering phase shift of η is located in a depth d. The surface layer is referred to as first layer.

that this estimate is appropriate.

It has to be noted that the system is not uniquely determined by the parameters. For example, a small variation in a_{surf} can be compensated by a change in scattering phase shift η. An additional distance of electron propagation lets the wave function collect an additional phase. Its value is significant because Cu's Fermi wavelength of $\lambda_{\mathrm{Cu}} = 4.6\,\text{Å}$ is of the order of the nearest-neighbor distances. A step of $0.1\,\text{ML}$ in depth approximately corresponds to $-0.14\,\pi$ for the effective scattering phase shift η. This shows that the parameters of the plane wave tight-binding model are not independent of each other and more than one parameter set can be found to describe the data accurately. Nevertheless, some constraints limit these liberties, e.g. the focusing angle determines a certain lateral size of the interference pattern which excludes extreme values of a_{surf}.

The phase shift η includes all phase contributions within and outside the solid that are collected during propagation. Firstly, an additional phase shift is obtained at the transmission from the metal crystal into the vacuum [147]. Secondly, in contrast to the ab-initio KKR calculations, in the tight-binding model the electron also collects a phase during its propagation in the impurity cell. Both of these contributions are considered to be similar for all investigated impurity species. Hence, while a comparison of absolute values is not possible between the different calculation methods, differences between observed scattering phases of different species can be compared.

Figure 3.6: Effect of the number of k-points for the resolution. Simulated interference pattern of an exemplary impurity in (a) 4th ML and (b) 7th ML for ($h = 5\,\text{Å}$, $\eta = 1.25\pi$, $U = 0\,\text{V}$). For 20×20 k-points or higher, the resolution does not improve further.

From a computational point of view, the resolution in k-space is one crucial component that determines the precision of the simulation. The number of k-points is given by the parametrization (φ, ϑ) of the irreducible part of the first Brillouin zone. In [134], it was already shown via the density of states that a resolution of 10×10 k-points is similar to 20×20 k-points which shows good results and was used in those calculations. In this thesis, we usually use 20×20 k-points and for some calculations even 30×30. This means, because of the irreducible part of the Fermi surface, that we calculate the tight-binding simulations with a number of k-vectors between 19200 and 43200 for one energy. The differences of k-resolution are visualized in the final ΔLDOS patterns for different impurity depths shown in Fig. 3.6. While all patterns show similar structures, for $N = 5$ the amplitude deviates strongly. For $N = 10$ and $N = 15$ the data already improves significantly. For values of $N \geq 20$, there is almost no difference to be found. For the contrast of color maps of 2D data small differences like between $N = 15$ and $N = 20$ are irrelevant.

3.6 Orbital-Resolved Electron Propagation in Cu

Using the tight-binding model, we can characterize the Fermi surface as well as its orbital character which is needed for an orbital-resolved description of the electron propagation within the crystal. The Fermi surface of Cu is depicted in Fig. 3.7(a). The most peculiar difference to a spherical contour are the characteristic band gap 'necks' in the $\langle 111 \rangle$ directions. The color-coded angle of the group velocity shows the propagation direction of the corresponding electronic state. While around the
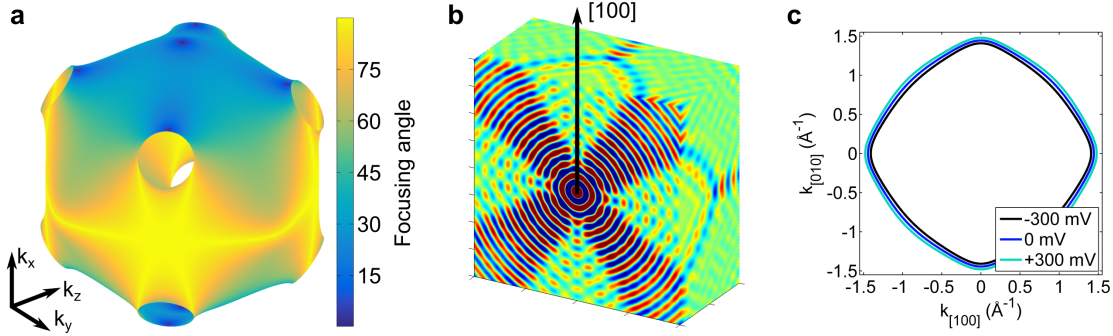
Figure 3.7: (a) Fermi surface of Cu calculated with tight-binding model. Color code depicts the group velocity's angle with respect to the [100] direction. (b) Real space propagator $\mathrm{Im}\, G_0(\mathbf{x}, \mathbf{x}', E_F)$ with four-fold focusing directions. (c) Sections through isoenergy contours along $k_{[001]} = 0$ for energies $E = -300...300\,\mathrm{mV}$ show similar shape with increasing size.

necks and in the $\langle 100 \rangle$ directions, the angle is close to $0°$, the regions between the necks (in $\langle 110 \rangle$ directions) reveal flat surface areas of focusing angles of $30°$ and $60°$. These electronic structure anisotropies are sufficient to cause the strongly directional real space electron propagation which is visualized in Fig. 3.7(b) with a four-fold focusing pattern. The isoenergy contours for different energies in Fig. 3.7(c) illustrate that for the mainly considered energy range of $E = \pm 300\,\mathrm{meV}$ the shape is identical while the size increases moderately with energy, so that the focusing behavior is not expected to change.

For an orbital-resolved description of electron propagation, we have to identify the orbital character of each state in the band structure. This is given by the eigenvector that is calculated for each $E(\mathbf{k})$ in the tight-binding model. Each of the nine coefficients b_n determines how strongly that atomic orbital wave function contributes to this state. As the eigenvector is normalized, the coefficient $|b_n|^2$ is used to scale a states' contribution for the calculation of the DOS or a propagator.

The DOS of the sample, which apart from surface effects is similar to the background contribution ϱ_0 described in Sec. 3.5.2, is split into orbital contributions as plotted in Fig. 3.8(a). Our results are in agreement with the literature [148]. The d bands of Cu's ten $3d$ electrons are mainly located between $E = -8\,\mathrm{eV}$ and $E = -2\,\mathrm{eV}$. A corresponding peak is found in the DOS and decreases to higher energies where the sp contributions become more important. For the detection by STM, the $\mathbf{k}_{\parallel}$-dependent decay into the vacuum has to be considered [130]. As shown in Fig. 3.8(b), the electrons of d character fade more quickly, so that for larger heights they become weaker in comparison to sp contributions, yet their signal still holds
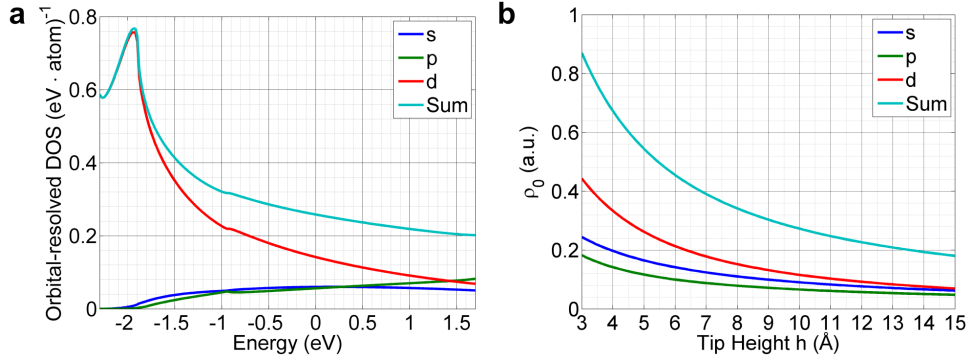
Figure 3.8: (a) Orbital-resolved DOS(E). The d states' contribution decreases with energy, yet is still the major contribution for $E = E_F$. (b) Tip height-dependent background contribution $\varrho_0(h)$ for $E = E_F$. The decay of d states is stronger than for sp contributions.
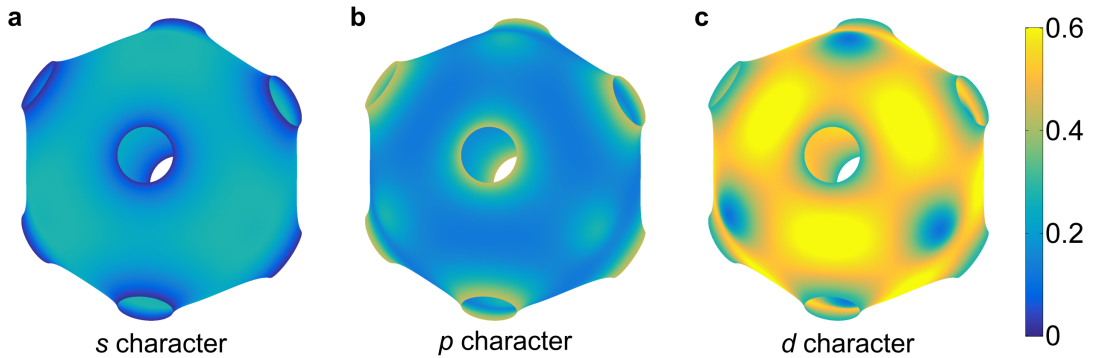

Figure 3.9: Fermi sphere of Cu resolved by electron orbital for the share of (a) s, (b) p, and (c) d character of the electronic state.

the largest share.

The orbital-resolved Fermi surfaces in Fig. 3.9 show in agreement with the literature [149, 150] that the electronic characters are not uniformly distributed in k-space. The p character is mostly present at the necks in $\langle 111 \rangle$ directions, while the s character is located on the rest of the Fermi sphere. Both characters have generally a smaller share than the d character which shows weak signal in the $\langle 100 \rangle$ directions and the necks. It shows an exceptionally strong signal in the $\langle 110 \rangle$ directions (between the necks) that coincide with the flat focusing regions found in Fig. 3.7(a).

The states in the focusing regions are crucially responsible for the ΔLDOS at the surface from impurity scattering because due to their directional propagation the signal sustains for distances of more than multiple nanometers from the buried defect through the crystal. As these flat areas of the Fermi surface are dominated by
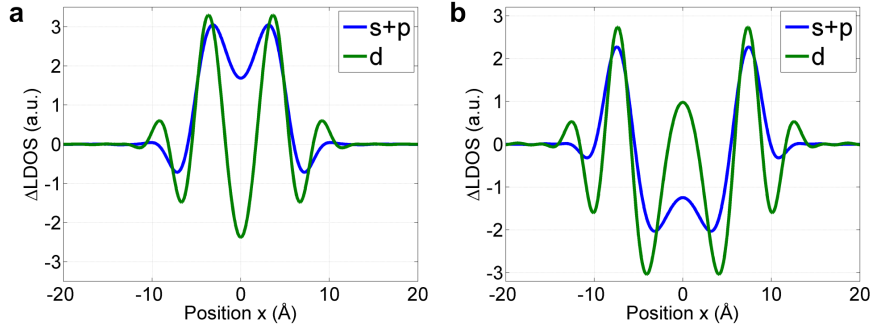
Figure 3.10: Orbital-resolved tight-binding interference pattern along [010] direction for (a) 5th ML and (b) 7th ML exemplary impurities ($\eta = 1.25\pi$) for $E = 0\,\text{eV}$ and a tip height $h = 7\,\text{Å}$. While the center part is mixed with sp and d contributions, the outmost peak is only displayed by electrons of d character.

d character, also the surface interference patterns are governed by this orbital as shown in calculations for exemplary impurities in the 5th and 7th ML in Fig. 3.10. Here, an identical effective scattering matrix η is chosen for all orbitals. The contributions of s and p orbitals are similar in shape for this [010]-section, which is why their sum is plotted.

Furthermore, the apparent focusing angle is larger for d electrons than for sp. While in the center area the interference pattern is composed of all three orbital characters, for larger angles ($x \approx 9\,\text{Å}$ for $5\,\text{ML}$ and $x \approx 12\,\text{Å}$ for $7\,\text{ML}$) only the d orbital shows a signal. For both examples this additional oscillation is detected in comparison to the ΔLDOS from sp. This insight will prove profoundly useful later on for the discussion of the data for Ge impurities.

For Fig. 3.10, each orbital's pattern was calculated with an orbital-specific propagator for both ways between impurity and surface. One can go one step further and split the propagator not only in s, p and d, but each of the nine single atomic orbitals of the tight-binding basis set. This reveals the symmetries of each of these orbitals as illustrated in Fig. 3.11. While the surface pattern for s-like states is almost isotropic, orbital characters with distinct orientations, e.g. the p-orbitals, show clearly preferred lateral directions. The p-orbital characters are identical when examined in the bulk, but show for the chosen surface of Cu(100) mostly a four-fold pattern from p_x. The scale for ΔLDOS varies significantly for orbitals that are located within the surface plane or perpendicular to it.

From a simple look at the amplitudes of the patterns, it becomes apparent that the surface signatures of subsurface impurities consist mainly of contributions from d_{xy} and d_{zx} as well as s and p_x. This matches with the strong d component for the
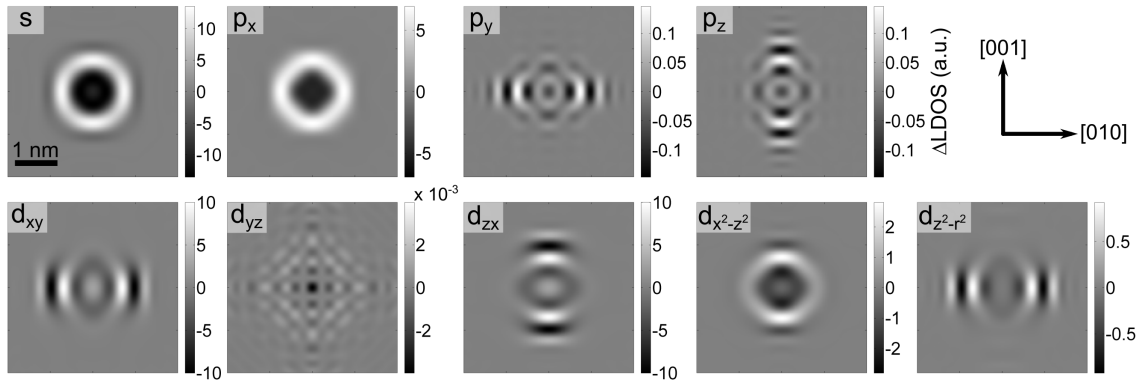
Figure 3.11: Orbital-resolved topographies ($4 \times 4 \, \text{nm}^2$) at $U = 0 \, \text{mV}$ for exemplary 7th ML impurity with $\eta = 1.25\pi$ and tip height $h = 7 \, \text{Å}$. The scale in ΔLDOS varies significantly between different contributions.

most important focusing regions on the Fermi sphere. Despite the single characters' different symmetries, for each orbital (s, p, d) the overlap of all characters creates a similar pattern, as we have shown in the 1D section (Fig. 3.10). Only for the most outward area, the signal is only given by the sum of d orbitals. This will be helpful to understand the experimental data where simply the ΔLDOS is measured without any additional information about electronic orbitals.

3.7 Ab-Initio Calculations (KKR-DFT)

Complementary to the plane wave tight-binding simulations, ab-initio calculations of the investigated systems were performed by M. Bouhassoune and S. Lounis from the Peter Grünberg Institute and Institute for Advanced Simulation at Forschungszentrum Jülich. They use density functional theory (DFT) in the local density approximation (LDA) [151] with the full potential Korringa-Kohn-Rostoker Green's function method (FP-KKR-GF) [152]. The KKR method is a band structure method that is based on the multiple scattering theory introduced by Korringa [153] and Kohn and Rostoker [154]. In this framework, first, scattering at each atomic potential is described separately by a scattering matrix. Then, for the multiple scattering approach considering all atoms of the solid, it is assumed that the incoming wave for each scattering center is the sum of all outgoing waves from the other atoms. Using this approach in the scope of the Green's function formalism yields a strong increase in computational efficiency since the evaluation of spatially resolved wave functions can be avoided. We have already shown in Sec. 3.4 how easily in this approach a

perturbation of the system (e.g. scattering at T) can be connected with the free solution (G_0). This description of the sample system fits perfectly to our investigation of a single impurity as scatterer in an otherwise homogeneous system, as already shown by Zeller et al. in 1979 [155]. Over the last decades, the KKR method has been used in many ways, e.g. with the coherent potential approximation (KKR-CPA) for the description of randomly disordered alloys, and has been steadily developed further. While first calculations used muffin-tin potentials, here a self-consistent full potential approach is employed.

On a technical level, first, the band structure is calculated by Cu slabs of 18 fcc layers with three additional vacuum layers on each side of the Cu slab. The lattice parameter is set to $a_{Cu} = 3.61$ Å without surface relaxations. In a second step, an impurity is inserted into the selected depth and the charge in the cluster of impurity and neighboring atoms is updated self-consistently. The STM data is obtained by the charge density in height $h = a_{Cu}$ above the surface according to the Tersoff-Hamann approach.

The fundamentals of FP-KKR-GF have been outlined elsewhere [140, 152, 156], so only few aspects other than the results are discussed here.

The single-site scattering is described by a spherical atomic potential in an environment of a constant potential. This is very similar to the known textbook example of elastic scattering at a radially symmetric potential [157]. The suitable choice for dealing with such symmetry is the use of spherical Bessel functions as basis set, so that the solution of the Schrödinger equation is expanded over the angular momentum indices (l, m) with radial wave functions $R_l(r, E)$. Typically, only the orbitals $l = 0, 1, 2$, i.e. s, p and d orbitals, are considered. For asymptotic distances $r \to \infty$ the wave functions are given by

$$R_l(r, E) \to \frac{A_l}{\sqrt{E}r} \sin\left(\sqrt{E}r - \frac{l\pi}{2} + \delta_l(E)\right). \tag{3.48}$$

Here, A_l is a constant and $\delta_l(E)$ the scattering phase shift, which denotes the phase shift between the wave function with and without the potential. These scattering phase shifts comprise the full information about the scattering potential. For this reason it can be shown that the complex entries t_l of the scattering T-matrix, as introduced in Sec. 3.4, are determined by the scattering phase shifts:

$$t_l(E) = -\frac{1}{\sqrt{E}} \sin(\delta_l(E)) e^{i\delta_l(E)} \tag{3.49}$$

Species/Layer	s	p	d
Cu 3ML	-0.086	0.070	-0.180
Cu 5ML	-0.084	0.074	-0.180
Ag 3ML	-0.20	-0.04	-0.22
Ag 5ML	-0.20	-0.01	-0.22
Ge 3ML	0.87	0.85	0.045
Ge 5ML	0.87	0.86	0.044

Table 3.1: Scattering phase shifts δ_l from ab-initio calculations at Fermi energy E_F for different species in 3rd and 5th ML.

This orbital-specific scattering matrix is not yet the quantity to be placed into the Dyson equation to simulate the experiment because the KKR approach assumes scattering at every atomic potential, i.e. also the host's atoms. Therefore the decisive quantity to describe the *difference* in scattering due to the impurity reads

$$\Delta T_l(E) = t_{\text{imp},l}(E) - t_{\text{host},l}(E). \tag{3.50}$$

Thus, if one inserts an impurity with identical scattering properties like the host, there will not be any perturbation. However a vacancy with $t_{\text{vac},l} = 0$ will cause scattering with an effective scattering matrix of $\Delta T_l = -t_{\text{host},l}$. The effective scattering amplitude is given by $|\Delta T|$ and the effective scattering phase by the complex argument $\arg(\Delta T)$.

For a comparison of the scattering phases in the tight-binding model and the ab-initio calculations, we have to compare the tight-binding effective scattering matrix $T_{\text{TB}} = \exp(i\eta)$ and the KKR scattering matrix ΔT. In the following, we will discuss the results for our sample system of Ag and Ge impurities in Cu as host material.

The scattering phases δ_l obtained from the ab-initio calculations for $E = E_F$ are given in Tab. 3.1. These are consistent with previous simulations in the literature by Braspenning et al. [158]. The comparison of 3rd ML and 5th ML shows that the scattering phase is almost independent of depth. For atoms deeper within the crystal the effect of the surface is assumed to decrease even further. The energy-dependent plots in Fig. 3.12 show that for most orbitals the scattering phase is approximately constant in the considered interval of $E = \pm 1\,\text{eV}$. Hence, this supports the assumption for the tight-binding effective scattering phase shift to be independent of energy.
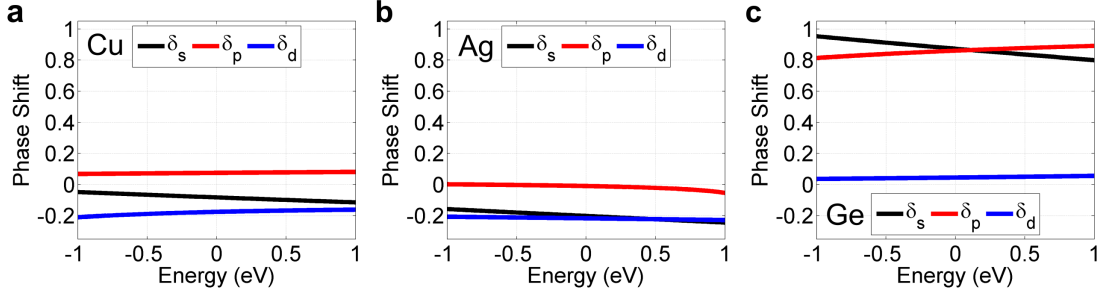
Figure 3.12: Scattering phases $\delta_{\{s,p,d\}}(E)$ obtained by KKR-DFT for (a) Cu, (b) Ag, and (c) Ge in the 5$^{\text{th}}$ ML. The phases are mostly constant over energy which supports the assumption for the tight-binding model of a constant effective scattering phase shift η.

Species		s	p	d
Ag in Cu	$|\Delta T|$	0.12	0.08	0.04
	$\arg(\Delta T)$	1.91π	2.02π	1.87π
Ge in Cu	$|\Delta T|$	0.82	0.71	0.22
	$\arg(\Delta T)$	1.25π	1.30π	0.96π

Table 3.2: Effective scattering phase shifts $\Delta T = t_{\text{imp}} - t_{\text{Cu}}$ from ab-initio calculations at the Fermi energy E_F for 5$^{\text{th}}$ ML Ag and Ge impurities species in Cu. $|\Delta T|$ is stated in arbitrary units.

As explained above, the implications for the scattering patterns are given by the properties of the difference of scattering matrices ΔT. These values are given in Tab. 3.2. For Ag impurities in Cu, all effective scattering phases are very similar. Furthermore, the scattering amplitudes are rather small in comparison to Ge impurities in Cu. Especially strong scattering for Ge is found for s and p orbitals which matches with the electronic configuration of Ge with one additional 4s and two 4p electrons with respect to Cu. The effective scattering phases for Ge differ from the Ag values. Most peculiar is the inversion of $\arg(\Delta T_d)$ for both species. This would correspond to an inverted interference pattern as surface signature (for the d contribution). On first sight, this might be surprising because the values of δ_d (c.f. Tab. 3.1, Fig. 3.12) seem rather similar for both species. However, this effect is easily explained when exploring the details how ΔT is calculated.

Each term, t_{imp} and t_{Cu}, is a complex number which is only parametrized by one value, namely δ. According to Eq. 3.49, the value of t is periodic in δ with a periodicity of 1π. Hence, when the scattering phases δ_{Cu} for the host are fixed, the value of ΔT can only lie on a specific circle in the complex plane with each
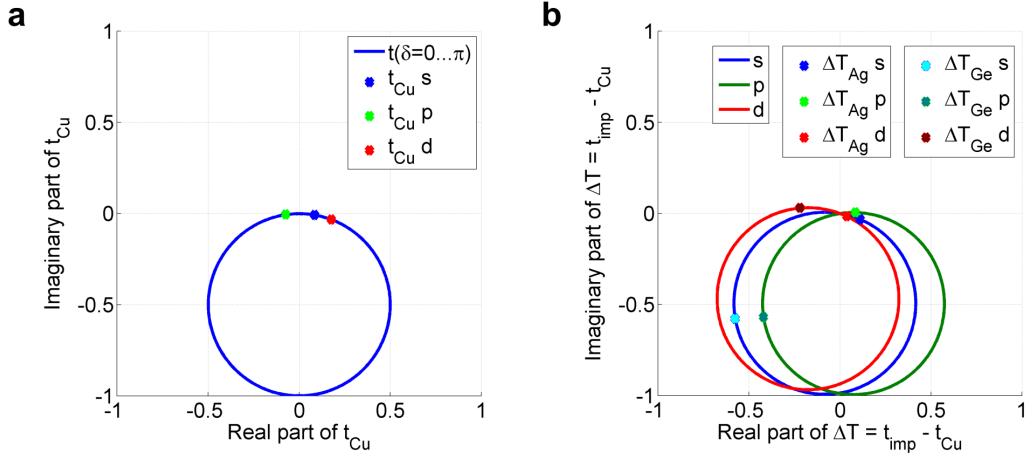
Figure 3.13: Depiction of scattering matrices in the complex plane. (a) Values of t_{Cu} and possible values for any value of δ (blue circle). (b) Values of $\Delta T = t_{imp} - t_{Cu}$ for Ag and Ge in Cu. Although the points for both d orbitals are located close to each other, the shift over the horizontal axis leads to an inversion in the effective phase shift $\arg(\Delta T)$ with respect to the other species.

point of the circle corresponding to one value of $\delta_{imp} = 0...1\pi$. This is illustrated in Fig. 3.13(a), where the values for t_{Cu} are plotted in the complex plane, and in Fig. 3.13(b) where the circles depict any possible difference of t_{imp} and t_{Cu}. For the s and p orbitals the points for Ag are found close to the origin, implying a small perturbation with respect to Cu, while for Ge the points sp lie well within the plane. The inversion between Ag and Ge that we observed for the d orbital finds its reasoning in the crossing of the horizontal axis in the complex plane. Although the values of $\delta_{Ge,d}$ and $\delta_{Ag,d}$ are similar, their small difference shifts ΔT into another quadrant and therefore to a strongly changed effective scattering phase shift.

With the knowledge of the scattering phases δ and the scattering matrices t, the KKR-DFT ab-initio calculations can predict the experimental STM and STS data. These results will be shown and discussed in the context of the experimental data in Chap. 6.

3.8 Electron-Phonon Coupling

In this last section of the chapter, we describe electron-phonon coupling. This many-body effect influences the band structure of the host, which can be described by including a self-energy Σ into the single-particle propagator G. This is introduced in the following, before we present experimental data from the literature that shows the signature of electron-phonon coupling in the electronic structure.

3.8.1 Many-Body Description

In a single-particle approach, the interaction of electrons with phonons is characterized by a mean scattering time τ. Free electrons move within the solid and every time interval τ or propagation distance $v_F \tau$ a scattering event occurs which also limits the coherence length of an electronic state. This classical depiction of electron-phonon interaction is very graphic and is therefore even used to describe the results of elaborate many-body calculations, as in [150].

An alternative formulation of electron-phonon interaction is to include it into the electron band structure. Phonons are lattice vibrations, i.e. the movement of the ions that create the crystal lattice potential, which in turn determines the electronic states. This allows to calculate an electronic structure that already incorporates the interaction with the (vibrating) lattice, so that no further scattering events have to be described. We will find that the dispersion relation $E(\mathbf{k})$ changes symmetrically around the Fermi level, exhibiting a characteristic *kink*. Furthermore, the dispersion is broadened in $\mathbf{k}$ which assigns a lifetime to the electronic state. This pays tribute to the fact that electrons, due to interaction with phonons, show shorter coherence lengths.

It is possible to express the phonon contribution to the dispersion relation in a Hartree-Fock approach with an effective dielectric constant that includes the screening of interacting electrons and phonons [66]. However, here we will focus on the description which is suitable for a many-body implementation in the Green's function method, namely to describe the electrons as quasiparticles with a self-energy Σ. For a thorough introduction to electron-phonon coupling in metals, we refer to the book by Grimvall [159] or other literature [135, 160]. A large field of application for the Migdal-Eliashberg theory is electron-phonon coupling in superconductors. Engelsberg and Schrieffer famously applied the presented approach to the simple phonon spectra in the Einstein and Debye model [161].

The fundamental concept behind the self-energy is to describe a new particle instead of an electron. This particle is a *quasiparticle* which behaves like an electron and includes its interactions. This way, these interactions do not have to be considered throughout the calculations once they are included in the many-body propagator. The difference between an electron and the quasi-electron is described by the self-energy, so that for the quasiparticle's energy E^* holds $E^* = E + \Sigma$. The self-energy Σ is a complex quantity whose real part renormalizes the electron's energy and the inverse of its imaginary part yields the quasiparticle's lifetime.

The single-particle propagator G introduced in Sec. 3.4 reads including the self-energy Σ

$$G(\mathbf{k}, \varepsilon) = \frac{1}{\varepsilon - E(\mathbf{k}) - \Sigma(\mathbf{k}, \varepsilon) + i\eta} \tag{3.51}$$

It can be interpreted as an interaction of the particle with itself and can therefore be written in a series expansion

$$G = G_0 + G_0 \Sigma G_0 + G_0 \Sigma G_0 \Sigma G_0 + ... \tag{3.52}$$

For an electron-like quasiparticle with energy $\varepsilon = \hbar\omega$ the self-energy reads

$$\Sigma(\omega, \mathbf{k}) = i \sum_\gamma \int_{-E_F}^\infty \frac{d\nu}{2\pi} \int d^3\mathbf{k}' \frac{V}{(2\pi)^3} |g(\omega - \nu, \mathbf{k} - \mathbf{k}'; \gamma)|^2 \tag{3.53}$$
$$\times D(\omega - \nu, \mathbf{k} - \mathbf{k}', \gamma) G(\nu, \mathbf{k}')$$

Here, G denotes the electron propagator and D the phonon propagator. Put simply, both represent the probability that an electron state of $(\nu, \mathbf{k}')$ and a phonon $(\omega - \nu, \mathbf{k} - \mathbf{k}', \gamma)$ are available, so that the given electron can interact with the phonon. Hence, the phonon energy and momentum are given by the differences. Moreover, g is the electron-phonon coupling matrix element characterizing how strongly a given electron interacts with a given phonon. Following Migdal's approximation that coupling beyond the first order is small (c.f. Eq. 3.52) [162], in this equation $|g|^2$ is used instead of the product of g and the vertex function Γ that describes these higher order contributions. The integrals are a sum over all possible final states for the scattering of an initial electron with $(\omega, \mathbf{k})$. For this, the sum runs over all energies ν and wave vectors $\mathbf{k}'$ (full k space) with V as real space volume. The sum over γ denotes the phonon branch.

From Eq. 3.53 it becomes apparent that it is useful to define a coupling function for an electron state $\mathbf{k}$ and a phonon of energy ω that already includes the phonon spectrum and the matrix element. The *Eliashberg function* $\alpha^2 F(\omega; \mathbf{k})$ is defined as

$$\alpha^2 F(\omega; \mathbf{k}) = \frac{V}{\hbar(2\pi)^3} \sum_\gamma \int \frac{\mathrm{d}^2 \mathbf{k}'}{v_{\mathbf{k}'}} |g(\mathbf{k}, \mathbf{k}'; \gamma)|^2 \delta(\hbar\omega - \hbar\nu(\mathbf{k} - \mathbf{k}', \gamma)) \qquad (3.54)$$

For an electron on the Fermi surface with momentum $\mathbf{k}$, the Eliashberg function is a sum over the coupling matrix elements of all possible final states $\mathbf{k}'$, weighted by the Fermi velocity $v_{\mathbf{k}'}$. Furthermore, only those final states are selected whose energy $E(\mathbf{k}) + \hbar\omega$ matches with the phonon energy $\hbar\nu(\mathbf{k} - \mathbf{k}')$. The term $\alpha^2 F(\omega)$ originates from the phonon density of states $F(\omega)$ and average electron-phonon interaction $\alpha^2(\omega)$ as introduced by McMillan [163]. Often the k-dependence is neglected, and then the Eliashberg function is calculated as an average over the Fermi surface:

$$\alpha^2 F(\omega) = \int \frac{\mathrm{d}^2 \mathbf{k}}{v_{\mathbf{k}}} \alpha^2 F(\omega; \mathbf{k}) \bigg/ \int \frac{\mathrm{d}^2 \mathbf{k}}{v_{\mathbf{k}}} \qquad (3.55)$$

The Eliashberg function is dimensionless and is independent of the volume of the specimen (in the definition in Eq. 3.54, the volume V cancels against a factor within $|g|^2$). In order to characterize the strength of electron-phonon interaction within a material with a single number, the k-independent Eliashberg function can be averaged over energy to obtain the *electron-phonon coupling parameter* λ:

$$\lambda = 2 \int_0^\infty \frac{\alpha^2 F(\nu)}{\nu} \, \mathrm{d}\nu \qquad (3.56)$$

This quantity is also called *mass enhancement parameter* as it changes the effective mass m^* of the electronic quasiparticles at the Fermi energy by

$$\left(\frac{m^*}{m} \right) = 1 + \lambda \qquad (3.57)$$

Typically, λ is assumed to become relevant for the material's properties when it exceeds a value of 1. For Cu, its bulk value is $\lambda_{\mathrm{Cu}} = 0.15$ and for Pb as strong coupling superconductor $\lambda_{\mathrm{Pb}} = 1.55$ [159]. Substituting $\alpha^2 F(\omega)$ into Eq. 3.53 yields
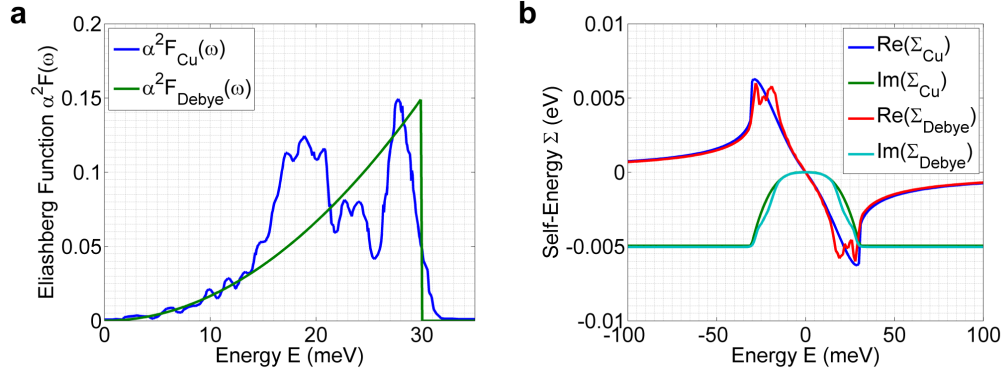
Figure 3.14: Comparison of Cu experimental data and a Debye model with $\lambda = \lambda_{Cu} = 0.15$ and $\omega_D = 30\,\text{mV}$. Eliashberg function for Cu taken from [164]. (a) Eliashberg function $\alpha^2 F(\omega)$ (dimensionless). (b) Self-energy $\Sigma(\omega)$ calculated using Eq. 3.59.

for the self-energy with few approximations at $T = 0$

$$
\Sigma(\omega) = \int_0^\infty d\omega' \alpha^2 F(\omega')
$$
$$
\times \left[\int_{-\infty}^0 \frac{d\nu}{\omega - \nu + \omega' + i\eta\,\text{sgn}(\omega)} + \int_0^\infty \frac{d\nu}{\omega - \nu - \omega' + i\eta\,\text{sgn}(\omega)} \right] \qquad (3.58)
$$

with an integration over all phonon energies ν and possible final states ω'. This integration can be simplified with the complex logarithm and a complex argument:

$$
\Sigma(z = \omega + i\delta) = \int_0^\infty d\omega' \alpha^2 F(\omega') \ln\left(\frac{\omega' - z}{\omega' + z} \right) \qquad (3.59)
$$

To get an impression of the Eliashberg function $\alpha^2 F(\omega)$ and the resulting real and imaginary part of the self-energy, these quantities are plotted in Fig. 3.14. Experimental data of Cu (taken from [164]) is compared with a Debye model whose Eliashberg function reads

$$
\alpha^2 F_D(\omega) = \lambda \cdot \left(\frac{\omega}{\omega_D} \right)^2 \quad \text{for} \quad |\omega| < \omega_D. \qquad (3.60)
$$

Above the Debye frequency, no phonon states are available and $\alpha^2 F_D(\omega) = 0$. This equation holds because a constant coupling is assumed for all phonon modes of the Debye model's phonon density of states $D(\omega) = 3\omega^2/(2\pi^2 c^3)$ with speed of sound c. For Cu, the Debye temperature is $\Theta_D = 343\,\text{K}$ and the corresponding frequencies

$\omega_D = 30\,\mathrm{mV}$ and $\nu_D = 4.49 \times 10^{13}\,\mathrm{Hz}$ [67]. The Eliashberg functions in Fig. 3.14(a) increase towards the Debye frequency and then abruptly cut off for higher energies. The curve of $\alpha^2 F_{\mathrm{Cu}}(\omega)$ shows additional peaks around $E = 18\,\mathrm{meV}$ originating from the real phonon spectrum. According to ab-initio calculations, the Cu Eliashberg function generally follows the phonon density of states without exceptionally large coupling to particular parts of the phonon spectrum [165]. These additional modes prove not to be crucially relevant for the self-energy shown in Fig. 3.14(b). The self-energy's imaginary part is symmetric and the real part anti-symmetric around $0\,\mathrm{eV}$. The imaginary part always has to be negative and its absolute value increases from zero to the cut-off energy from where on it remains constant. The real part shows a maximum peak closely below the cut-off energy and then slowly decreases to zero. Comparing the Debye model with the experimental Cu data demonstrates that the Debye approximation is suitable.

As described in Eq. 3.51, the self-energy is added to the electron dispersion in the denominator of the propagator. Hence, the real part of the self-energy acts as a shift on the electron dispersion $E(\mathbf{k})$. The effect of the imaginary part becomes more obvious in the spectral function:

$$A(\mathbf{k}, \varepsilon) = \frac{1}{\pi} \frac{|\operatorname{Im}\Sigma|}{[\varepsilon - E(\mathbf{k}) - \operatorname{Re}\Sigma]^2 + (\operatorname{Im}\Sigma)^2} \tag{3.61}$$

The imaginary part acts as Lorentzian broadening of the spectral function. While for $\operatorname{Im}\Sigma = 0$ the spectral function $A(\mathbf{k}, \varepsilon)$ is a δ-distribution at every point of the dispersion $E(\mathbf{k})$, a non-trivial imaginary part causes that multiple $\mathbf{k}$ values correspond to one energy.

The role of the self-energy's real and imaginary part are illustrated qualitatively in Fig. 3.15. The shifted energy due to $\operatorname{Re}\Sigma$ causes the characteristic kink in the band structure with respect to the bare electronic dispersion. It is symmetric around the Fermi level. The imaginary part causes a broadening which stays constant for $|E| > \hbar\omega_D$. Towards the Fermi energy the quasi-particle peak narrows down and lifetime increases. Close to E_F, the electrons lack the energy to excite most of the phonon modes and, thus, cannot scatter. In contrast, any electron with $|E| > \hbar\omega_D$ has sufficient energy to excite any phonon mode and therefore the quasiparticle lifetime is constant and shorter.

Many-body effects like electron-phonon interaction lead to the described renormalization of the band structure. The fact that electron focusing depends on the
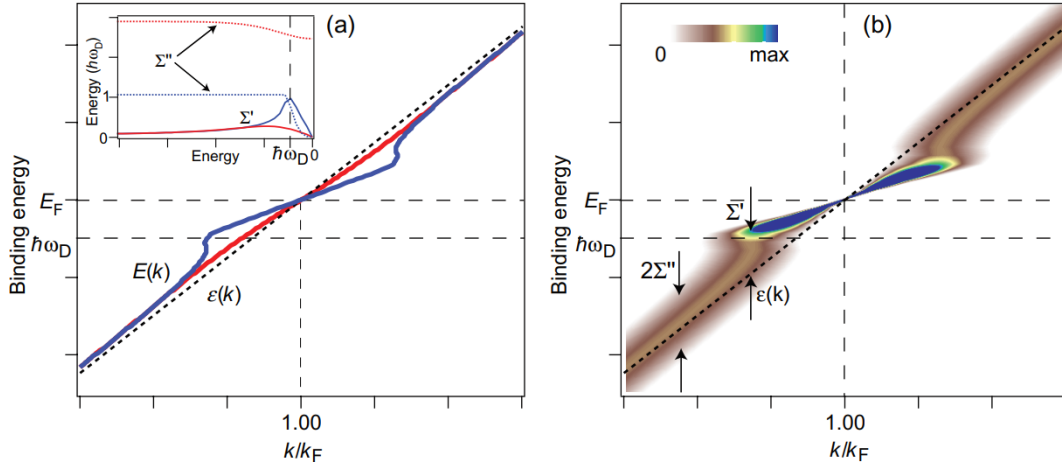
Figure 3.15: (a) Renormalization of the electronic dispersion from bare dispersion $\varepsilon(k)$ for low temperatures (blue) and higher temperature (red). Inset: real and imaginary part Σ' and Σ'' for high and low temperature. (b) Spectral function $A(\omega, k)$ for low temperature. The quasi-particle peak sharpens around E_F as $\mathrm{Im}\,\Sigma$ vanishes. Reprinted with permission from Hofmann et al. [166] (2009), licensed under CC BY-NC-SA 3.0.

anisotropies of the electronic structure suggests that the impact of the self-energy from electron-phonon coupling or other many-body interactions might also be found in a real space signature. In Chap. 6, we will use the plane wave tight-binding model introduced in Sec. 3.5 to simulate spectroscopy data including electron-phonon coupling. We implement this via the real part of the Debye self-energy $\Sigma_D(\omega, \lambda)$ which is added to the dispersion obtained from the tight-binding calculation. From this renormalized isoenergy contour with $\varepsilon = E(\mathbf{k}) + \mathrm{Re}\,\Sigma$ the real space Green's function propagator G is calculated.

3.8.2 Experimental Signatures

The self-energy corrections due electron-phonon coupling lead to a renormalization of the band structure, especially around the Fermi level. Here, we discuss how these modifications can be identified experimentally.

For the bulk, quantum oscillation techniques like de Haas-van Alphen measurements were already used decades ago to quantify the mass enhancement parameter λ [1]. Lee et al. determined the cyclotron masses for different orbits of the Cu Fermi surface, finding a k dependence from $\lambda = 0.085$ up to $\lambda = 0.23$ [167].

Today's most versatile technique to study band structures, especially those of 2D materials, is angle-resolved photoemission spectroscopy. ARPES is based on the
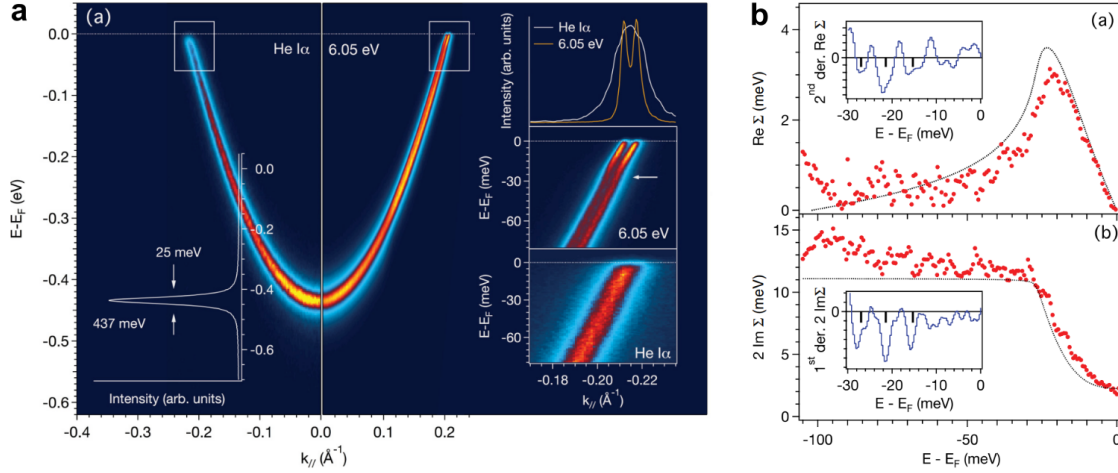
Figure 3.16: Direct extraction of λ and Σ from band renormalization. (a) Conventional He Iα (left) and laser-ARPES (right) data from the Cu(111) surface. Insets show the momentum distribution curves at E_F and zoom-ins to the energy interval near E_F. (b) Self-energy of the surface state compared with Debye model. The insets reveal the fine structure of the Eliashberg function. Reprinted figure with permission from Tamai et al. [171]. Copyright (2013) by the American Physical Society.

photoelectric effect. A photon with sufficient energy extracts an electron from the surface of a material. By detecting the kinetic energies and the emission angles of the photoelectrons, the band structure can be mapped in momentum space. Two different approaches to determine the electron-phonon coupling parameter λ or directly the self-energy Σ are discussed in detail in [166, 168, 169] and are briefly introduced here.

The most immediate way to quantify electron-phonon interaction is to extract it directly from the band renormalization close to the Fermi energy. The measured dispersion is compared to the bare dispersion, which has to be known for this analysis, revealing $\mathrm{Re}\,\Sigma$. The peak width in momentum determines the imaginary part of Σ. This was already performed by Valla and co-workers for the Mo(110) surface state in 1999 [7], who identified the characteristic kink in the spectra. The developments of the technique allowed continuous improvements in energy resolution [169, 170]. Fig. 3.16 shows experimental work of Tamai et al. using conventional ARPES (He Iα) and laser-ARPES ($h\nu = 6.05\,\mathrm{eV}$) on the Cu(111) Shockley surface state, revealing its Rashba splitting [171]. The parabolic dispersion is well-resolved and very close to E_F the kink in the dispersion is found. For resolving it clearly, the higher resolution laser-ARPES data has to be used (inset of Fig. 3.16a). Having extracted $\mathrm{Re}\,\Sigma$ and $\mathrm{Im}\,\Sigma$ from the momentum distribution curves for each energy, the typical shape

of the self-energy is revealed (Fig. 3.16b). Apart from the overall fit to a Debye model with $\lambda = 0.16$, they could also identify oscillations as fine structure within the self-energy. These are linked to the Eliashberg function $\alpha^2 F(\omega)$ which shows coupling to certain phonon modes at the given energies (inset of Fig. 3.16b).

This approach requires high energetic resolution up to the the Fermi energy. At the same time, the measurement near E_F is advantageous, because the parameter λ can vary strongly with energy [166], and thus one obtains the value that is crucial for transport. It is extracted from the experimental data by the gradient of the real part of the self-energy:

$$\lambda = -\frac{\partial \operatorname{Re} \Sigma(\omega)}{\partial \omega}\bigg|_{\hbar\omega = E_F} \tag{3.62}$$

An alternative method, used by McDougall and co-workers as one of the first ARPES experiments to quantify the electron-phonon interaction, gives access to $\operatorname{Im}\Sigma$ and λ via temperature-dependent data [8]. The Lorentzian line shape of energy distribution curves of the Cu(111) surface state is measured for different temperatures. As other contributions to the lifetime are assumed to be either constant (e.g. impurities and defects) or negligible compared to the phonon contribution for the temperature range of $T = 30 - 625\,\mathrm{K}$, a linear dependence for the linewidth of $2\pi\lambda k_B$ is expected. From this, they find for the Γ point of the surface state, located at $E = -440\,\mathrm{mV}$, a value of $\lambda = 0.15$.

Over the years, many surfaces and surface states have been investigated with similar ARPES studies [166, 169]. It was even possible to extract the Eliashberg function $\alpha^2 F(\omega)$ from the spectra without assumptions on a phonon model [9]. At the same time, ARPES also has some disadvantages, such as energy resolution and the restriction to occupied states (or unoccupied in the case of inverse photoemission). Thus, the STM with high spectroscopic resolution for all states around the Fermi level was used as a complementary technique.

First reports on the lifetime of electronic states, including a self-energy, were presented by Li et al. measuring the width of the onset of the surface state in STS data [10]. In 2013, Grothe and co-workers studied the Ag(111) surface state by QPI, revealing its electronic dispersion including kinks due to self-energy corrections [17]. Their results, including a simulation, are shown in Fig. 3.17 that compiles FT-STS data sets of various energies into one image. Around the Fermi level, a symmetric kink is found at $E = \pm 14\,\mathrm{meV}$. Their data reproduces well both real and imaginary
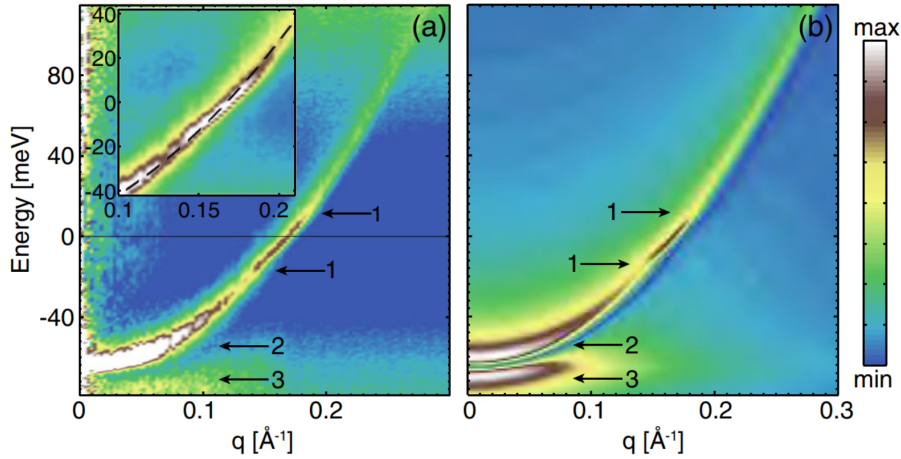
Figure 3.17: (a) Dispersion of Ag(111) surface state obtained from QPI data. Parabolic dispersion is found with subtle kinks at $E = \pm 14\,\text{meV}$, labeled (1) and shown in the zoom-in (inset). (b) Calculated QPI intensity including electron-electron and electron-phonon interaction. Reprinted figure with permission from Grothe et al. [17]. Copyright (2013) by the American Physical Society.

part of the self-energy in a Debye model. With this experiment, they proved the high capability of an STM to characterize electron-phonon coupling in a 2D system. It has to be noted that the low coupling constant of $\lambda = 0.13$ leads to only a small kink in the surface state's dispersion. The consideration in k-space is beneficial to identify the feature because such small deviations in wave length are even harder to resolve.

Other STM experiments followed that also found a renormalization of the quasiparticle band structure due to many-body effects, e.g. for $2H$-NbSe$_2$ [172], in iron-based superconductors [173, 174] or Sr$_2$RuO$_4$[175]. For noble metal (111) surfaces, an additional anomalous energy band was identified to originate from an acoustic surface plasmon [176]. Employing Landau level spectroscopy as a different approach by STM, a renormalized Fermi velocity v_F was attributed to electron phonon-interaction for graphene flakes on graphite [15]. By the same method, Zeljkovic et al. obtained for the surface state of the bulk insulator PbSe a quasiparticle dispersion with a kink due to renormalization from electron-phonon interaction and could extract the real part of the self-energy, a value for λ and the Eliashberg function [16].

Finally, the STM is known to be able to record vibrational spectra, e.g. from single molecules adsorbed on a surface, by inelastic tunneling spectroscopy [28]. The derivative of the differential conductance $\mathrm{d}^2 I / \mathrm{d} V^2$ reveals a peak for each vibrational mode because the tunneling current gains an additional channel. For

collective phonon modes, this was applied, e.g., in graphite [177], noble metal surface phonons [178], and the high-T_c superconductor $Bi_2Sr_2CaCu_2O_{8+\delta}$ [179]. The local Eliashberg function within Pb islands on Cu(111) [13] was measured by probing the spectroscopic properties of the islands' quantum well states. Hence, the phonon spectrum is measured via the coupling to the electrons and therefore it relates to the Eliashberg function. Recently, the phonon spectrum in interaction with the Be(0001) surface state was characterized [14].

In summary, various studies with STM and ARPES have been performed in the past to study the band renormalization due to many-body effects such as electron-phonon coupling. Mainly 2D sample systems were investigated as 3D data is difficult to acquire for STM and difficult to interpret for ARPES. In Chap. 6, we will refer to the remarks given here when we discuss the signature of many-body effects in the three-dimensional system accessed by electron focusing.

4 Dilute Metal Alloys

The previous chapter has introduced the concept of electron focusing and explained how subsurface impurities can be detected at a metal surface and reveal insights about scattering at the impurity as well as the host material. This chapter will cover how the samples required for those measurements are grown and characterized. We investigate germanium and silver as non-magnetic impurities buried in Cu(100).

First, we explain the preparation process of the low temperature growth method. Subsequently, we discuss Cu-Ge surface structures, which can emerge for room temperature preparation. In the second half of the chapter, we review the different residual resistivity of the selected species and the corresponding scattering mechanisms.

4.1 Preparation of Sample Systems

The experimental preparation of the sample systems has to be performed carefully as it has to be made sure that no contaminations – apart from the planned impurity species – are incorporated into the samples. The dilute surface alloys are grown in a home-built UHV chamber ('Probenpräparationsshuttle PPS') with a base pressure of 5×10^{-11} mbar. It is equipped with two electron beam evaporators by Tectra, a sputter gun (Specs IQE11/35), a pyrometer for sample temperature measurement (Impac IM120) and a sample stage with electron beam or resistive heating as well as liquid nitrogen cooling.

In a first step, Cu(100) single crystals are cleaned by cycles of argon sputtering (700 eV, $2.5\,\mu\mathrm{A} \approx 2 \times 10^{-2}\,\mathrm{A/m^2}$) and annealing by electron-beam heating (400 °C). The temperature is monitored with the pyrometer using an estimated emissivity of 11% for the Cu surface [180]. For the final cycles, sputtering and annealing times as well as annealing temperature are reduced (350 °C) in order to minimize segregation of bulk defects to the surface. The last step is an annealing step, so that a flat, large-terrace surface is obtained. The surface quality is checked by low-energy
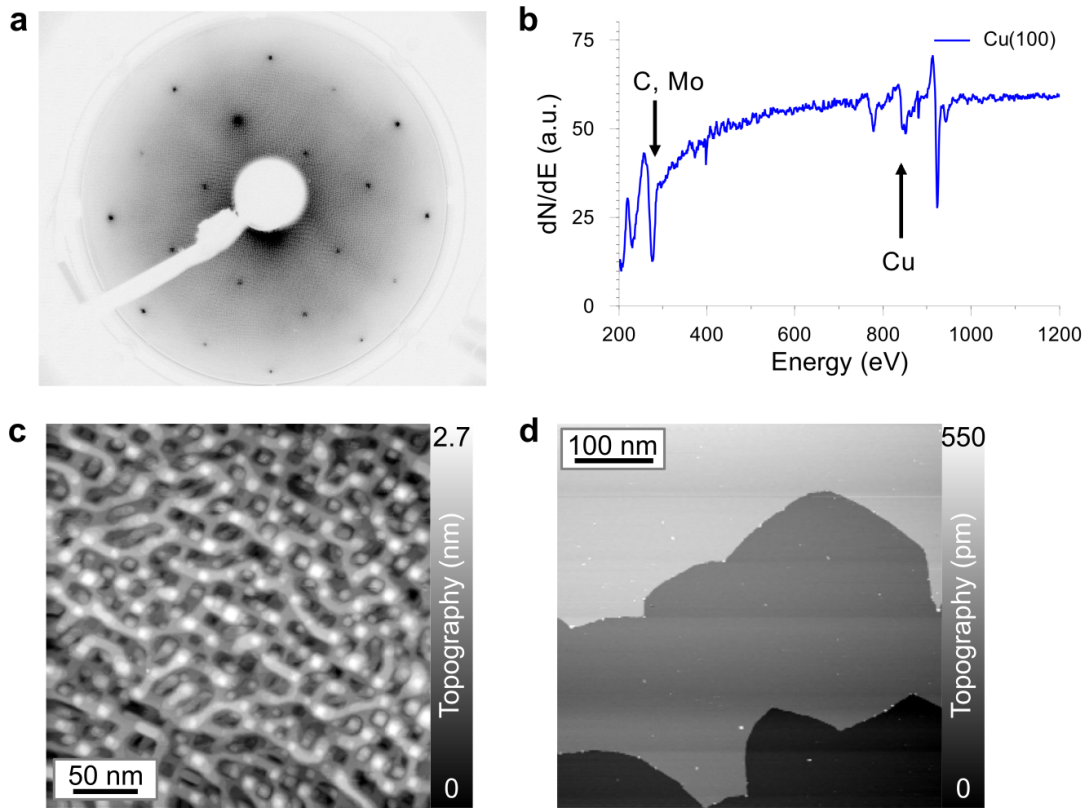
Figure 4.1: Surface analysis of Cu(100). (a) LEED pattern for $E = 283\,\text{eV}$ after seven cycles of sputtering and annealing. (b) AES data for cleaned sample show clear peaks for Cu and remaining signal from the sample holder (C, Mo). (c) STM topography of sputtered sample with rough surface. (d) Annealing produces large flat terraces suitable for investigation by STM (both data sets $U = 1\,\text{V}, I = 0.1\,\text{nA}$).

electron diffraction (LEED) and Auger electron spectroscopy (AES) measurements, where exemplary data is shown in Fig. 4.1(a,b). The diffraction pattern shows sharp peaks with the four-fold symmetry of the (100) surface lattice of the fcc crystal. For AES, the cycles of sputtering and annealing remove peaks from oxygen and reduce signal from carbon and molybdenum (from the sample holder), while the Cu peaks' intensity increases with cleaning cycles. In STM measurements, we find terraces of a size of hundreds of nanometers where surface steps are often pinned at remaining defects, as presented in Fig. 4.1(d). For comparison, an STM topography without the final annealing step, i.e., directly after $5\,\text{min}$ of sputtering, is depicted in Fig. 4.1(c). It shows a rough surface which is significantly structured by the random impact of argon sputter ions.

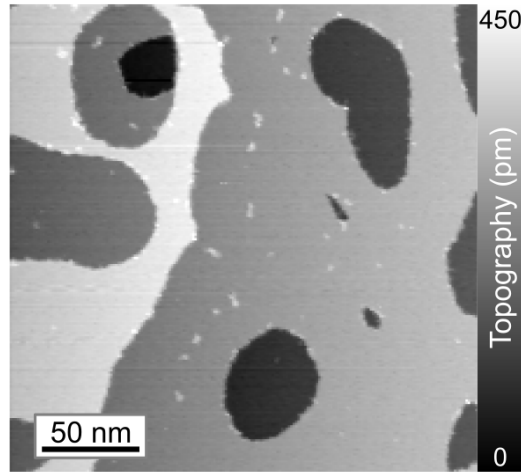Subsequently, dilute surface alloys of 20 monolayers Cu with $< 1\%$ impurities

Figure 4.2: Large-scale topography of dilute surface alloy with Ge in Cu(100), grown at $T = 100\,\mathrm{K}$ with subsequent temperature flash ($240 \times 240\,\mathrm{nm}^2$, $U = 1\,\mathrm{V}, I = 0.1\,\mathrm{nA}$). It is easy to find large-scale terraces or single steps for measurements.

are evaporated by co-deposition onto the cleaned Cu(100) crystals. While Cu is evaporated from a tungsten crucible at a growth rate of $1\,\mathrm{ML/min}$, the impurity evaporator operates at lower rates of $0.1 - 0.3\,\mathrm{ML/min}$ and is equipped with a stepper motor allowing for shutter opening times of down to $100\,\mathrm{ms}$ in order to obtain small ratios of composition. For the evaporation of Ge, a graphite crucible is used. Typical sample structures consist of a clean Cu(100) surface, 15 monolayers of dilute alloy, and a capping layer of three to five monolayers of only Cu. In order to avoid sputtering effects from charged ions of the evaporated material, a high voltage ($U = 1.3\,\mathrm{kV}$) is applied to the sample during evaporation. Furthermore, to limit surface mobility, the sample is held at a temperature of $100\,\mathrm{K}$. Otherwise, impurities have the tendency to separate from the Cu crystal and move to the surface. After low temperature growth, a flat surface has to be restored for investigations by STM. This is why, in a final step, the sample is flashed to $250\,^{\circ}\mathrm{C}$ for $3\,\mathrm{s}$ by electron-beam heating. Then it is immediately transferred into the STM mount which is at $T = 6\,\mathrm{K}$.

An exemplary large-scale topography of the grown surface is shown in Fig. 4.2. For a configuration as depicted in the figure, it is easy to find large flat regions of dozens of nanometers without crystal steps or contamination to investigate the signature of single buried impurities. These surface interference patterns are discussed in detail in Chap. 5.
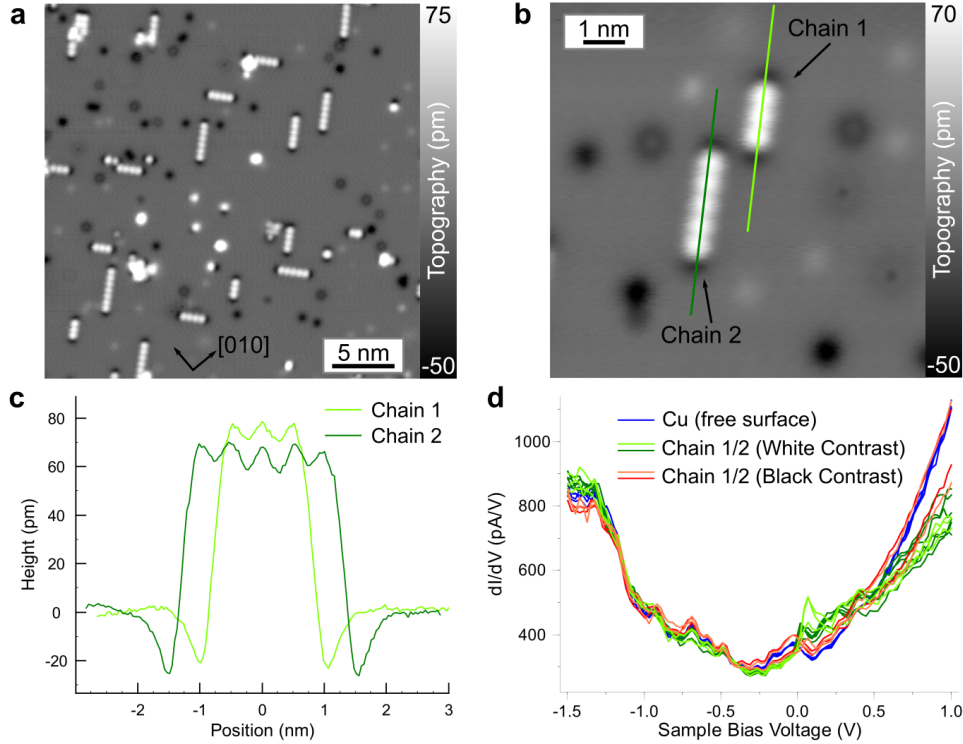
Figure 4.3: Chains on the Cu(100) surface. (a) Overview topography ($30 \times 30\,\mathrm{nm^2}$, $U = 0.1\,\mathrm{V}, I = 0.3\,\mathrm{nA}$) shows Ge chains along the surface lattice. (b) Zoom-in topography ($9 \times 9\,\mathrm{nm^2}, U = 0.2\,\mathrm{V}, I = 1.0\,\mathrm{nA}$) with chains of different lengths and additional surface defects. (c) Height profile for chains labeled in (b) with three and five maxima, respectively. (d) STS on free surface as well as white and black contrast on both chains ($U_{\mathrm{Set}} = -1.5\,\mathrm{V}, I = 0.7\,\mathrm{nA}$).

4.2 Surface Structures

The growth of dilute surface alloys is challenging as every combination of impurity species and host can show different properties, for example for mobility on the surface during or diffusion within the crystal after growth. While a dilute alloy of Co in Cu(100) can be fabricated at room temperature, this approach fails for Fe and low temperature growth at $T \approx 100\,\mathrm{K}$ is necessary [59, 134]. Despite using low temperatures for Ge and three to five cover layers of pure Cu, we still find segregated Ge atoms in the surface layer. For room temperature, the combination of Cu(100) and Ge reveals intriguing surface structures, which we will discuss in this section. Although we are not able to explain the underlying mechanisms, the data shows that for a similar experiment with another species, the respective sample system has to be examined carefully.

When a Cu-Ge dilute alloy is grown at room temperature, the Ge atoms' mobility

on the surface is high, so that they can 'float' on top of the crystal while new layers are added by evaporation. For a low concentration of Ge, approximately 0.1% for twelve bulk layers, we found chains of bright contrast on the Cu(100) surface, as depicted in Fig. 4.3. At each end of the feature, a dark contrast concludes the otherwise bright protrusion. The bright contrast shows a periodicity of $b = 5\,\text{Å}$ and exists in lengths from one bright dot up to chains of seven. Peculiarly, these chains are aligned along the surface lattice, i.e. between the nearest neighbors of the cubic surface lattice ($a_{\text{surf}} = 2.55\,\text{Å}$).

Figure 4.3(b) features two chains of different lengths, surrounded by other surface defects. The three dark depressions show a contrast of $30\,\text{pm}$ which is typical for impurities in the surface layer. The height profiles in Fig. 4.3(c) indicate that the dark contrasts at the end of both chains have a similar depth like a single Ge atom in the surface layer and that the periodicity b resembles for both chains. Its topographic height of $60-70\,\text{pm}$ is assumed to be at least partly of electronic (instead of structural) nature. It remains unclear, if the chains lie on top of the Cu surface with negative electronic contrast, or the impurity atoms are located within the surface layer. As Ge has three more electrons than Cu, this surplus might show as the bright contrast when multiple atoms join such a chain without sufficient screening from the host. As atomic resolution could not be obtained for these structures, the atomic configuration is unknown and the chains' width of $c \approx 6\,\text{Å}$ could either be due to an atomic zig-zag configuration in the surface lattice or due to a far-reaching doping effect from a single line of defects. The periodicity of $b = 5\,\text{Å}$ might be linked to double the distance of the surface lattice a_{surf} or four times the covalent radius of Ge ($r_{\text{cov}} = 1.22\,\text{Å}$). Also alloying structures with mixing components of Cu and Ge, involving the underlying substrate, could be possible. It has to be noted that even for long chains the one-dimensional feature remains energetically favorable (or feasible) compared to a two-dimensional cluster. Spectroscopy on the different parts of the surface mainly shows two features. For high energies, the free Cu surface (blue in Fig. 4.3d) shows higher signal, offering more states to the LDOS than the defect chains (green). These show a peak at $E \approx 100\,\text{mV}$ which appears stronger for the shorter chain.

The result of a different temperature treatment of a Cu-Ge-surface alloy is presented in Fig. 4.4. A sample with 2% of Ge per alloy layer was stored for two weeks at $T = 80\,\text{K}$ before being cooled down to $T = 6\,\text{K}$ again for STM measurements. It cannot be excluded that during the temperature change the sample briefly exceeded
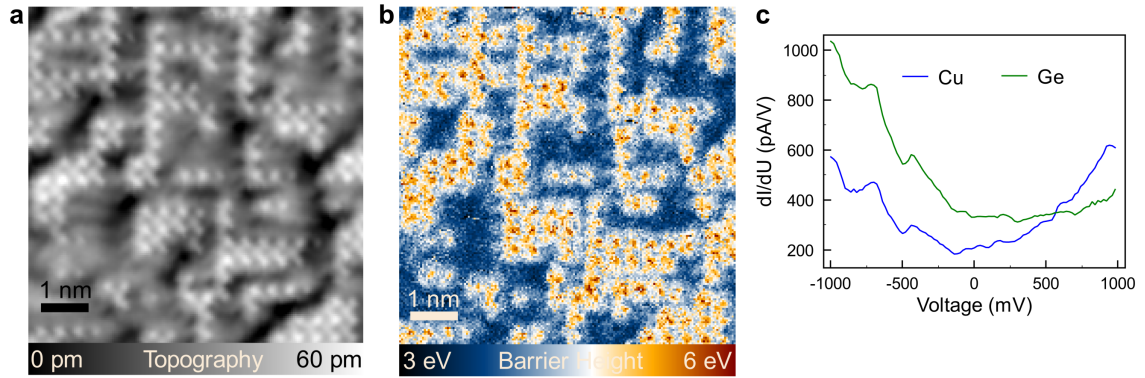
Figure 4.4: Surface structures of Ge in Cu(100). (a) Topography ($7 \times 7\,\mathrm{nm}^2$, $U = 0.05\,\mathrm{V}, I = 0.3\,\mathrm{nA}$) with chains of electronic contrast that align with the surface's crystal structure. (b) Corresponding map of apparent barrier height Φ indicates that Ge networks (high Φ) form in Cu surface. (c) STS data for $U_{\mathrm{Set}} = 1.0\,\mathrm{V}, I = 0.4\,\mathrm{nA}$.

the specified values. On first sight, the resulting surface structures are similar to the patterns presented above with their bright surface contrast. However, here the features are oriented with the crystal directions and not the surface lattice, which means a rotation by 45°. Furthermore, single atoms can be identified to sit on every site of the Cu(100) fcc surface, i.e. 'double chains' that first might seem like two rows of atoms contain a row with weaker contrast in the middle, corresponding to the face-centered atom in the lattice. The apparent barrier height measurement in Fig. 4.4(b) clearly identifies two different chemical species while the unperturbed surface exhibits the typical value of Cu ($\Phi = 3.6\,\mathrm{eV}$). Thus, we assume the atomic contrast is given by a Ge structure that is either fully composed of Ge atoms or an alloy like Cu_3Ge. As the barrier height is rather homogeneous, a mixed structure would be assumed to extend into the first layers of the bulk.

Energy-dependent measurements reveal that the Ge structures show fewer states for high energies (Fig. 4.4c), which matches with the findings for the Ge-like chains that were found for smaller concentrations. The differences in LDOS are sufficiently high to be visible in the multi-bias topographic data in Fig. 4.5. For negative voltage and $U = 0.7\,\mathrm{V}$, similar patterns but with smaller height contrast are found. For $U = 2.0\,\mathrm{V}$, the contrast inverts because the contribution from Cu states of energies higher than $1\,\mathrm{V}$ is so high, that the Ge contribution from close to E_F is excelled.

The investigation of surface alloys was already field of research decades ago [181], and even simple systems like sulfur adatoms on Cu(100) have still been examined
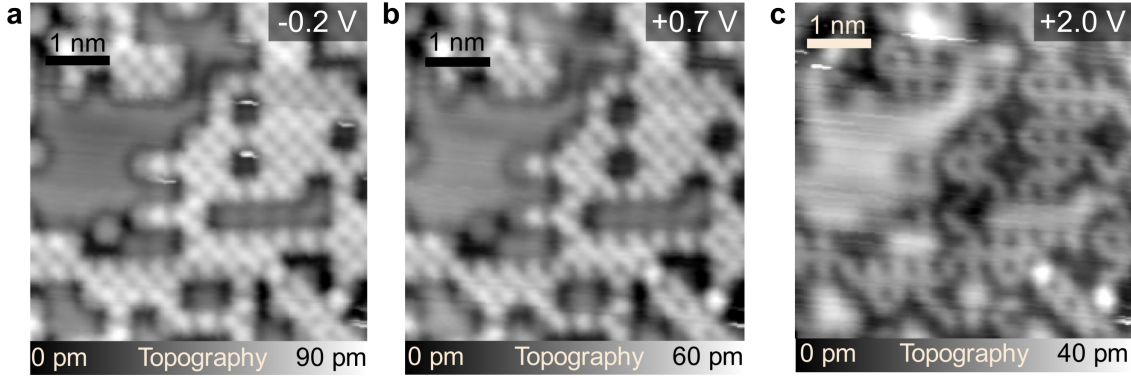
Figure 4.5: Multi-bias topographies of Ge-Cu surface structures ($5.3 \times 5.3\,\mathrm{nm}^2, I = 0.5\,\mathrm{nA}$). Contrast decreases from (a) $U = -0.2\,\mathrm{V}$ to (b) $U = 0.7\,\mathrm{V}$ and inverts at high bias (c) $U = 2.0\,\mathrm{V}$.

recently [182]. We have also found that the preparation of the samples required for our electron focusing experiments is non-trivial and that the interaction of two atomic species during growth and in vicinity of a surface can lead to complex surface structures. On the Cu(100) surface, e.g., adsorbed Pb was characterized for various coverages finding different phases including a $c(4 \times 4)$ superstructure where the Pb atoms form linear chains [183]. For the Fe(100) surface, bulk carbon impurities segregated to the surface and created surface phases with local and long-range order [184]. For this system, one-dimensional surface states were found to emerge due to the electrostatic potential of the adatoms [185, 186]. Such states could also be present in the Ge(-alloy) chains found for the Cu-Ge sample preparation.

Characterizations of surface alloys, including such electronic effects as well as diffusion in the surface layers and mobility during and after growth, are crucial for understanding and designing nanostructures. Especially the interplay of Ge and Cu can be of relevance for metal-semiconductor interfaces, where intermixing and interface alloying can influence structural and electronic properties. Nevertheless, these questions point in very different directions than the primary aim of this work. Therefore, we leave this as a first insight for such surface structures and focus instead on the investigation of subsurface impurities and properties of the bulk. With the low temperature growth, we identified a method that allowed us to fabricate the necessary samples of suitable quality.

4.3 Residual Resistivity

In the electron focusing experiment, we investigate the electrons in a dilute alloy sample system. These charge carriers are mainly responsible for the transport properties of the material and the impurities in the dilute alloy are irregularities that cause additional scattering affecting the transport properties. In this section, we review these effects in terms of macroscopic properties and the residual resistivity. For thorough derivations and more detailed descriptions is referred to the literature [67, 187, 188].

The Sommerfeld model combined the classical Drude model with the quantum mechanical Fermi-Dirac statistics where the electrons obey the Pauli principle [189]. The conductivity of a solid σ is the inverse of the resistivity ρ and describes how it reacts to an external electric field $\mathbf{E}$ with a current density $\mathbf{J}$. According to the model it follows Ohm's law

$$\mathbf{J} = \sigma\mathbf{E} = ne\mu\mathbf{E} = \frac{ne^2\tau}{m}\mathbf{E} = -ne\mathbf{v}_D \tag{4.1}$$

Here, n denotes the electron density, e the elementary charge, m the electron mass, and $\mathbf{v}_D$ the mean drift velocity which is proportional to the applied electric field by the mobility μ. In this description the mean scattering time τ is a central quantity to describe the scattering process as it quantifies the time between two scattering events. It is linked to the Fermi velocity v_F and the mean free path ℓ by

$$\ell = v_F\tau \tag{4.2}$$

Possible scattering events in a solid include scattering at defects, interaction with lattice vibrations (phonons) and interaction with other electrons. Additional scattering processes can be introduced by the sample geometry, i.e. at the sample surface. Each scattering event increases the total resistivity of the sample and reduces the mean scattering time τ. The empirical Matthiessen rule assumes that the scattering rates can be added:

$$\frac{1}{\tau} = \frac{1}{\tau_1} + \frac{1}{\tau_2} + \frac{1}{\tau_3} + ... \tag{4.3}$$

Although the rule is not exact and sometimes rather a rough estimate, e.g. for thin films, it is a helpful tool for predicting resistivities. The different contributions to

the overall resistivity can be added as if the different processes occurred separately:

$$\rho = \rho_1 + \rho_2 + \rho_3 + ... \tag{4.4}$$

While scattering at phonons shows a temperature dependence with $\rho_{\text{ph}} \propto T$ for low temperatures and $\rho_{\text{ph}} \propto T^5$ for high temperatures ($T \gg$ Debye temperature Θ_D), the contribution from defects and impurities is independent of temperature. It is called *residual resistivity* ρ_0. For dilute alloys, this quantity is especially important as the deliberately introduced foreign atoms are mostly responsible for it. Nordheim's rule is a semi-empirical equation that describes the contribution to the resistivity in a metallic alloy due to additional scattering at the substitutional atoms [190, 191]. With X as atomic fraction of solute atoms in a solid solution, the resistivity is given by

$$\rho_N = CX(1 - X) \tag{4.5}$$

Here, the constant C denotes the alloy-specific Nordheim coefficient. Nordheim's contribution to the resistivity can be included in the sum of Matthiessen's rule.

Already in 1932, Linde measured the resistivities of metal alloys in various concentrations [25]. Empirically, Linde's law was found, similar to Norbury's rule [192], that states that the residual resistivity ρ_0 increases quadratically with the valence difference ΔZ between host and impurity atoms:

$$\rho \propto (\Delta Z)^2 \tag{4.6}$$

Some of the results leading to this conclusion are shown in Fig. 4.6, where the atomic increase of resistivity for a Cu host is plotted as function of impurity species, clearly showing the quadratic relation. Although Ag is significantly larger than a Cu host atom, the change in resistivity with respect to a pure Cu sample is close to zero with $\Delta\rho = 0.14 \times 10^6 \, \Omega\text{cm/At\%}$. However, for Ge with a valence difference of three electrons, the resistivity increases by $\Delta\rho = 3.75 \times 10^6 \, \Omega\text{cm/At\%}$ for room temperature. This large difference for both impurity species, with a factor of almost 27, is one of the main reasons to choose specifically these two impurity species for this study. It would be assumed that these macroscopic results can also be found on the microscopic level when investigating single impurity atoms on the atomic scale.
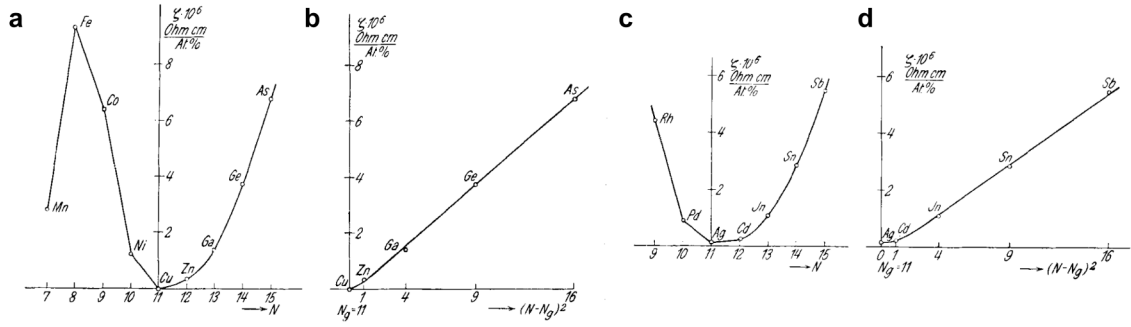
Figure 4.6: Increase in resistivity per atomic percent of impurities for a Cu host ($\xi = (\Delta\rho/c)$ for $c \to 0$). Linde's law is visualized by plotting over the square of valence difference $(N - N_g)^2$ in (b,d). Impurities of (a,b) 4$^{\text{th}}$ period and (c,d) 5$^{\text{th}}$ period. Reprinted with permission from J. O. Linde [25]. Copyright (1932) by Wiley-VCH.

The presented 'laws' were just the starting point for further experimental and theoretical investigations. Of course, some simplifying assumptions break down for more complicated materials, e.g. for alloys of various components, with a specific carrier density or with spin dependence. Most described rules are based on simple quasi-free electron scattering of, e.g., one s-band, so that more sophisticated scattering mechanisms are not represented.

A different approach than the nearly century-old empirical estimates are first-principles calculations that yield insight into the electronic structure of (dilute) alloys, of which the KKR Green's function method described in Sec. 3.7 is only one example. The calculation of impurity scattering and its application in the determination of electronic properties of a metal is a very broad field that is not covered here and, instead, we refer to reviews as [149, 187, 193, 194]. The scattering phase shifts obtained from KKR-DFT calculations describe the atomic potentials of the solid and since these determine the material's electronic properties, various quantities can be derived from them. For example, the phase shifts can be used to parametrize the Fermi surface, as done in connection with de Haas-van Alphen measurements. By applying a quasiclassical approach, combining a quantum-mechanical description of electrons with the classical Boltzmann equation, transport properties can be calculated from first principles. Thus, electronic properties like the resistivity or Seebeck coefficients can be linked to the scattering matrix t. Going even further, the contributions of different states of the Fermi surface to these properties can also be determined, since the ab-initio calculations compose them in a bottom-up approach summing over $\mathbf{k}$.

These connections allow to further investigate the question of the large differences in residual resistivity of Ge and Ag impurities in Cu. For the *sp* impurity Ge, three additional electrons in *s* and *p* orbitals cause a significant additional local valence charge at the impurity [158]. This perturbation of the crystal potential causes high scattering rates especially for *s* and *p* electrons. For the Ag impurity, the electronic configuration on the outer shell is identical to Cu, causing a smaller perturbation than Ge. The residual resistivity of the transition metal Ag in Cu originates from scattering at a 3*d* virtual bound state whose resonance is located far from the Fermi level. Hence, the *d* scattering amplitude at the Fermi level is only small [149, 158]. These explanations match with the values found in the ab-initio calculations presented in Sec. 3.7, where we found strong *sp* scattering for Ge and only weak scattering amplitudes for Ag.

Having discussed the sample preparation and the expected scattering mechanisms in the investigated dilute alloys, in the next chapter, we will present the topographic surface signatures of buried Ge and Ag impurities in Cu(100).

5 Topographic Signatures of Non-Magnetic Subsurface Atoms

In the previous chapter, the preparation of dilute surface alloys and the expected scattering properties of the studied subsurface impurities were introduced. Here, we will present the experimental investigation of topographic signatures of non-magnetic impurities in Cu(100). While single instances of STM data have already been shown above, this chapter takes a systematic approach to characterize the surface interference patterns.

First, the surfaces of dilute alloys are described and we explain how the depth of a specific impurity is determined. Subsequently, the interference patterns are characterized and quantified by a single scattering phase shift in the framework of the tight-binding model and compared to Ag as another non-magnetic impurity species. Finally, we start the transition to energy-dependent investigations with multi-bias measurements.

All presented Ge data was recorded within this thesis. The Ag data was recorded and processed before by H. Prüser whose work is gratefully acknowledged [59]. The analysis of Ag data with the tight-binding model as well as all comparisons with Ge are part of this work.

5.1 Surfaces of Dilute Alloys

The surface of a dilute alloy resolved by STM is shown in a large scale topography in Fig. 5.1(a). It is covered with the strong dark LDOS contrast of surface layer ('1ML') and second monolayer ('2ML') impurities as well as bright spots from adatoms. Between these high-contrast features, there are various interference patterns of different lateral sizes and amplitudes. Each pattern corresponds to a single Ge impurity buried in deeper layers of the Cu(100) surface.

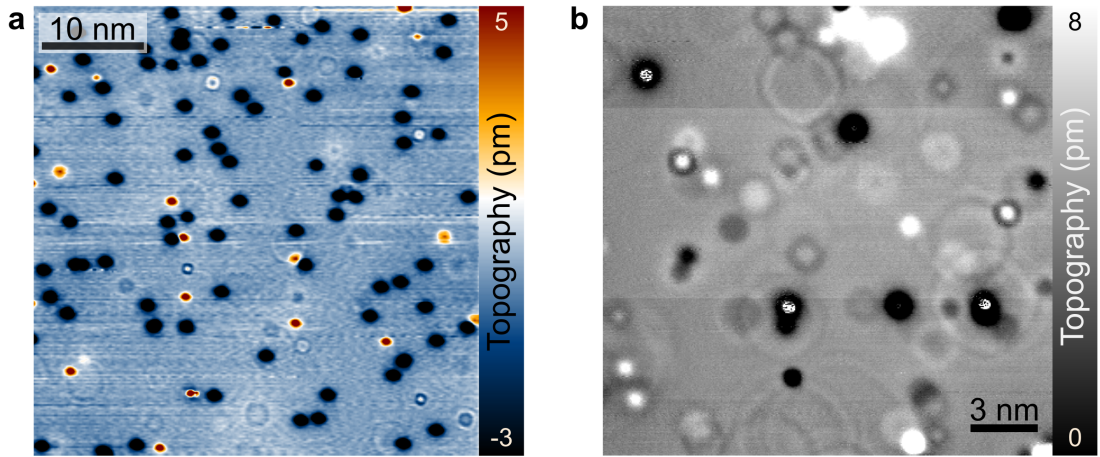Another overview in Fig. 5.1(b) with smaller surface area shows the different

Figure 5.1: Overview topographies of Ge impurities in Cu(100). (a) Topography ($43.5 \times 43.5\,\mathrm{nm}^2$) at set point ($U = 50\,\mathrm{mV}/I = 0.3\,\mathrm{nA}$). (b) Topography ($20 \times 20\,\mathrm{nm}^2$) at set point ($U = -100\,\mathrm{mV}/I = 0.5\,\mathrm{nA}$). Each data set features various four-fold interference patterns, each corresponding to a single buried Ge atom.

contrasts in more detail. Most dominant are ring-like patterns that consist of around 1.5 oscillations of protrusions and depressions in electronic contrast. The topographic height is only a few picometers, which amounts only to a small fraction of an atomic step. The patterns have a four-fold symmetry, which is given by the anisotropic band structure of Cu and the crystal surface orientation. Electron focusing defines, as described in Sec. 3.3, a certain focusing angle for enhanced electron propagation which is around 35° with respect to the Cu(100) surface normal. Hence, a laterally larger pattern corresponds to an impurity buried more deeply in the crystal. Fig. 5.1(b) shows clearly that the interference pattern superimpose without additional interference.

Figure 5.2(a,b) shows a comparison of three separate surface signatures in 2D topography and line sections. A 1ML Ge atom (in the surface layer) shows a negative contrast of approximately 30 pm. This was already found by Kloth et al. for Co atoms in Cu [116]. Only covered by one Cu layer, the 2ML impurity reveals a bright protrusion surrounded by a dark ring with an electronic contrast of around $10-15\,\mathrm{pm}$. These defects are also easily spotted in the overview topography Fig. 5.1(b). For comparison, a 7ML impurity is also depicted in Fig. 5.2. While its signature is spatially more extended than the surface-near defects, the topographic contrast in height is substantially smaller.

We identify the scattering centers as point-like, single Ge atoms. By a precise control of the growth process, we ensure that there is no contamination apart from
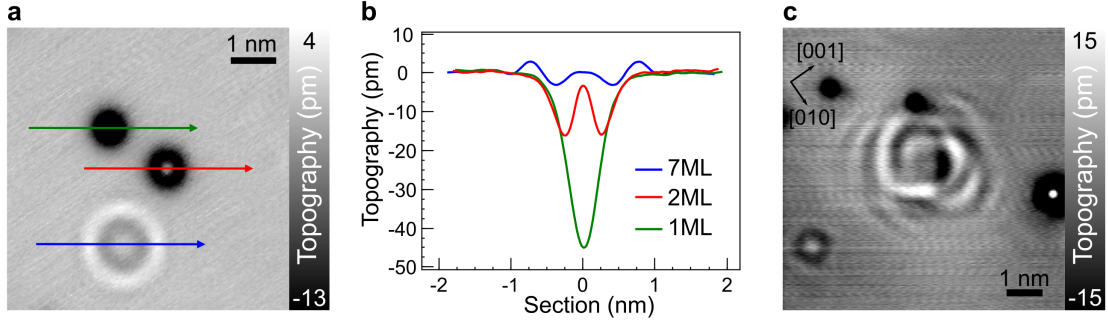
Figure 5.2: Subsurface defects at the Cu(100) surface. (a) $6.1 \times 6.1\,\mathrm{nm}^2$-topography ($U = 100\,\mathrm{mV}/I = 0.4\,\mathrm{nA}$) with dark depressions for surface-near Ge impurities and larger interference pattern for 7ML impurity. (b) Line profiles for different impurities, corresponding to colored arrows in (a). (c) $7.8 \times 7.8\,\mathrm{nm}^2$-topography ($U = -50\,\mathrm{mV}/I = 0.3\,\mathrm{nA}$) showing the complexer pattern of a three-dimensional subsurface cluster.

the impurity species. This is checked by reference measurements with a clean Cu(100) sample and a Cu(100) sample with additional evaporated Cu layers, as shown in Chap. 4. Argon cavities were found by Schmid et al., Kurnosikov et al. and others as result of the single crystal preparation [124, 125, 195]. These show richer interference patterns with larger lateral extent than point-like impurity atoms because of the geometry as three-dimensional subsurface object. Also clusters of impurity atoms cause more complex structures in topography due to multiple scattering centers and focusing angles. However, because the concentration of impurities is usually $< 1\%$, clusters form only rarely. In a few topographies, e.g. in Fig. 5.2(c), we find interference patterns of residual sputter gas or impurity clusters that can easily be distinguished from the clearly defined four-fold surface signatures of single impurity atoms and are therefore excluded in our analysis.

5.2 Determination of Impurity Depth

For the analysis it is crucial to determine the depth of a specific impurity from its surface signature. The key to resolve this question is atomic resolution data. The crystal lattice of Cu(100) consists of equal sublattices parallel to the (100) surface, which only differ by a lateral shift of half a lattice parameter a_{Cu} (depicted in Fig. 5.3(a) in blue and green, respectively). Assuming that the impurity atom sits substitutionally in the Cu matrix, its depth is limited to the Cu monolayers. Furthermore, an impurity's electron focusing pattern is symmetric around the impurity because of the
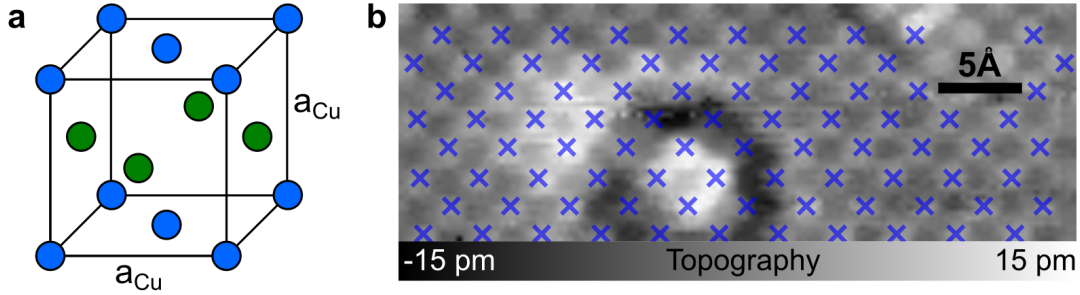
Figure 5.3: Determination of an impurity's depth by atomic resolution data. (a) Cu fcc
crystal unit cell. Atoms of an odd (even) monolayer are colored in blue (green).
(b) Topography of 4ML Ge impurity ($4 \times 1.4\,\mathrm{nm}^2$, $U = -50\,\mathrm{mV}/I = 0.3\,\mathrm{nA}$).
The (partial) surface signature is superimposed with atomic resolution labeled
by blue crosses. The center of the interference pattern is in between surface
atoms, thus, the impurity is located in an even monolayer.

crystal's four-fold symmetry. The position of the interference pattern with respect
to the atomic lattice of the surface determines whether the impurity is located in an
odd monolayer (3ML, 5ML, ...) or *even* monolayer (2ML, 4ML, ...). If the surface
signature is symmetric around a surface atom, then the impurity as scattering center
sits right below this atom, and is part of a monolayer that is identical to the surface
layer, i.e., an odd layer. If the interference pattern is symmetrically located around
a position between surface atoms, then the impurity is located in an even layer. The
signature of an impurity in an even monolayer is shown in Fig. 5.3(b) where the
center of the pattern is clearly between the surface atoms.

In the next step, it needs to be determined in which layer exactly the impurity
atom is located. For this, there are three additional ingredients. Firstly, the overall
lateral size of the interference pattern is approximately given by the focusing angle
that is independent of depth. Generally, a larger interference pattern corresponds to
a more deeply buried atom. However, additional contributions from the phase that
is collected during propagation can change the pattern's shape. Therefore, this is a
helpful guideline, but no irrevocable rule. Secondly, a very experimental approach
is the measurement of many impurity signatures of the same species with similar
imaging conditions. The preparation process does not exclude any layers for the
impurities, thus, data sets for various different layers can be collected and compared.

Finally, the tight-binding model, as introduced in Sec. 3.5, can be used as additional
tool whose application is shown in Fig. 5.4. A data set with atomic resolution depicted
in Fig. 5.4(a) shows an impurity located in an odd layer because the interference
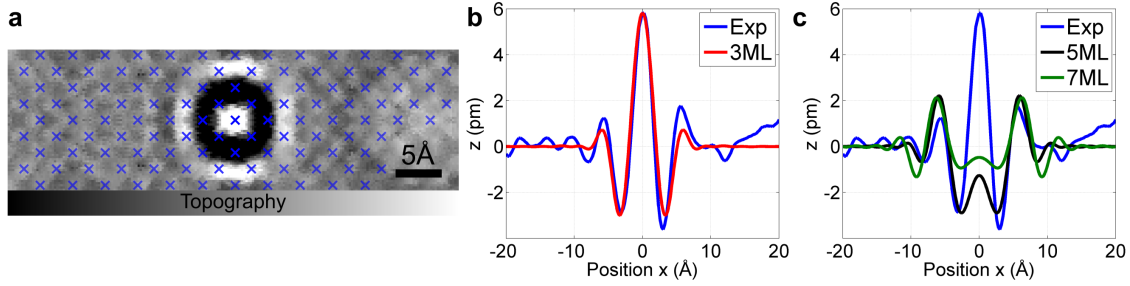pattern is symmetric around a surface atom. The small lateral size of less than

Figure 5.4: Determination of an impurity's depth by atomic resolution data and tight-binding model. (a) Topography ($U = -100\,\mathrm{mV}/I = 0.5\,\mathrm{nA}$) (b) Horizontal section (along [010] direction) in excellent match with 3ML tight-binding calculation. (c) Horizontal section in comparison with 5ML and 7ML simulations, where the main weight of the signal is shifted towards the outer peaks, not matching the experimental pattern. Therefore, the topography in (a) is assigned to 3ML.

2 nm hints towards depths rather close to the surface. In Fig. 5.4(b) and (c) the experimental section is plotted together with tight-binding simulations for different odd MLs, each with a best-fit impurity scattering phase. While for 5ML and 7ML the overall lateral sizes and shapes do not match, for 3ML an excellent fit of experiment and simulation is obtained. Another use case of the tight-binding model is when a complete collection of experimental data for all depths is not available for a comparison, e.g. for very deep layers. Then, if an approximate effective scattering phase is known from other data (see Sec. 5.3 for more details), the calculations can be used to determine the impurity's depth.

5.3 Effective Scattering Phase Shift

We have shown that buried non-magnetic impurities show surface interference patterns even for various layers below the surface. Apart from a certain beauty of the experiment, one has to ask what can be derived from the data. The patterns' shapes are determined by the host's electronic structure and the scattering properties of the impurity. In the tight-binding model presented in Sec. 3.5 the known overall Cu bulk band structure is reproduced accurately and therefore allows to characterize the impurity scattering. It is described in this simple model by an effective scattering amplitude and an effective scattering phase shift η. Here, we fit the experimental data to the tight-binding model in order to obtain the effective scattering phase shift. In the previous section, we have already shown tight-binding simulations that, of

course, include scattering phase values representing the impurity. In this section, we introduce the systematic approach which is used to obtain these suitable values.

In Sec. 3.6, we have characterized the role of electronic orbital characters for the focusing patterns. Yet, for simplicity, we here decide to study the scattering phase shift without orbital resolution as it will be shown that this model can reliably describe the data. In the end of this section, we will discuss the influence of different scattering mechanisms, which also involves the different electronic orbitals.

The absolute scattering amplitude is not fitted with the experimental data. It is responsible for the electronic contrast in height z which also crucially depends on the imaging conditions of tip shape and set point. This is why the relative ΔLDOS differences within a pattern, i.e. the relation of minima and maxima, are taken into account, but not the absolute height. For comparison, the maximum values are matched between experimental and simulated data.

5.3.1 Simulation and Fit

The fit procedure of the tight-binding simulation is based on four parameters (c.f. Fig. 3.5), where the effective scattering phase shift η is the aim of the fit while the other parameters are fixed. It is important to notice that the parameters are coupled, e.g. a small change in a_{surf} leads to a different propagation distance and, thus, collected phase during propagation of the electron wave. In order to obtain the same phase relation at the surface (e.g. maximum constructive interference), this leads to a smaller effective scattering phase shift.

The impurity depth d as integer value is determined as described in the previous section. The height h is fixed for Ge impurities to 7 Å which suits the moderate values for set point currents and bias voltages, while typical STM tunneling distances are 5 Å to 8 Å [43]. The distance between surface layer and vacuum a_{surf} is set to $a_{\mathrm{surf}} = 1.0 a_{[100]}$ in a first approximation which corresponds to a rough estimate where the potential exceeds values occuring within the crystal [146]. Later, the assumptions for h and a_{surf} are checked for their accuracy.

In the fit procedure, the experimental topography section along the [010] direction through an interference pattern of an assigned depth is compared to simulated sections, similarly as in Fig. 5.4. For one data set, all computational parameters are fixed as stated above and simulated sections for all possible phase values $\eta = (0.00...2.00)\pi$ are calculated. The root-mean-square deviation in height is taken as quantity to be optimized, i.e. the deviation concerning every pixel of the fit. The lowest value
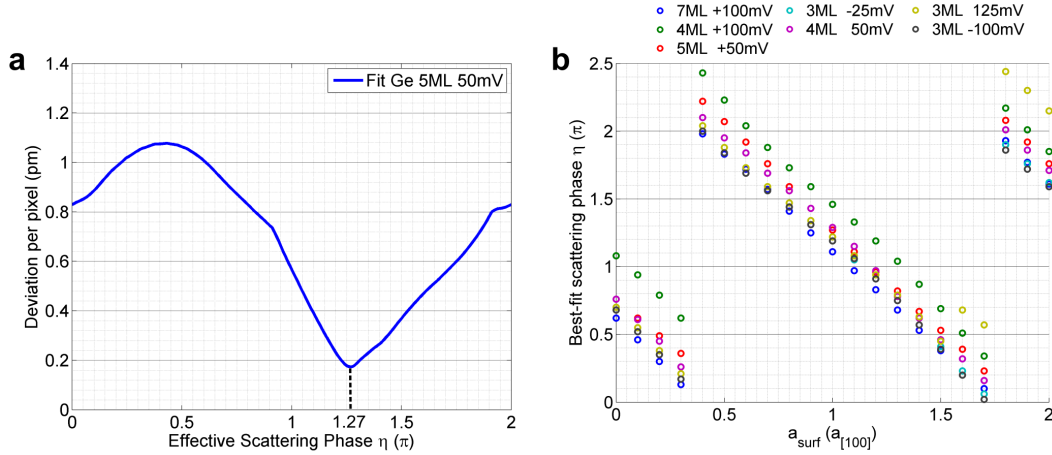
Figure 5.5: Fit procedure for the effective scattering phase shift η. (a) Deviation per pixel for varying phase shift for Ge 5ML impurity with $a_{\mathrm{surf}} = 1.0a_{[100]}$. Best fit is found for $\eta = 1.27\pi$. (b) Determination of a_{surf}. Smallest variance of best-fit phase η for various Ge data sets is found around $a_{\mathrm{surf}} = 1.0a_{[100]}$.

idenfties the best effective scattering phase shift η. This 'brute force' approach in the limited parameter space for the phase allows to easily identify the absolute minimum. On a technical level, in order to be comparable, the simulations are interpolated to the experimental lateral data point distance and the maximum peak amplitudes are matched. We restrict the comparison to the lateral area of the impurity-induced interference pattern. Depending on the depth this is $r < 10\,\text{Å}$ for the small pattern of a 3ML impurity or usually $r < 15\,\text{Å}$ for deeper layers.

An exemplary plot corresponding to the fitting procedure for a Ge 5ML impurity is shown in Fig. 5.5(a). The phase with minimal deviation per pixel corresponds to the best-fit value, here $\eta = 1.27\pi$. The periodicity in the data is expected: the phase η is 'added' to the phase collected during electron propagation. Therefore, a shift of 1.0π leads to an inverted interference condition at the surface.

Multiple checks were performed in order to characterize the stability of the fit with respect to its parameters. The first test deals with the value of a_{surf} where we initially chose $a_{\mathrm{surf}} = 1.0a_{[100]}$. As we assume a depth-independent effective scattering phase shift, we expect the smallest possible spreading of phase values for the best fit. The fit results for various experimental data sets for different values of a_{surf} in Fig. 5.5(b) show that the variance of phase values is smallest around $a_{\mathrm{surf}} = 1.0a_{[100]}$. At the same time, we find that small changes in a_{surf} do not change the outcome significantly. Therefore, our findings do not contradict and are consistent with the findings of A. Weismann who found a best consistency for describing Co

impurities with $a_{\mathrm{surf}} = 1.3a_{[100]}$ [134]. The figure also visualizes the certain ambiguity of the parameters because a smaller value for a_{surf}, and, hence, phase collected with propagation, is compensated by a higher scattering phase η in order to reproduce the same experimental data set.

A similar check can be run for the height h. We find significantly higher variances for the phase values for $h = 3\,\text{Å}$ and $h = 11\,\text{Å}$ which is induced by considerably different pattern shapes due to transmission of more or less frequencies in $k_{\parallel}$, respectively. The most consistent fits are obtained for Ge for $h = 7\,\text{Å}$ and $h = 9\,\text{Å}$ where we choose $h = 7\,\text{Å}$ as it matches better to the literature value distances for the applied set points and a visual comparison of simulated 2D data with the experimental topographies.

It is important to note that the selection of a 1D section is not the only possible way to determine an effective scattering phase from the data. However, it is a suitable approach, as it already leads to neat results. A similar 1D fit for the [011] direction has resulted in very similar phase values and therefore supports the chosen fitting procedure. Nevertheless, the full 2D appearance is also of importance, but more difficult to fit. For example, one would have to discuss imbalances of different topography regions due to the four-fold symmetry of the surface signatures that leads to outward features being more strongly represented in a simple 2D comparison. In the next subsection, it will be shown that the parameters, which are obtained with the presented fit method, prove to describe well the impurities' signatures in both 1D and 2D. The used parameter set is not necessarily unique as different quantities can compensate for another.

5.3.2 Ge Effective Scattering Phase Shift

The tight-binding model is used to describe the impurities' topographic signature. A fit reveals the effective scattering phase shift η which characterizes the pattern shape. Figure 5.6 shows systematically the surface signatures of Ge atoms from 3ML to 7ML. Impurities closer to the surface do not reveal patterns that are determined by electron focusing. The topographic signatures show four-fold symmetry and their lateral size increases with depth from about $1\,\text{nm}$ for 3ML up to a diameter of $2\,\text{nm}$ for 7ML. As a visualization, one can follow the main maximum/minimum being shifted outwards. At 3ML, the highest maximum is the central peak which becomes a broader peak for 4ML, then a small ring in 5ML, and finally in the 7ML pattern a peak which is located at $r = 8\,\text{Å}$. Starting with 7ML, the center area is almost
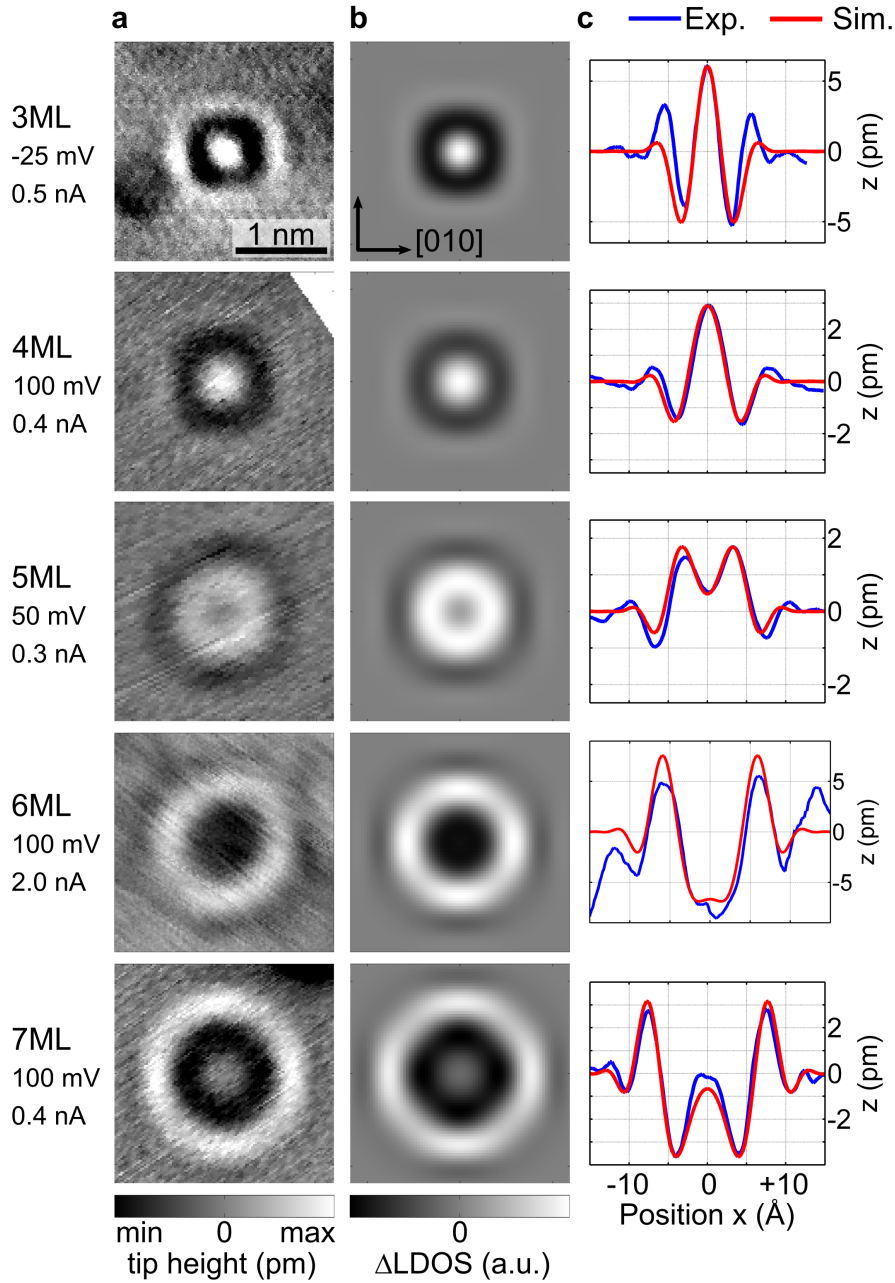
Figure 5.6: Ge impurities in Cu(100) buried in various depths. (a) Experimental topographies ($2.4 \times 2.4\,\text{nm}^2$) show interference patterns of characteristic shape increasing in lateral size with depth. (b) Tight-binding simulations of the topographies with fitted values of $\eta = \{1.19, 1.46, 1.27, 1.07, 1.11\}\pi$ for $h = 7\,\text{Å}$. (c) Comparison of experiment (blue) and simulation (red) along horizontal sections ([010] direction) through the surface signatures shows excellent agreement.

Depth	U_{Bias}	Best Fit η
3ML	$-100\,\text{mV}$	1.19π
3ML	$-25\,\text{mV}$	1.19π
3ML	$125\,\text{mV}$	1.22π
4ML	$50\,\text{mV}$	1.29π
4ML	$100\,\text{mV}$	1.46π
5ML	$50\,\text{mV}$	1.27π
6ML	$100\,\text{mV}$	1.07π
7ML	$100\,\text{mV}$	1.11π
Average		1.23π

Table 5.1: Best fit results for the effective scattering phase shift η for various Ge data sets with tight-binding model parameters $a_{\text{surf}} = 1.0 a_{[100]}$ and $h = 7\,\text{Å}$. Some of the data is shown including the corresponding simulation in Fig. 5.6.

unaffected as the regions with highest maximum/lowest minimum have moved further outwards.

The 2D topography simulations of the tight-binding model in Fig. 5.6(b) match excellently with their experimental counterparts. This is confirmed by the horizontal 1D sections in [010] direction that are shown in subfigure (c). The corresponding phase values are obtained by a fit as described in the previous section.

As we assume an effective scattering phase for Ge that is constant for the investigated energy interval of $-100\,\text{mV} < E < 100\,\text{mV}$ and for all bulk layers, we can average all fit values for η in Tab. 5.1. It includes the data sets shown in Fig. 5.6 and a few more. We obtain as an average effective scattering phase shift for Ge impurities

$$\eta_{\text{Ge}} = (1.23 \pm 0.05)\pi. \tag{5.1}$$

The error is calculated as standard error of the mean. Although the variation of the original data points is larger, all experimental data sets are still well-described by the average value. These variations could be explained by different tip-sample distances in the experiment ('height h'), artifacts due to the summation of multiple energies for set points further away from $U = 0\,\text{mV}$ or experimental resolution. A comparison of this result and the phase shift values from the ab-initio calculations (c.f. Sec. 3.7) will be discussed together with the Ag data (Sec. 5.5) as well as in the next chapter where energy-resolved data is studied.

The average value for the phase shift works well to describe the surface signatures

of buried Ge impurities. On the one hand, this holds for the data sets that were used to obtain the average value, and on the other hand, this holds for data sets where the data quality is not sufficient to extract the phase shift. For example, it can be useful for depth determination of patterns in large overview topographies where no high lateral solution for the specific patterns is obtained. The average phase shift η_{Ge} can be used to forecast a full collection of all possible interference patterns for comparison with depth-unassigned surface signatures.

Analyzing the overview topography presented in Fig. 5.1(a), we find that the tight-binding model in addition to the lateral pattern shape also predicts accurately the topographic contrast in z-direction. We determine the total topographic height, i.e. the difference between maximum and minimum, of 11 interference patterns as well as the corresponding impurity depth in the overview topography. As the resolution does not permit a phase fit, we identify the depth by the average phase value which is not always unambiguous and leads to error bars along the depth axis. The data is shown in Fig. 5.7 with the simulated topographic heights within the tight-binding model.

As the model does not contain an absolute scale in z-direction, the curve is scaled with a constant factor to match the value at $d = 5\,ML$. The experimental and simulated curves match very well for depths in medium range $(5-10\,ML)$ down to very deeply buried impurities more than 15ML below the surface. For comparison, the corresponding signal in an isotropic 3D electron gas $(\propto r^{-2}$, matched to the experiment for $d = 5\,ML)$ decays significantly faster than the experimental and tight-binding data.

For impurities close to the surface, i.e. 3ML and 4ML, the interference patterns are very sensitive to phase changes because the propagation distance is very short and the maximum peak is in the center of the pattern. This is why the tight-binding values do not continue to increase monotonously (and, related to this smaller robustness, also create problems when running a phase fit). Nevertheless, we find that the tight-binding model does not only comprise the physics for the interference pattern shape, but also for the signal losses in the propagation of electron focusing.

In Sec. 3.6, we have introduced orbital components to the tight-binding model. Up to now in this chapter, we have not distinguished between orbitals. This is equivalent to orbital-independent scattering phase shifts and scattering amplitudes where an incoming electron can be scattered into any outgoing orbital component. We have run checks, if a different modeling of the scattering process describes better the
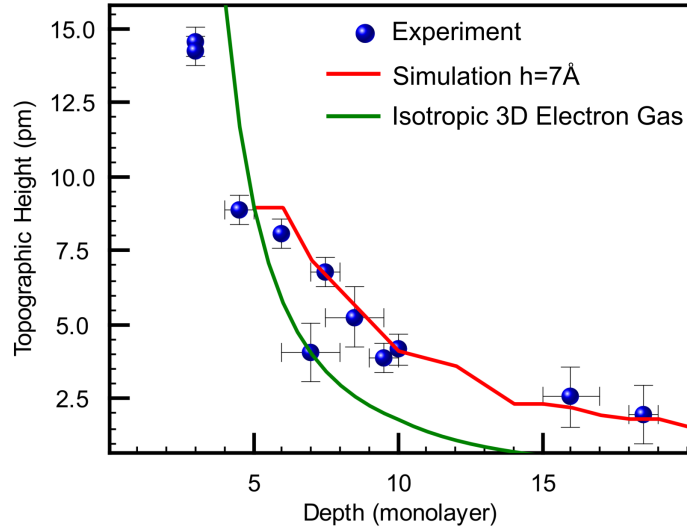
Figure 5.7: Comparison of depth-dependent topographic heights for experiment and tight-binding simulation. The height is defined as difference between minimum and maximum point of the interference pattern. All experimental data points are taken from the overview topography shown in Fig. 5.1(a). Simulated data is not shown for $d < 5\,\mathrm{ML}$ because for short propagation distances the model is very sensitive to the phase shift and depends more on the depth-dependent pattern shape than on the depth. For deeper layers, the experiment is reproduced well in height contrast. In comparison, the signal corresponding to isotropic propagation ($\propto r^{-2}$) decays significantly faster (scaled to experimental data for $d{=}5\,\mathrm{ML}$).

experimental data in terms of the pattern shape. Three candidates were investigated: orbital-independent scattering between all orbitals ('type 1'), scattering only within the orbital character s, p, or d ('type 2'), as well as scattering only within each of the nine orbitals ('type 3'). For each simulation the same effective scattering phase shift and scattering amplitude is used.

In a quantitative fit, the different types of scattering do not show significant differences, neither in the obtained phase values, its variance for different data sets nor the deviation per pixel. It has to be noted that these are average quantities, i.e. the same value can be obtained while one part of the pattern is fitted better and another part matches worse. For scattering within the orbital ('type 3'), the calculated patterns show stronger peak amplitudes at outward positions, while 'type 1' has more lateral weight in the center. Generally, when observing the pattern for 3ML or 5ML in Fig. 5.6, more outward amplitude can reproduce better the experimental data. However, as this is not significantly reflected in the quantitative fit, where we obtained similar values, we chose to use scattering between all orbitals ('type 1') as the simplest version for the analysis and the plots in this thesis.

There are several reasons why the orbital-resolved analysis does not yield a clear result for one scattering mechanism. Firstly, as mentioned above, the simulations are overdetermined with parameters where maybe not the best combination was found matching the real system. Furthermore, the fit quantity 'deviation per pixel' might not be suitable in the orbital analysis as it only takes into account the 1D section and does not weight different areas of the scattering pattern. Finally, the orbital-dependent analysis is not conclusive. For example, orbital-dependent scattering amplitudes might shed light into the scattering mechanism. In order to make use of further parameters introduced into the model, more statistics by more data sets of the same depth and species would be necessary.

By determining the effective scattering phase shift η, we are able to characterize Ge impurities and their surface signatures from depths close to the surface down to more than a dozen layers into the crystal. In the next section, we will have a closer look at deeply buried impurities.

5.4 Deeply Buried Impurities

Non-magnetic impurities show interference patterns for surface-near depths, as discussed in the previous sections, and even for deeply buried Ge atoms. The latter show signatures of a few nanometers in diameter, as, e.g., found in Fig. 5.1. The tight-binding model is needed to identify the depth of these impurities because there are several reasons that make it hard to determine the layer without the numerical model. Firstly, we do not have a complete data set available with interference patterns for all depths with comparable measurement conditions (set point, tip shape) as not every layer is found during measurements. Furthermore, deeper scattering centers cause weaker signals in the LDOS (e.g. 1 pm instead of a few pm), so that the signal-to-noise ratio decreases. Also, atomic resolution is a helpful tool to identify an even or odd layer, but obtaining atomic resolution simultaneously with such a weak focusing pattern is very challenging and was not successful for the data presented here. Finally, as the center area is unperturbed for large interference patterns, the overall pattern shape resembles more for deeper layers. In Fig. 5.8, this can be seen in a full collection of tight-binding simulations at the Fermi energy for impurity
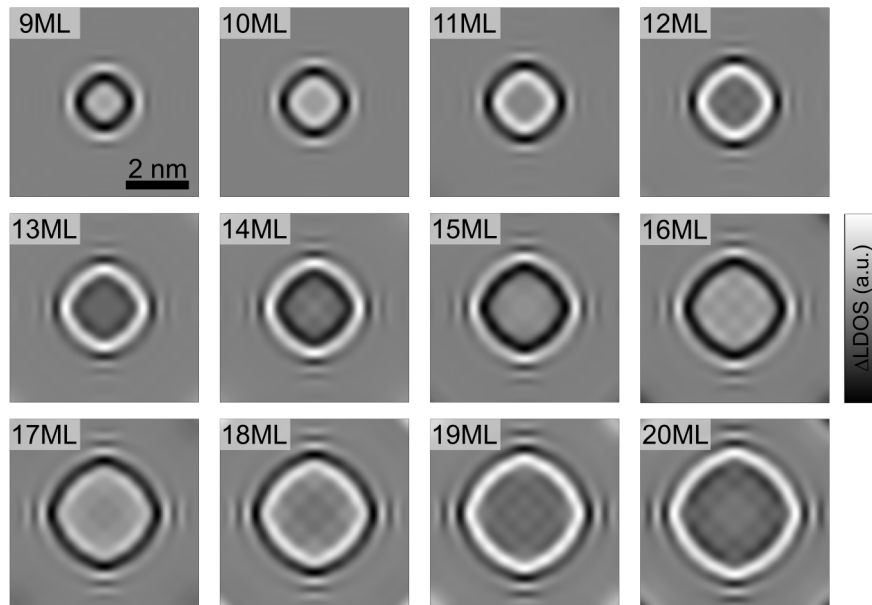

Figure 5.8: Calculated topographic surface signatures (6×6 nm^2) at $U = 0$ mV for Ge impurities ($\eta = 1.23\pi$, $h = 7$ Å) in deep layers. The surface signatures for neighboring depths only differ by small differences in lateral size and ratio of intensity of maxima and minima. The range of the color scale decreases by a factor of four from 9ML to 20ML.

depths of $9 - 20$ ML. These patterns' shapes and lateral sizes can be compared to experimental data.

An example of such an overview with deeply buried impurities is depicted in Fig. 5.9. From the comparison with 2D and 1D tight-binding simulations, we suggest as depths for the distinctly visible patterns 14ML (top right), 13ML (top left) and 13ML (bottom left). As the data of 1D sections is often noisy, a possible approach to determine the depth is to first obtain a depth range from the lateral size of the pattern and in a second step compare the shapes with the possible candidates. This strategy succeeds if the apparent effective scattering phase shift is close to the mean value calculated above, so that the pattern coincides with the shapes in Fig. 5.8.
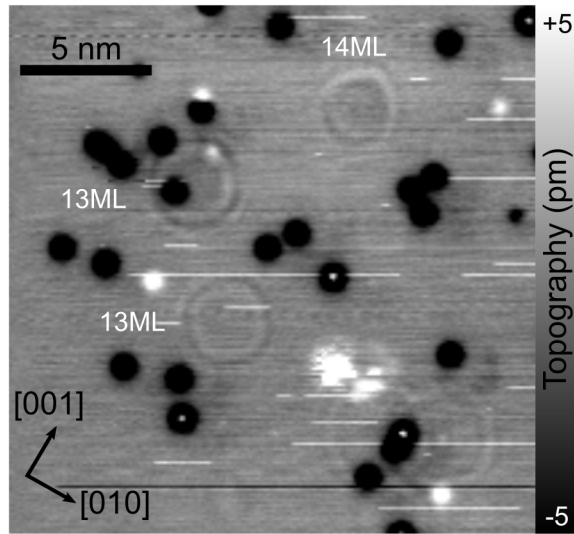

Figure 5.9: Overview topography (20×20 nm^2, $U = -100$ mV$/I = 0.5$ nA) with the signatures of three deeply buried impurities. Black contrast are 1ML and 2ML impurities.

In Fig. 5.10 we show three different patterns in layers deeper than 10ML that were recorded with higher resolution. Peculiar in comparison with the signatures of impurities closer to the surface, shown in Fig. 5.6, is an apparent rotation of the patterns by 45°. This starts for 7ML and can be clearly identified for deeper impurities, also found in Fig. 5.8. This seeming change in shape can be explained by the focusing directions. For Cu(100), the main features are the fourfold beam-like signatures along the crystal directions (c.f. Fig. 3.7b). These beams are connected to form the typical ring shape. For small patterns, this results in nearly quadratic patterns aligned with the crystal lattice. For larger depths, the beams are oriented into the same directions, but as the main minima and maxima are further apart, the
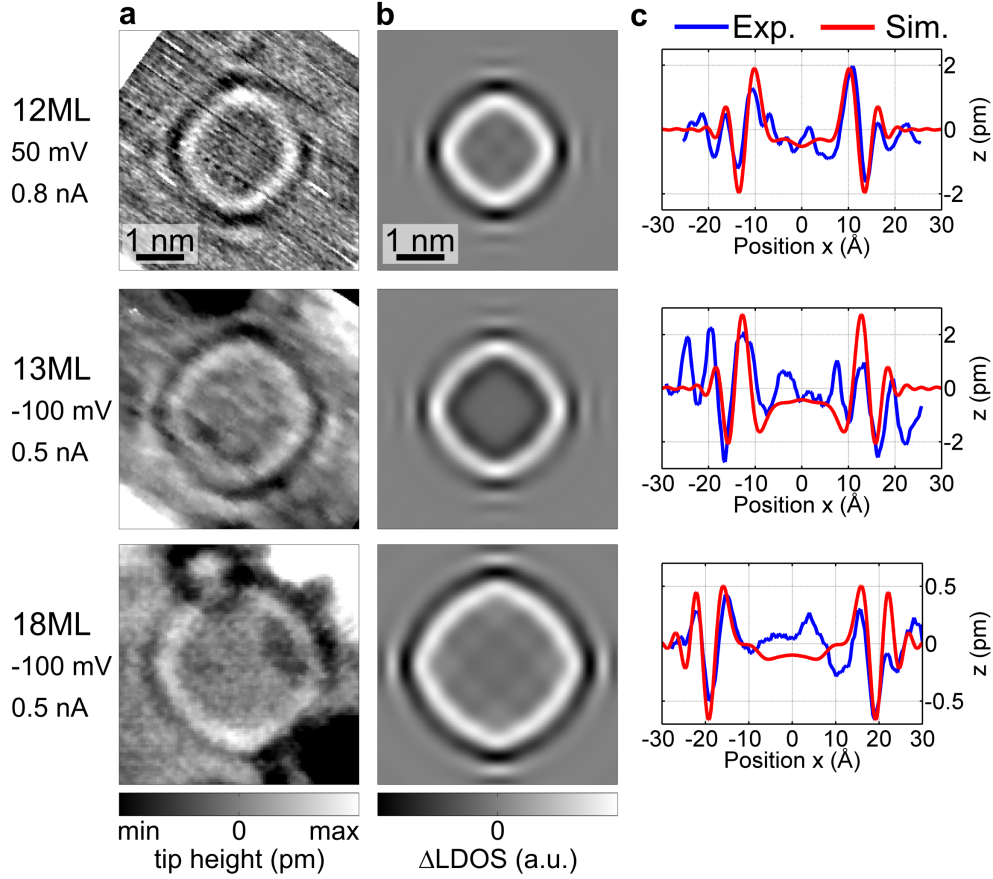
Figure 5.10: Surface signatures ($5.0 \times 5.0\,\text{nm}^2$) of three Ge impurities buried more than 10 monolayers in Cu(100). Although the pattern shape is similar, different depths show different pattern sizes. The (a) experimental topographies match well to (b) tight-binding simulations ($\eta = 1.23\pi, h = 7\,\text{Å}$), as shown in (c) the comparison of sections along the [010] direction.

rings appear rotated against the crystal lattice.

All experimental topographies in Fig. 5.10 show a height contrast of around 1 pm, so that data acquisition is challenging. For the 13ML pattern, the 1D section data alone would be difficult to interpret, and the 2D image is necessary for distinguishing between peaks from the interference pattern and from noise or background signals. In the experimental topography, on first sight 12ML and 13ML appear similar with a combination of maximum/minimum/maximum. However, in the 2D tight-binding simulation it becomes clear that both signatures show that the ring of dark contrast is more pronounced for 12ML. Furthermore, especially the 1D section shows that the peak positions are different as the pattern for 13ML is significantly larger. Due to considerations like this, we can assign the impurities' depths with some certainty.

All in all, despite the low electronic contrast of deeply buried impurities, we can identify their interference patterns at the surface, even for a single subsurface atom located a few nanometers below the surface.

5.5 Comparison with Ag Impurities

In the previous sections, we have characterized Ge impurities buried in Cu(100). In order to distinguish between general properties of non-magnetic impurities and the specific characteristics of Ge, we compare the results found so far with Ag impurities. Silver is also a non-magnetic species, however, it is isoelectronic to Cu and therefore significantly different from Ge.

The surface signatures of Ag impurities, shown in Fig. 5.11, appear to be very similar to the patterns found for Ge. From 3ML to 7ML the patterns' sizes increase with depth and also the pattern shapes are surprisingly identical when compared to the Ge patterns (c.f. Fig. 5.6). For the 7ML pattern, the focusing pattern is superimposed with atomic resolution. Other than that, the tight-binding model can, similarly to Ge, describe the Ag interference patterns both in 2D topographies and 1D topographic sections.

We fit an effective scattering phase shift η_{Ag} to the data, as explained for the Ge analysis in Sec. 5.3. Here, we also use $a_{\text{surf}} = 1.0a_{[100]}$ and choose $h = 5\,\text{Å}$ due to the different set point for the Ag data. We obtain the phase values presented in Tab. 5.2 and find that the values scatter less which can be explained by the set point at $U = -10\,\text{mV}$ which excludes effects from the summation of different energies.

We find an average value of $\eta_{\text{Ag}} = (1.32 \pm 0.05)\pi$. This is similar to η_{Ge} and

Depth	U_{Bias}	Best Fit η
3ML	$-10\,\text{mV}$	1.34π
4ML	$-10\,\text{mV}$	1.39π
5ML	$-10\,\text{mV}$	1.42π
6ML	$-10\,\text{mV}$	1.24π
7ML	$-10\,\text{mV}$	1.29π
7ML	$-150\,\text{mV}$	1.23π
Average		1.32π

Table 5.2: Best fit results for the effective scattering phase shift η for various Ag data sets with tight-binding model parameters $a_{\text{surf}} = 1.0a_{[100]}$ and $h = 5\,\text{Å}$. Most of the data is shown including the corresponding simulation in Fig. 5.11.
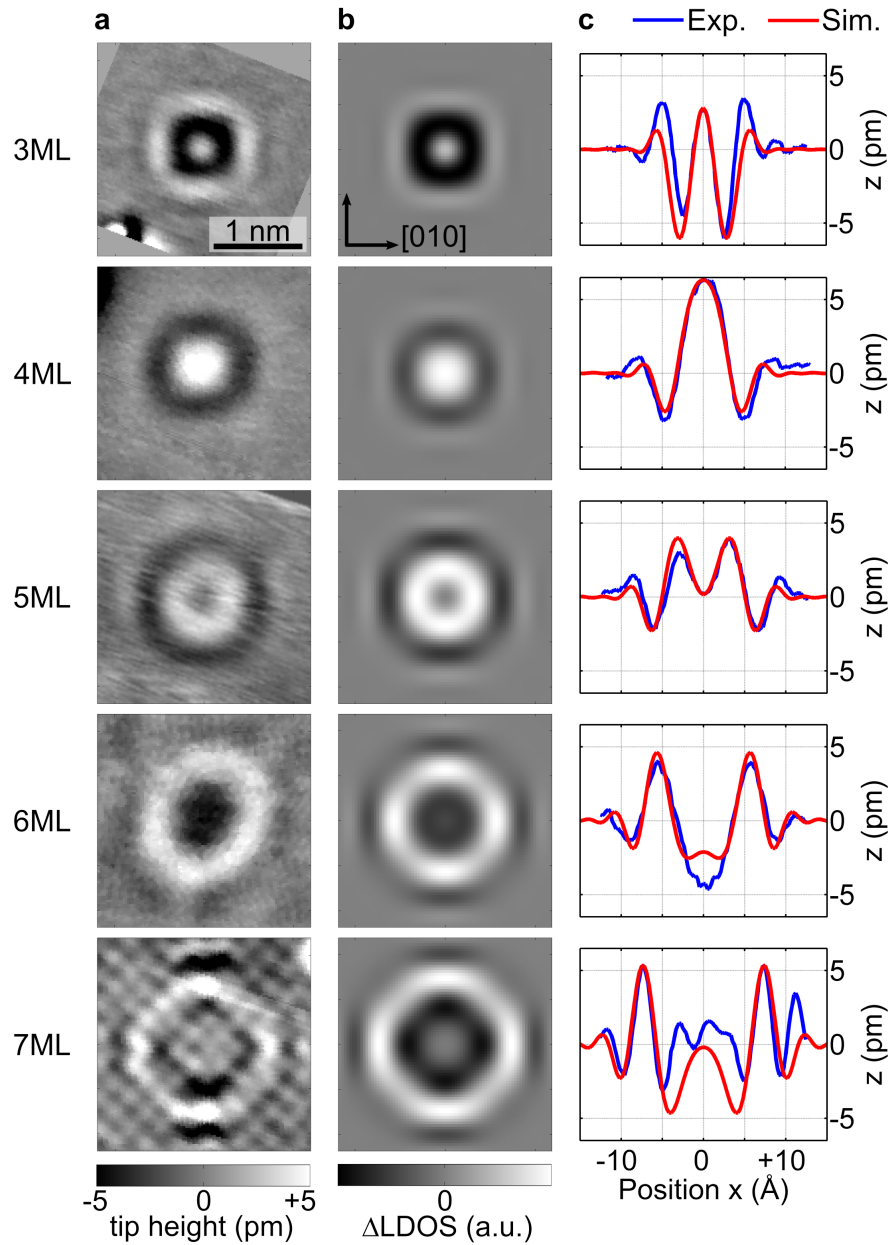
Figure 5.11: Ag impurities in Cu(100) buried in various depths. (a) Experimental to-pographies ($2.4 \times 2.4 \, \text{nm}^2$) at set point ($U = -10 \, \text{mV}$ / $I(3\text{L},7\text{L}) = 2.0 \, \text{nA}$, $I(4\text{L},5\text{L}) = 3.0 \, \text{nA}$, $I(6\text{L}) = 0.8 \, \text{nA}$) show interference patterns of characteristic shape increasing in lateral size with depth. For 7ML, atomic resolution is superimposed with the electron focusing signal. (b) Tight-binding simulations of the topographies with fitted values of $\eta = (1.24\pi...1.42\pi)$ for $h = 5 \, \text{Å}$. (c) Comparison of experimental (blue) and simulated (red) section along horizontal sections ([010] direction) through the surface signatures.

quantifies the resembling appearance of Ge and Ag patterns. Interestingly, they also resemble the surface signatures of the magnetic impurity Co [23, 134]. At the Fermi level, we have obtained a value of $\eta_{\mathrm{Co}} = 1.48\pi$ for $(h = 5\,\text{Å}, a_{\mathrm{surf}} = 1.0a_{[100]})$. However, as the impurity introduces an additional phase shift due to the Kondo resonance, the effective scattering phase is expected to change on a scale of few hundreds of mV for Co.

For a comparison of the tight-binding effective scattering phase shift values with the scattering phase shifts in the ab-initio DFT calculations, the role of the orbital contributions has to be regarded. In η all orbitals are combined, while in the first-principles calculations different values for s, p and d are given for δ and the corresponding $\arg(\Delta T)$. Due to the correspondence of propagation distance and phase shift via the tight-binding parameter a_{surf} a comparison of the absolute numerical values is not possible. Instead, we can compare the difference between both species within each framework.

With the tight-binding fit, we obtain a similar value for the scattering phase shift. In the DFT results, as described in Sec. 3.7, the scattering phase shift δ and the corresponding $\arg(\Delta T)$ is significantly different for s and p states while the values for the d orbital are for both species in a similar range. This is a cautious indication that the experimental topographic patterns are dominated by d orbitals. We will discuss the comparison of experimental and DFT results in more detail in the next chapter, where we also consider ab-initio STS simulations that include the scattering amplitude of the different orbital channels.

5.6 Energy-Dependent Topographies

Up to now, we have analyzed topographies close to the Fermi level. In the next chapter, we present STS data and the energy-dependence of the impurities' surface signatures. Here, we discuss constant current topographies at different energies. For this, it is important to note that the topographies are a sum over the signatures of different energies, which are weighted differently by energy-dependent transmission in the STM tunneling process. This mix of signals with highest sensitivity at the set point voltage can blur features, e.g. when a peak position shifts with energy.

In order to exclude possible effects from tip modifications, we recorded multi-bias topographies for a 7ML Ge impurity, as shown in Fig. 5.12. As all data is recorded within one data set with changing voltages in every line, we ensure the same tip shape

for all topographies. As also the set point current is increasing from $U = \pm 300\,\mathrm{mV}$ to $U = \pm 100\,\mathrm{mV}$, this leads to a reduced tip-surface distance. Approximating a constant LDOS in the given energy range, in simple tunneling theory one would expect a tip movement of $\Delta h = 0.27\,\text{Å}$ for the change in current and $\Delta h = 0.53\,\text{Å}$ for the change in energy. This estimation matches very well with the experimental tip height difference of $\Delta h = 0.78\,\text{Å}$ found for both $\pm 100\,\mathrm{mV}$ with respect to the absolute height at $U = -300\,\mathrm{mV}$.
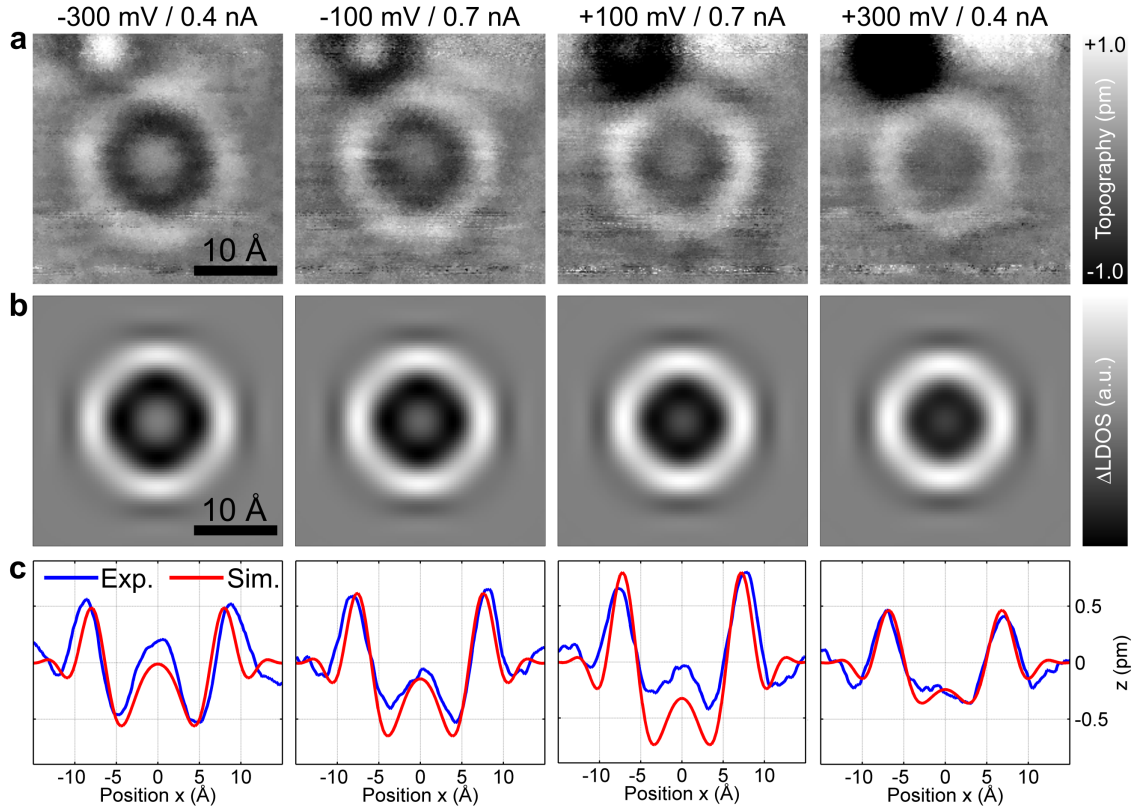

Figure 5.12: Multi-bias topographies of a Ge 7ML impurity $(3.0 \times 3.0\,\mathrm{nm}^2)$ for $(U = \pm 300\,\mathrm{mV}/I = 0.4\,\mathrm{nA})$ and $(U = \pm 100\,\mathrm{mV}/I = 0.7\,\mathrm{nA})$. (a) Experimental topographies. (b) Tight-binding simulations. $(\eta = 1.25\pi, h = 7\,\text{Å})$ (c) Comparison of lateral sections of experiment (blue) and simulation (red) along [010] direction. For higher energies, the pattern shrinks as the features move towards the center. The simulation reproduces well the topographic change with energy.

The 2D experimental topographies in Fig. 5.12(a) show an apparent shrinking of the ring-like patterns. The features like the bright maximum or dark minimum move towards the center and disappear there. This is illustrated by the light peak in the center that vanishes between $-300\,\mathrm{mV}$ and $300\,\mathrm{mV}$. The described changes are also

visible in the tight-binding simulations in 2D and are confirmed in the 1D section where experiment and simulation are compared. The contrast in z for $100\,\text{mV}$ is larger than for $300\,\text{mV}$, which can be explained by the set point; this finding is less pronounced for negative bias voltages. In general, this data was recorded at the limit of z resolution, so some steps in noise reduction and image post-processing were necessary. Nevertheless, the energy-dependent effects can be clearly identified.

The explanation for the 'shrinking' is given by how electron focusing works. The surface interference patterns are determined by the phase relation of incoming and scattered electrons, protrusions (depressions) occur at sites of constructive (destructive) interference. The phase relation changes for different electron wave lengths which depends on energy: the dispersion of the host's band structure connects higher energy with a higher momentum k and, hence, a smaller wave length λ. This results in the same phase condition being satisfied for shorter propagation distances, i.e. closer to the pattern's center. Thus, the host's electron dispersion in visualized in the interference patterns shown in these constant current topographies.

The next chapter is dedicated to the energy-dependence of interference patterns and what can be learned from it about both the impurities and the electronic structure of the host material.

6 Spectroscopic Signatures of Non-Magnetic Subsurface Atoms

In the previous chapter, we have shown that we can detect signatures of single buried non-magnetic atoms in STM topographies of the Cu(100) surface. We understand how the interference patterns are a result of electron focusing and how their shapes are given by the host band structure as well as the scattering properties of the impurity, which we can describe in a simple model with a single effective scattering phase shift. In this chapter, we characterize the energy-dependence of the surface signatures by means of scanning tunneling spectroscopy (STS).

Weismann et al. have used topographies at the Fermi level to 'see the Fermi surface in real space' [20]. Thereafter, Prüser et al. have thoroughly investigated the energy-dependence of the signature of magnetic atoms by STS, characterizing the Kondo properties of the impurity as a single-atom Kondo system [22–24, 59, 134]. Here, we investigate the interference patterns of non-magnetic impurities. Firstly, these yield access to the energy-dependent scattering properties of the impurity. Secondly, as both investigated species act as weak scatterers, we expect their signatures to be rather featureless in the considered energy interval around the Fermi level. In a comparison of Ag and Ge, this allows to disentangle the different contributions of impurity and host. We can functionalize a non-magnetic impurity atom in order to obtain a real space access to the local bulk band structure of the host.

First, we will introduce the STS signatures of Ge impurities in Cu(100) and compare them to experimental data of Ag impurities as well as to tight-binding simulations. Subsequently, we analyze the corresponding ab-initio calculations and discuss the scattering properties of different electronic orbital contributions. In Sec. 6.4, we present low-bias features found in the experimental data around the Fermi level that we identify as band renormalizations due to many-body effects. We extract and discuss an electron-phonon coupling parameter λ that can describe the data. The chapter is concluded with an outlook.
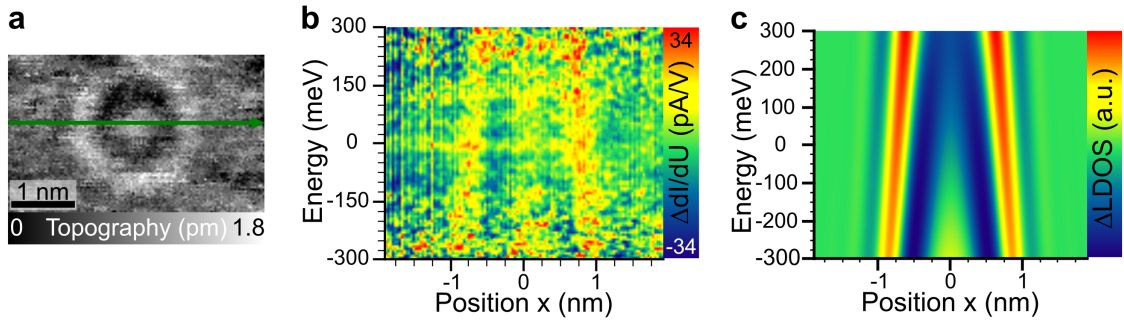
Figure 6.1: Signature of Ge 7ML impurity. (a) Topography obtained during STS measurement ($U = -300\,\mathrm{mV}/I = 0.3\,\mathrm{nA}$). (b) Spectroscopic section in [010] direction (indicated by the green line in panel a). The difference $\Delta\,\mathrm{d}I/\,\mathrm{d}U$ with respect to the pristine Cu surface is color-coded. (c) Tight-binding simulation, reproducing the major characteristics of the interference pattern with peak positions and dispersion with energy ($\eta = 1.25\pi$, $h = 7\,\mathrm{\AA}$).

6.1 Ge STS Surface Signatures

The spectroscopy data are studied in sections along the crystal axes that coincide with the four-fold symmetry of the interference patterns. Such a simplification is necessary for a graphical representation printed on paper because STS is recorded in four dimensions, i.e. $\mathrm{d}I/\,\mathrm{d}U(x, y, E)$. Thus, throughout this chapter, sections along the horizontal [010] direction are the most important depiction of spectroscopic data.

As an example, we show in Fig. 6.1 the spectroscopic signature of the Ge 7ML impurity that was already presented in Fig. 5.12. The horizontal axis of the spectroscopic section in Fig. 6.1(b) indicates the lateral position along the horizontal line in (a), while the vertical axis indicates the energy scale. The color-code depicts the difference in differential conductance $\Delta\,\mathrm{d}I/\,\mathrm{d}U$ with respect to the pristine Cu(100) surface, as introduced in Sec. 2.3, and is a measure for the change in LDOS due to the presence of the impurity. Due to difficult imaging conditions, the signal-to-noise ratio for this data set is rather low. The topography only shows a height contrast of less than 1 pm and as the STS signature requires multiple hours of imaging, it is even more difficult to obtain. Yet, after image processing including topography normalization (c.f. Sec. 2.3.4), clear characteristics can be identified.

The dominant feature in the STS data is the outer maximum that is located at $x = \pm 9\,\mathrm{\AA}$ for $U = -300\,\mathrm{mV}$ and weaker, but clearly visible, is another protrusion in the center. This pattern shape corresponds to the ring-like signature of the topography. The main characteristic with energy is an inward movement of all positions of maxima and minima towards the center. This is explained by energy

dispersion of the focusing electrons, which was already illustrated by the 'shrinking' of the surface signatures in the multi-bias topographies in Sec. 5.6. A higher electron energy is equivalent to a larger wave vector and a shorter electron wave length. Hence, the same interference condition is already fulfilled at a shorter distance. In the center, the features vanish for higher energies what is indicated by the central feature that is especially strong for lower energies and becomes weaker for bias voltages higher than $-100\,\mathrm{mV}$. Generally, the ΔLDOS is strongest at the highest energies. That is because the tunneling matrix element is larger for higher energies, so that the $\mathrm{d}I/\mathrm{d}U$ signal increases.

A tight-binding calculation of the interference pattern in Fig. 6.1(c) reproduces the characteristics of the experimental STS data on the whole. Dispersion is also the dominating effect in the simulation. For this energy interval, it manifests itself in a nearly linear course of the features' positions with increasing energy. In detail, the ratio of the intensities of maxima and minima might somewhat vary between calculation and experiment, especially for the central peak, but even with the average effective scattering phase shift η_{Ge} the general pattern shape is obtained. We find that the tight-binding model can describe well both the topographic as well as the spectroscopic data.

The surface signature of a 5ML Ge impurity, shown in Fig. 6.2, exhibits similar features. The spectroscopic pattern reflects the topography data and is characterized by maxima and minima converging with energy due to electron dispersion. The minimum in the center vanishes for higher energies as the maximum moves towards the center. Again, the tight-binding simulation can reproduce the general shape of the spectrum. Most relevant are the maxima and the outer minimum, both shrinking in lateral size with energy. This is also visualized in the topography-normalized $\Delta\,\mathrm{d}I/\mathrm{d}U$ maps in Fig. 6.2(d) that show the ΔLDOS in both lateral dimensions (x, y) for different energies. Despite the mediocre signal-to-noise ratio both the four-fold symmetry and changes in lateral size due to electron dispersion can be identified.

An additional spectroscopic feature in Fig. 6.2(c) is found at the Fermi level. There is a kink around $0\,\mathrm{eV}$, so that the pattern shifts towards the center as if it is experiencing a small phase shift and back. The overall dispersion in a larger energy interval is unaffected by this zero-bias feature. This characteristic is not observed in the tight-binding data. Thus, the description of the additional kink is beyond the scope of the single-particle band structure calculation. We will discuss this in detail in Sec. 6.4 later in this chapter.
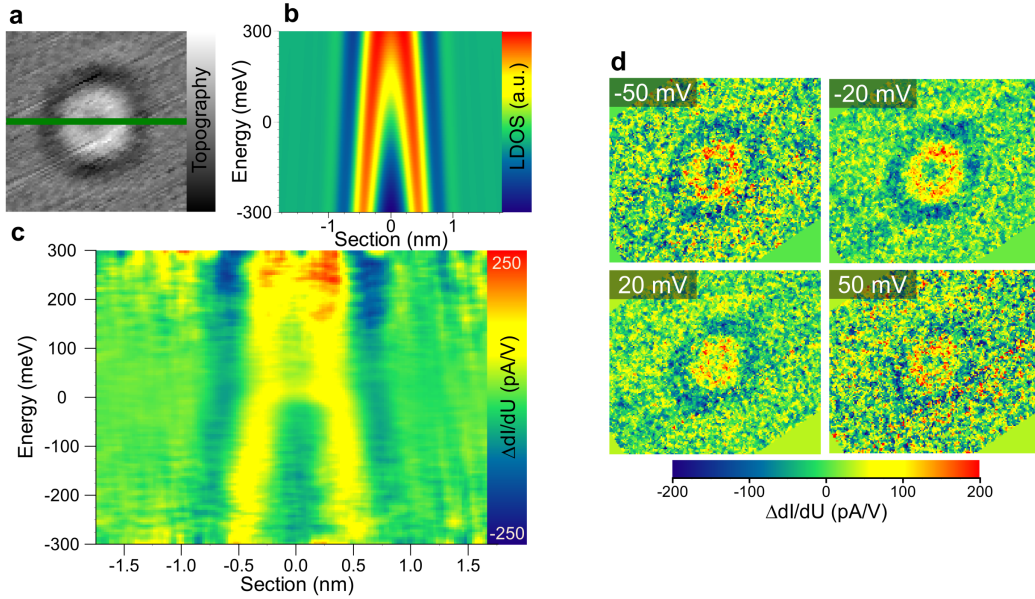
Figure 6.2: Signature of Ge 5ML impurity. (a) Topography ($2.6 \times 2.6\,\text{nm}^2, U = -50\,\text{mV}/I = 0.3\,\text{nA}$). (b) Tight-binding simulation of spectroscopic section ($\eta = 1.25\pi, h = 7\,\text{Å}$). (c) Experimental spectroscopic section ($U_{\text{set}} = -300\,\text{mV}$). The pattern resembles the simulation and shows an additional bending around the Fermi level. (d) Two-dimensional $\Delta\,\text{d}I/\,\text{d}U(x,y)$ maps for energies $E = \{\pm 50, \pm 20\}\,\text{meV}$ show shrinking of ring-size due to dispersion.

Having studied an energy interval of $\pm 300\,\text{mV}$ so far, in Fig. 6.3, we investigate the signature of a 4ML Ge impurity in a larger energy range. The spectroscopic section in Fig. 6.3(c) agrees with the results we have found up to now. The peak in the center and its neighboring minima are also discovered in the topography and show dispersion in the spectroscopy. Again, the additional kink at the Fermi level is not reproduced in the – otherwise matching – tight-binding simulation in Fig. 6.3(d). The large energy interval of $\pm 1\,\text{eV}$ in Fig. 6.3(e) differs from the previous spectroscopic sections as the dispersion deviates from an almost-linear behavior. Furthermore, as the tunneling transmission probability is strongly non-linear in this energy range, the signal around $0\,\text{eV}$ is only weakly imaged. Nevertheless, the found pattern matches to the other experimental data and overall to its tight-binding simulation in Fig. 6.3(f). It is fair to mention that for this layer, the electron focusing interference patterns have a structure similar to surface defects of other species, so that they might be confused. However, as the topographic signals match very well for the calculation and the spectroscopic signal shows the characteristics of the bulk dispersion, we are confident to have identified a 4ML impurity. The measurement in the larger energy
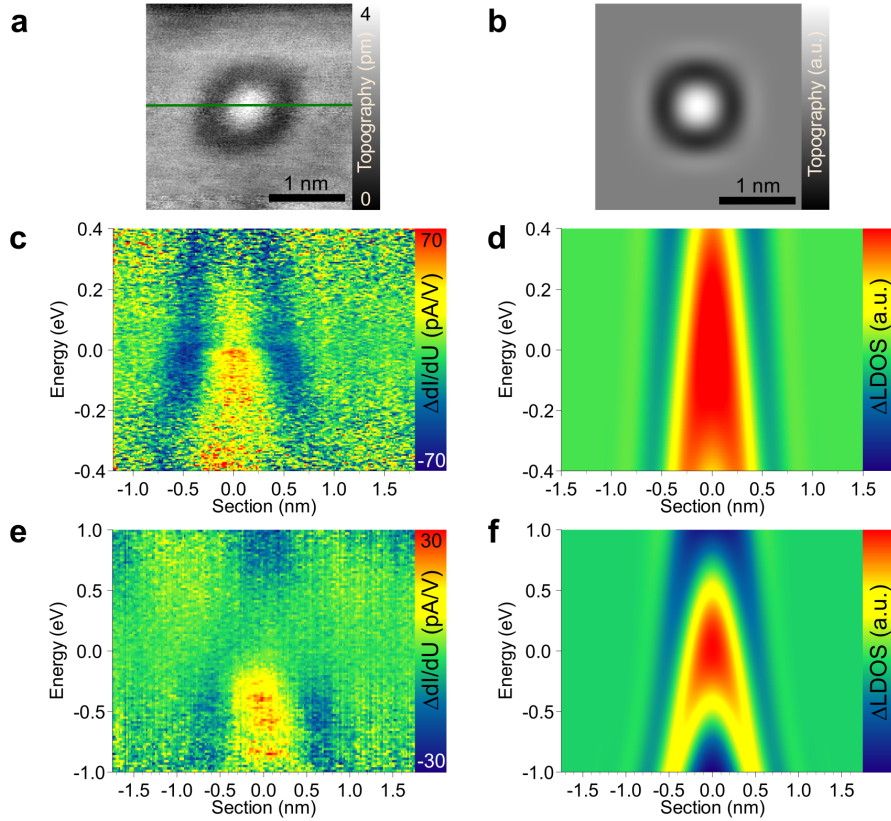
Figure 6.3: Signature of Ge 4ML impurity. (a) Topography $(2.7 \times 2.7\,\mathrm{nm}^2, U = 100\,\mathrm{mV}/I = 0.5\,\mathrm{nA})$ (b) Topography tight-binding simulation $(\eta = 1.23\pi, h = 7\,\text{Å})$ (c,e) Experimental spectroscopic sections for set point $U_{\mathrm{Set}} = -0.4\,\mathrm{V}$ and $U_{\mathrm{Set}} = -1.0\,\mathrm{V}$, respectively. For both ranges, the dominant feature is dispersion. Around the Fermi level, an additional bending is observed in the otherwise approximately linear pattern. (d,f) Tight-binding simulations $(\eta = 1.23\pi, h = 7\,\text{Å})$ are generally consistent with the experimental STS data in (c) and (e), respectively. The feature around zero bias is not reproduced.

interval does not show any further features, such as resonances at element-specific energies. When crossing an energy level of a resonance, e.g. a coupling of an impurity state to the host, a phase shift would be expected in the scattered electrons, but this is not found in the experimental spectra.

We can obtain spectroscopic data even for deeply buried impurities, as for the 18ML Ge impurity shown in Fig. 6.4, which is buried approximately 3 nm below the surface. Although the topographic signature is superimposed with adsorbates and other impurities, it can be clearly identified and resembles the tight-binding simulation. The spectroscopic section in Fig. 6.4(c) shows electronic dispersion that causes the ring-like features to move inwards with higher energy. Because the topography
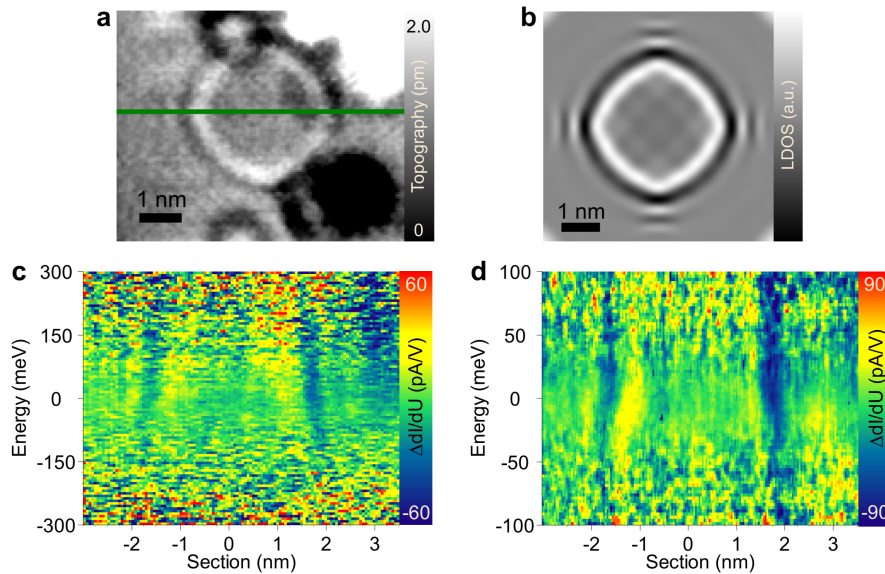
Figure 6.4: Signature of deeply buried 18ML Ge impurity. (a) Topography ($7.0 \times 5.9\,\text{nm}^2, U = -100\,\text{mV}/I = 0.5\,\text{nA}$. Four-fold ring-like feature consists of two maxima and one minimum. (b) Tight-binding topography simulation ($6.0 \times 6.0\,\text{nm}^2, \eta = 1.25\pi$) in excellent agreement with (a). (c) Spectroscopic section ($U_{\text{Set}} = -300\,\text{mV}$) without topography normalization. Ring-like structure moves inwards with energy due to dispersion. (d) Spectroscopic section similar to (c) with smaller energy range showing a bending of the pattern at the Fermi level.

recorded during STS did not allow for a topography normalization, the fading of the signal for negative voltages originates from the set point at $U = -300\,\text{mV}$. We conclude that we obtain an interference pattern from coherent propagation through the Cu single crystal even for a distance of 7 nm from the surface to the impurity and back. The additional spectrum with higher energy resolution in Fig. 6.4(d) reveals the characteristic bending of the interference pattern at the Fermi level, as already found for the other surface signatures.

The signal of ΔLDOS shown in the spectroscopic data is only about 1% of the full spectra $\mathrm{d}I/\mathrm{d}U$. Therefore, the quality of the tip plays a crucial role for the measurements, which is discussed in Appendix A.

6.2 Ag STS Surface Signatures

Since the topographies have shown very similar surface signatures for Ge and Ag, it is straightforward to compare the STS data for both species. The 7ML Ag

impurity depicted in Fig. 6.5 shows a dispersive interference pattern which matches the pattern shape of the topography. The tight-binding simulation fits the overall shape of maxima and neighboring minima. At the Fermi level, we find again an additional kink that bends the otherwise almost linear dispersion. In an energy range of approximately $\pm 100\,$mV the signal becomes weaker and seems to get blurred. This is due to a spectral characteristic of this tip which reduces the total amplitude of the differential conductance for low bias voltages while the signal-to-noise ratio remains alike (c.f. zoom-in in Fig. 6.10 that clearly shows the interference pattern).
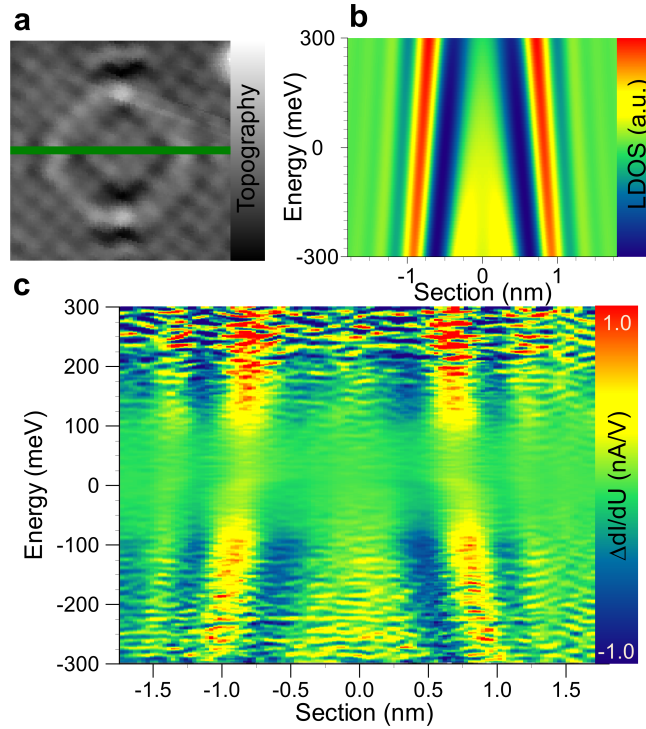

Figure 6.5: Signature of Ag 7ML impurity. (a) Topography $(2.4 \times 2.4\,\text{nm}^2, U = -10\,\text{mV}/I = 2.0\,\text{nA})$ (b) Tight-binding simulation of spectroscopic section $(\eta = 1.0\pi, h = 5\,\text{Å})$. (c) Experimental spectroscopic section $(U_{\text{set}} = -300\,\text{mV})$. The maxima and minima resemble quantitatively the simulation in (b) and show at the Fermi level an additional bending.

The surface signature of a 5ML Ag impurity in Fig. 6.6 confirms the findings described above for the 7ML impurity. Despite the drift in the data set (the topography in (a) was recorded during the STS measurement and shows a slight asymmetry due to thermal drift of the sample with respect to the tip), all the previously discussed characteristics are identified. The ring-like structure, here the dark contrast left and right and two merging maxima in the center, is governed by dispersion. It also shows a kink at zero bias, which is easiest to identify for the
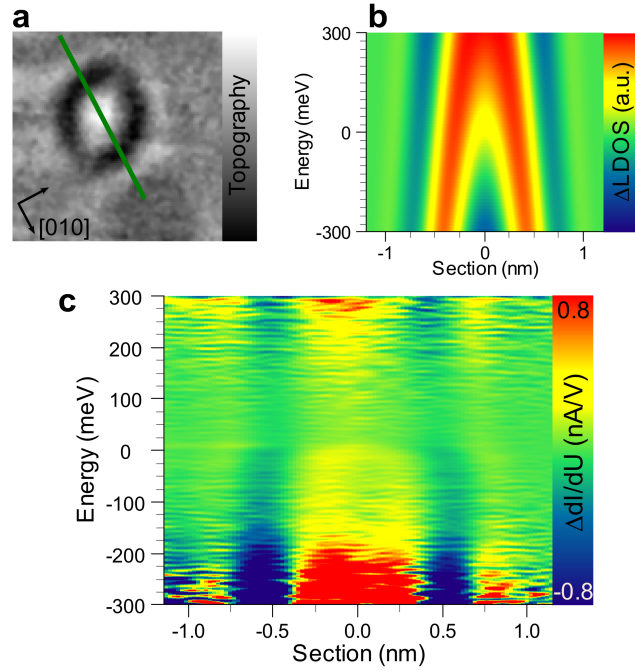
Figure 6.6: Signature of Ag 5ML impurity. (a) Topography recorded during STS measurement $(2.4 \times 2.4\,\mathrm{nm}^2, U = 300\,\mathrm{mV}/I = 1.0\,\mathrm{nA})$ shows drift along slow scan axis. Green line indicates the position of spectroscopic sections. (b) Tight-binding simulation of spectroscopic section $(\eta = 1.32\pi, h = 7\,\mathrm{\AA})$. (c) Experimental spectroscopic section $(U_{\mathrm{set}} = 300\,\mathrm{mV})$. Apart from dispersion, the pattern shows a distinct bending at the Fermi level.

minima. The different shape in the tight-binding simulation in comparison to the experimental data, especially the depression in the center for low energies, can be explained by the drift and the use of the average effective scattering phase shift.

A comparison with Ge shows: like the topographies, the spectroscopy sections of the same impurity depth resemble each other. For both species, we find the kink in the dispersion at the Fermi level. Especially for both 5ML patterns the inbound shift is very similar. For the 7ML Ge impurity (Fig. 6.1), the kink cannot be identified probably due to the high noise. The origin of this zero-bias feature is assumed to be a renormalization of the band structure and will be discussed in detail in Sec. 6.4 below.

Apart from the described characteristics, both species do not show any additional features like resonances in the studied energy interval. This should be visible as a phase shift in the spectroscopic section, but for $\pm 300\,\mathrm{mV}$ we only find an almost linear dispersion.

6.3 Comparison with Ab-Initio Calculations

Having described the methods of KKR-DFT ab-initio calculations in Sec. 3.7, here we present the calculated spectroscopic sections for a comparison to the corresponding experimental data. Figure 6.7 shows a collection of simulations for the experimental data sets shown in the previous sections, i.e. 5ML and 7ML impurities of both species Ag and Ge. The first-principles calculations show richer interference patterns than the tight-binding simulations because in addition to the host band structure they comprise the full crystal potential and solve the system self-consistently.
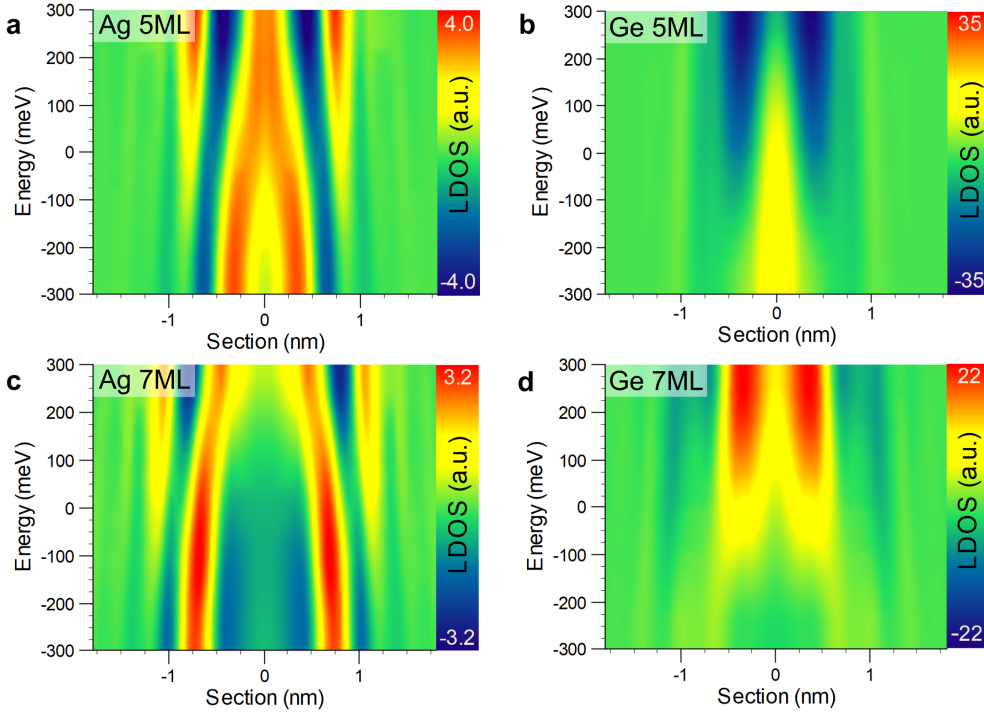

Figure 6.7: Spectroscopic sections calculated by ab-initio KKR-DFT calculations for a tip height of $h = 3.61\,\text{Å}$. (a) 5ML Ag (b) 5ML Ge (c) 7ML Ag (d) 7ML Ge. The lateral sizes of the interference pattern are similar for both species for a given depth. While the Ag patterns show mostly dispersive features similar to the experiment, the Ge data is governed by strong features in the center ($x = 0\,\text{nm}$). Only in the outward part of the pattern, Ge shows dispersive structures. Courtesy of M. Bouhassoune and S. Lounis (FZ Jülich).

For the Ag patterns, the shape is mostly governed by interference maxima and minima that generally follow a dispersive course. The line shapes are not as linear as in the tight-binding model and the ΔLDOS amplitude modulates with energy. Both, 5ML and 7ML, show a feature at around $150\,\text{mV}$ like a tentative phase shift that moves the pattern inbound and is not simply described by the host band structure.

A scattering resonance is unlikely because the calculated phase shifts (see Sec. 3.7) are inconspicuous in the corresponding energy range. Presumably, interference effects between different orbital contributions lead to the observed feature. These result from the solution of the Dyson equation that links the Green's function propagator of the investigated system with the propagator of the pure host and the orbital-specific scattering matrices. This can also be responsible for the different amplitudes at different energies, as the single orbital scattering amplitudes $|\Delta T|$ do not vary strongly over energy.

The Ge patterns are dominated by a strong feature in the center of the surface signature. The 5ML calculation shows an inversion of contrast from negative to positive energies, including a change of which lateral position shows the strongest ΔLDOS signal. This cannot be described solely by electron focusing of host electrons as the focusing angle does not change so significantly within this energy interval. Only in the outer regions the simulated Ge signature reminds of a 'regular', dispersive pattern similarly found for Ag. These findings hold for both Ge patterns despite their different shapes.

Comparing the ab-initio calculations of Ag and Ge, they show more differences than similarities. The lateral size, where the pattern is non-zero, is similar, but the pattern shapes are very distinct. The Ge signal is up to a factor of 7 higher in amplitude than for Ag in the same depth.

How do these images connect to the orbital-resolved values of phase shifts δ and t-matrices that were obtained by the KKR-DFT calculations (see Sec. 3.7)? The scattering amplitude, $|\Delta T|$, is higher for Ge than for Ag by a factor of 4 to 8, so the increased ΔLDOS is comprehensible. Especially for s- and p-type electrons the scattering is a lot stronger. Concerning the scattering phase δ, mainly responsible for the pattern's shape, for s and p orbitals the values differ while for d orbitals a similar phase is obtained. However, in the (for the STS pattern more relevant) phase of scattering matrix $\arg(\Delta T)$, the small change in δ_d leads to an inversion between Ag and Ge.

From the orbital-resolved tight-binding simulations (Sec. 3.6), we know that in the center area of the interference pattern we find contributions from all orbitals, but the most outward areas are dominated by d-like electrons. In the calculated signatures in Fig. 6.7 we find dispersive features that are inverted for Ag and Ge, which was expected from the scattering phases. It is consistent that the strong sp features for Ge lead to an excessive amplitude in the central part of the pattern which covers
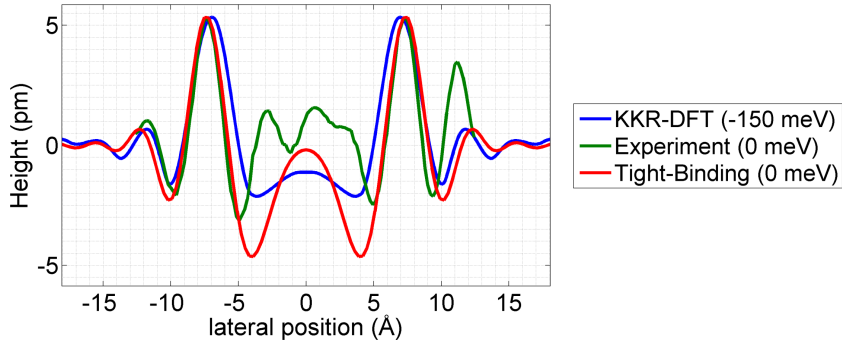
Figure 6.8: Sections of experimental and simulated STS data for an Ag 7ML impurity.
When the DFT data (blue) is shifted by 150 mV, it matches the patterns
from the experiment (green) and the tight-binding simulation (red). The
deviations for the experimental data in the center are due to superimposed
atomic resolution in this data set.

possible contributions from the d orbital. Even if the d orbital's pattern continued
into the center with its dispersive shape, like it is found in the outward regions, it
would be masked by the other orbitals' features.

There is no well-reasoned visual motivation why the Ge impurity shows such a
different interference pattern in the ab-initio calculation. However, one could expect
rather large perturbations of the host crystal because of the three more electrons the
impurity introduces into the system on an atomic level and the strongly increased
alloy resistance on a macroscopic scale.

In the next step, we will compare the ab-initio calculations with the experimental
results. For Ag, we find adequate agreement for the pattern shape. The peak
positions match best when the ab-initio data are shifted by 150 mV, which is not
unusual since it is known that DFT can have difficulties to obtain an absolute energy
scale. This is visualized in a comparison of sections of experimental and simulated
data in Fig. 6.8 where pattern shape and lateral size match. In the DFT data,
the experimentally observed kink around zero bias is not retrieved and has to be
explained beyond the model's assumptions.

The experimental Ge patterns do not match with the simulations from first
principles, neither in shape nor position. This is not surprising, since the DFT
simulations are so different and the experimental patterns so similar when comparing
both species. In the experimental Ge data (c.f. Fig. 6.1, Fig. 6.2), we do not find
the peculiar, dominating feature in the center, which is attributed to *sp* electrons.
Instead, the overall shape shows dispersive lines which correspond to the 'ring-like
structures' found in the topography. In the outward regions ($r > 8\,\text{Å}$), that we

know is *d*-orbital-governed, both experiment and calculation, show this type of shape. Therefore, we attribute the signal in the experimental Ge interference patterns to mainly *d* electrons.

For an explanation of this behavior, it has to be noticed that our experiment is designed to probe only the contributions of coherently scattered electrons for which incoming and scattered waves interfere constructively or destructively at the surface. In the experiment, we find coherent scattering for Cu electrons with mainly *d* character, while we cannot detect signatures of coherently scattered *sp* electrons despite being predicted by the KKR-DFT calculations. Hence, we assume that there are additional processes present in the sample system that induce incoherence, which so far are not taken into account by the ab-initio calculations.

In general, incoherence can be introduced during electron propagation or during scattering at the impurity. For the propagation, the bulk electron coherence including electron-electron interaction at low temperatures has been assumed to be several dozens of nanometers for energies of 1 V from the Fermi level [196, 197]. The distances in our experiment of a few nanometers are significantly shorter. The *k*-dependence of relaxation times for bulk electrons due to electron-phonon interaction was studied by Mustafa et al. in ab-initio studies [150]. For regions of the Fermi surface close to the necks and in ⟨100⟩ directions, they found scattering rates three times higher than for the flat regions. Although this trend would fit the observed missing *sp* contributions, all coherence lengths – even including the strong anisotropies – are still more than an order of magnitude larger than the experimental paths. Thus, incoherence induced during the electron propagation is assumed to be negligible for the most part.

Instead, we propose a partially incoherent scattering process of *sp* electrons at the Ge impurity. It reduces the signal in our (coherently probed) experiment and causes the differences with respect to the ab-initio calculations. These findings suggest that the substantially higher residual resistivity of Ge impurities in Cu than for Ag atoms could partly be attributed to incoherent impurity scattering of the *sp* electrons.

These considerations about the visibility of different orbital contributions elucidate the question why Ge and Ag show almost identical surface signatures in the STM measurements. For Ag, the ab-initio calculations find similar effective phase shift values for all orbital contributions and all orbitals have rather weak scattering amplitudes. This matches to the experimental data that consists of a dispersive pattern without strong features. It is constituted from all orbital characters and especially *d* electrons because of their strong orbital contribution in electron focusing. For Ge,

while *sp* contributions govern the ab-initio data, we assume *d* electrons to dominate the experimental pattern. The KKR scattering phases for Ag and Ge are similar for the *d* orbital which, at first glance, does explain why the interference patterns for both species resemble each other. However, decisive for the surface signature is the phase of the scattering matrix $\arg(\Delta T)$ which includes the contributions from the host (c.f. Sec. 3.7). This quantity is almost inverted for Ag and Ge, despite being close in the complex plane as discussed previously. In contrast, the resembling experimental data indicate that the effective scattering phases lie within the same quadrant of the complex plane. There are two possible explanations for deviations in the calculations. Firstly, the DFT calculations are performed without relaxations of the Cu atoms because often they are small and therefore negligible [198]. A change in the connection from the impurity lattice cell to the host crystal potential, e.g. due to relaxation, is usually described by a 'backscattering phase shift'. Braspenning et al. have found a backscattering phase shift value that does not fully suffice to invert $\arg(\Delta T)$ [158], but points towards that direction. As the buried impurities in our experiment are located close to the surface, this can lead to a further enhancement of backscattering. Secondly, numerical inaccuracies might occur, e.g. the results might be a local minimum in the optimization routine instead of the absolute minimum, as the Ge patterns are governed by *sp* contributions, so that the *d* contribution only plays a minor role. Furthermore, also small errors in the phase shift value of Cu δ_{Cu} can contribute additionally.

One might raise an alternative explanation of the apparent inversion between experiment and ab-initio calculation for the Ge data. The depth determination via atomic resolution is limited to a statement whether even or odd lattice layer. Furthermore, a comparison of two patterns of depths d and $d + 2\,\mathrm{ML}$ shows approximately an inversion. This is reflected in the tight-binding model where a shift of $d = 0.1\,\mathrm{ML}$ corresponds shift in phase of 0.14π, i.e. two layers correspond to 3π, which is identical with a flip of the pattern shape. Therefore, one could suggest that we have identified the depths for Ge wrongly and they are two layers deeper. This is very unlikely because of comparisons of lateral size. We find a similar pattern size comparing experimental and DFT data for Ag, as well as comparing both species in ab-initio simulations. Therefore, we expect the lateral sizes for Ge also to resemble between experiment and simulation which is only the case for the given depths, and not two layers deeper. As the lateral size of the interference pattern is mainly governed by the electron focusing properties of the host, i.e. the focusing angle, the pattern sizes

for different species are expected to be similar.

At the end, we want to return briefly to the spectroscopic data in large energy intervals presented in Fig. 6.3. In the ab-initio calculations, at the Fermi level larger scattering amplitudes were found for the Ge impurities than for Ag. For an energy range up to $1\,\mathrm{eV}$ the ΔLDOS calculated by KKR-DFT increases even further by a factor of 2–3. This holds especially for the features in the center that we attribute to s and p orbital contributions. Yet, in the experimental data, we do not find any significant amplification of signal towards high energies. The set point for Fig. 6.3(e) is at negative bias ($U = -1\,\mathrm{eV}/I = 0.5\,\mathrm{nA}$), so that we do not expect any influence because of the constant current set point and the resulting different tip heights. Hence, the missing rise in amplitude in this large energy STS is another hint towards our explanation of incoherent sp scattering.

6.4 Low-Bias Features and Many-Body Effects

In the following, we will focus on the low-bias features that we found for both non-magnetic species. The 4ML Ge impurity, first presented in Fig. 6.3, shows a well-pronounced kink at the Fermi level which is mapped in high energy resolution in Fig. 6.9. The minima seem to experience a phase shift and move towards the center. The center maximum fades, making room for the features moving towards the center. In energy intervals as small as $\pm 100\,\mathrm{meV}$ or $\pm 50\,\mathrm{meV}$, the overall dispersion can be approximated as vertical linear slope which is in agreement with the tight-binding simulation in Fig. 6.3(c).

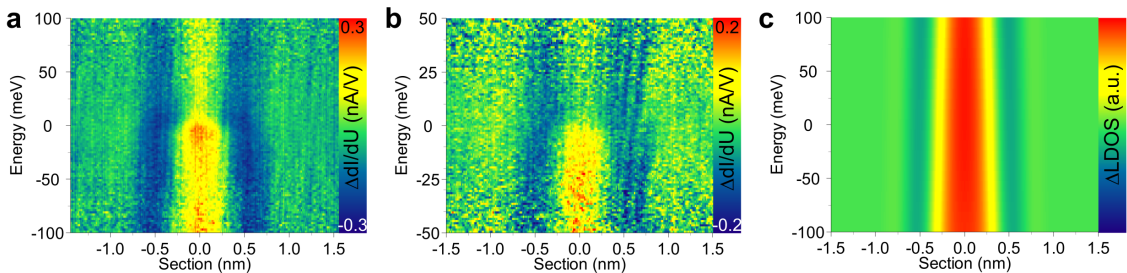As stated above, also for Ag such kink-like features around the Fermi level are

Figure 6.9: Low-bias feature for Ge 4ML impurity. Spectroscopic sections for (a) $U_{\mathrm{Set}} = -100\,\mathrm{mV}$ and (b) $U_{\mathrm{Set}} = -50\,\mathrm{mV}$. (c) Tight-binding simulation ($\eta = 1.23\pi, h = 7\,\text{Å}$) has a similar overall shape, but does not reproduce the kink at the Fermi level. The same impurity's patterns are shown for larger energy intervals in Fig. 6.3.
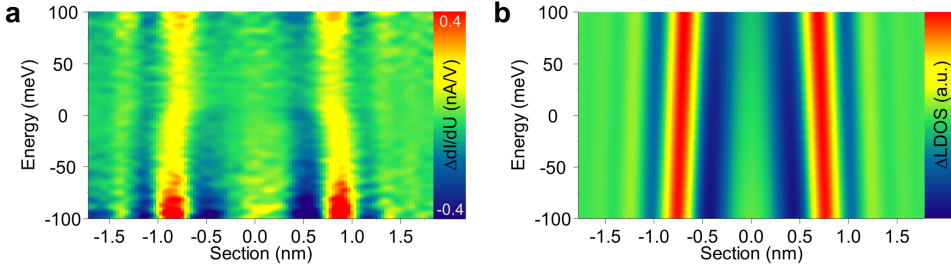
Figure 6.10: Spectroscopic feature around zero bias at 7ML Ag impurity. (a) STS section with high energy resolution as zoom-in of Fig. 6.5. (b) Tight-binding simulation ($\eta = 1.32\pi, h = 5\,\text{Å}$) shows linear dispersion, but does not reproduce the bending at the Fermi level.

found. It is clearly visible in Fig. 6.10, which shows an energetic zoom-in for the Ag 7ML impurity depicted in Fig. 6.5. The tight-binding simulation matches the overall pattern shape and lateral size, but does not contain the additional bending. For both species Ag and Ge, the deviation from electron dispersion is located at the Fermi level and is neither found in the tight-binding nor in the ab-initio calculations.

A phase shift at the impurity can occur at the energy of an electronic resonance, which, e.g., originates from a hybridization of bulk states with impurities. For example, such a phase shift is found for magnetic impurities due to the Kondo resonance [22]. However, considering the two non-magnetic species in our experiment, it would be extremely unlikely if by chance such resonances were located for both species exactly at the Fermi level and, moreover, are not predicted by the first-principles calculation. Instead, we assume further interactions of the electrons with the solid, either during propagation or at the impurity, to give rise to this feature.

6.4.1 Many-Body Renormalization of Surface Signatures

Both impurity species show similar low-bias features in an energy range of approximately $\pm 30\,\text{mV}$, which are not found in the simulations. To explain these deviations, an obvious candidate for an additional interaction in this energy range are vibrational modes since the Debye energy for Cu is $\hbar\omega_D = 29.6\,\text{meV}$ [67]. In our sample system, there are two possibilities for electronic interaction with lattice vibrations. Firstly, the impurity atom can induce local vibrational modes. Secondly, electron-phonon interaction can occur with delocalized Cu bulk phonons. We would expect different local vibrational modes for both species, because Ag is significantly heavier than Ge. Yet, we find a very similar behavior of the species' signatures. Therefore, we suspect
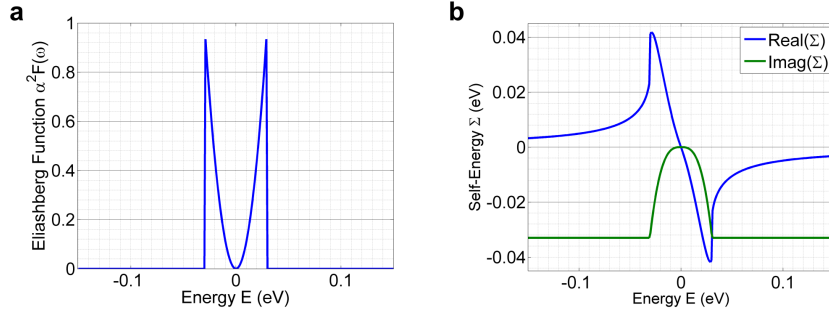
Figure 6.11: Electron-phonon coupling in a Debye approximation for exemplary values of $\lambda = 1.0$ and $\hbar\omega_D = 30\,\text{meV}$. (a) Eliashberg function $\alpha^2 F(\omega)$. (b) Real and imaginary part of the self-energy Σ.

that electron-phonon interaction of Cu bulk states with Cu crystal phonons leads to the additional features at zero bias. While so far we have mainly investigated the scattering properties of the impurity, we are now shifting the focus to the host material.

As described in Sec. 3.8, a kink in the band structure $E(k)$ is known as a renormalization of the dispersion relation due to many-body interactions. The real part of the corresponding self-energy shifts the dispersion in energy and the imaginary part causes broadening in k, which leads to a finite quasiparticle lifetime. Here, we characterize the real space signature of such a renormalization for a 3D bulk system.

In order to estimate the effects of many-body effects on the interference patterns in our experiment, we have extended the tight-binding model with self-energy corrections. We use the Debye model according to Eq. 3.60 with $\hbar\omega_D = 30\,\text{meV}$ to describe the Cu phonons. Fig. 6.11 shows the Eliashberg function and the corresponding self-energy for an exemplary value of $\lambda = 1.0$. The real part of the Debye self-energy is included into the calculation while we neglect the imaginary part, whose role will be discussed below. This simple approach does not include a directional dependence of $\alpha^2 F(\omega)$ on electron momentum k and assumes particle-hole symmetry in the self-energy.

Figure 6.12 illustrates how electron-phonon coupling changes the interference pattern by comparing the experimental data with a simulated interference pattern. The calculation shows obvious deviations from the calculation without many-body effects (c.f. Fig. 6.2b). The kink, which is found here in real space, corresponds to the well-known kink in momentum space. For $|E| < \hbar\omega_D$ the dispersion of minima and maxima shows a higher slope than for $|E| > \hbar\omega_D$. Also the latter regions are affected as they show a smaller slope than without electron-phonon interaction. Comparing the 2D data from calculation and experiment, we find good agreement for a coupling
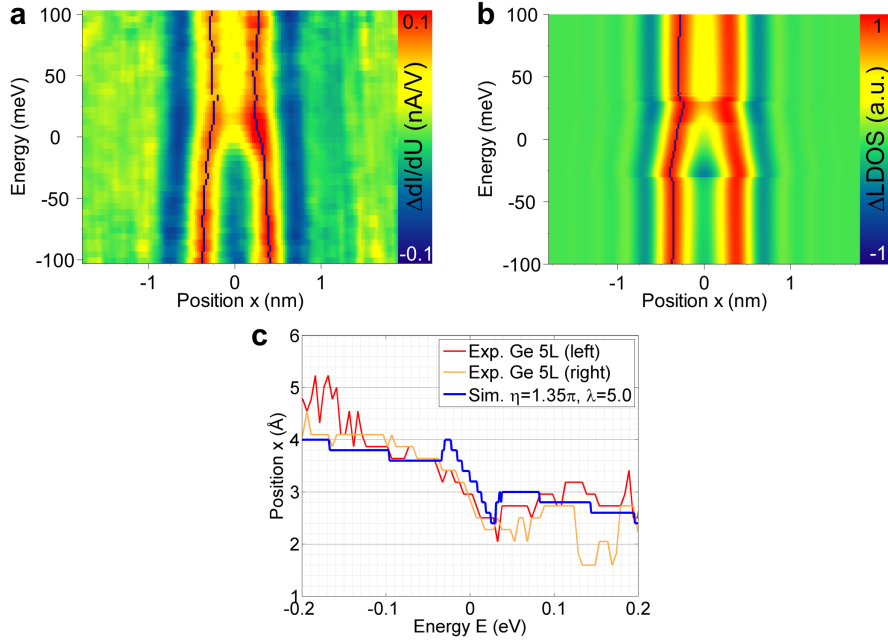
Figure 6.12: Spectroscopic signature of electron-phonon coupling for 5ML Ge impurity. (a) STS ($U_{\mathrm{Set}} = -300\,\mathrm{mV}/I = 0.7\,\mathrm{nA}$) with bending of the interference pattern around the Fermi level. The patterns' maxima are labeled in dark blue. (b) Tight-binding simulation including Debye electron-phonon coupling with $\lambda = 5.0, \hbar\omega_D = 30\,\mathrm{meV}, h = 5\,\mathrm{\mathring{A}}$. (c) Comparison of the position of the maxima in experimental (red/orange) and calculated (blue) data.

parameter of $\lambda = 5.0$. For example, for both it is resolved that at around $25\,\mathrm{mV}$ the maxima almost meet before bending outwards again for higher energies. The good agreement also holds for the 1D comparison for the position of the maximum in Figure 6.12(c). It shows a steep step around the Fermi level, while for $|E| > \hbar\omega_D$ the peak positions remain almost constant. In the tight-binding simulation, there are discontinuities found in the 2D data at $\pm\omega_D$ which are reflected in the bulges in the 1D comparison. These can be linked to numerical resolution and the Debye model which contains an abrupt cut for the phonon density of states. In contrast, due to thermal broadening and experimental resolution, the experimental data is smoothened.

For Ag, Fig. 6.13 gives a similar picture for the comparison of experimental and tight-binding spectroscopic sections including many-body effects. Similarly to Ge, the simulated interference pattern shows an additional bending in an energy interval $[-\hbar\omega_D, \hbar\omega_D]$ which matches with the experimental findings. The comparison in Fig. 6.13(c) shows, like for the other non-magnetic species, a step in the dispersion at the Fermi level.
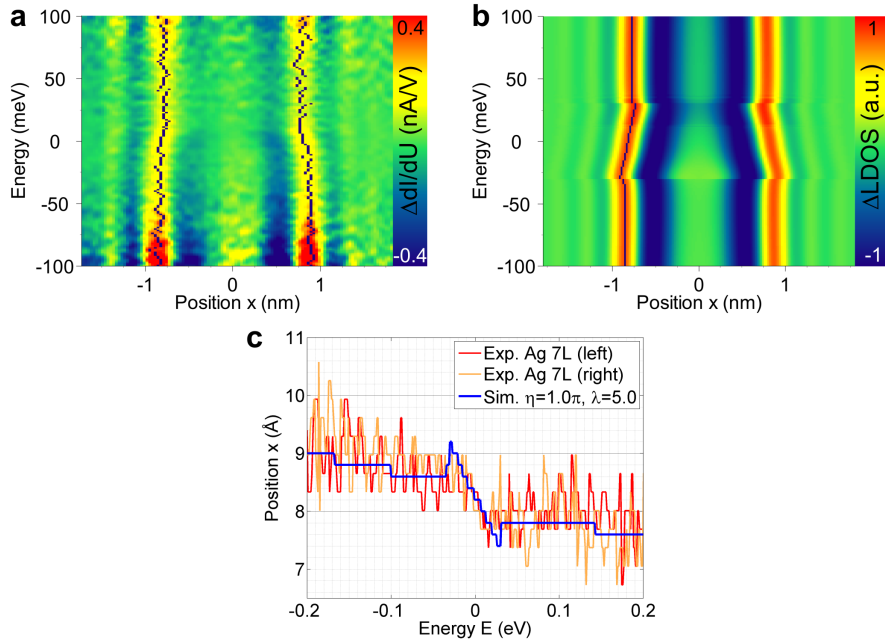
Figure 6.13: Spectroscopic signature of electron-phonon coupling for 7ML Ag impurity. (a) STS ($U_{\mathrm{Set}} = -300\,\mathrm{mV}/I = 2.0\,\mathrm{nA}$) with bending of the interference pattern around the Fermi level. The patterns' maxima are labeled in dark blue. (b) Tight-binding simulation including Debye electron-phonon coupling with $\lambda = 5.0, \hbar\omega_D = 30\,\mathrm{meV}, h = 5\,\text{Å}$. (c) Comparison of the position of the maxima in experimental (red/orange) and calculated (blue) data.

We find that the features around the Fermi level observed in the experimental data can be described by a self-energy from electron-phonon interaction that renormalizes the band structure. Since the interference patterns in real space are governed by electron focusing, which in turn relies on the electronic structure, the spectra reveal a real space signature of this renormalized band structure. The bending at low bias voltages can be interpreted as the real space visualization of the characteristic kink in momentum space, known from the experiments introduced in Sec. 3.8. This can open up a new experimental access to the study of many-body effects combined with the local resolution of an STM. Scatterers that show spectral homogeneity around the Fermi level can be functionalized to visualize the bulk dispersion in real space including deviations from the single-particle band structure. This approach is not limited to electron-phonon coupling and the Debye model used here, but can also be used to describe other self-energies of other many-body interactions.

6.4.2 Imaginary Part of the Self-Energy

We could show that both species could be described by including the real part of the self-energy into the tight-binding model while a full description would also include the imaginary part. We studied the role of the imaginary part in a simple 1D toy model adapted from [199], where the quadratic dispersion of a free electron is approximated by a linear dispersion around the Fermi energy ($E_F = 7\,\text{eV}$). The many-body effects are introduced by self-energy corrections from Debye phonons, similar to the Eliashberg function used above.

The results of this calculation are shown in Fig. 6.14. The renormalized spectral function in momentum space shows the expected kink at the Debye energy. The imaginary part causes broadening of the dispersion, which is strongest for $E > \hbar\omega_D$. The real space representation of the Green's function propagator is obtained via a Fourier transform and is then used to calculate the real space patterns in Fig. 6.14(b-d) for a 7ML impurity. For this 1D model, the Friedel oscillations show a constant amplitude even for large distances. This is why we include a distant-dependent
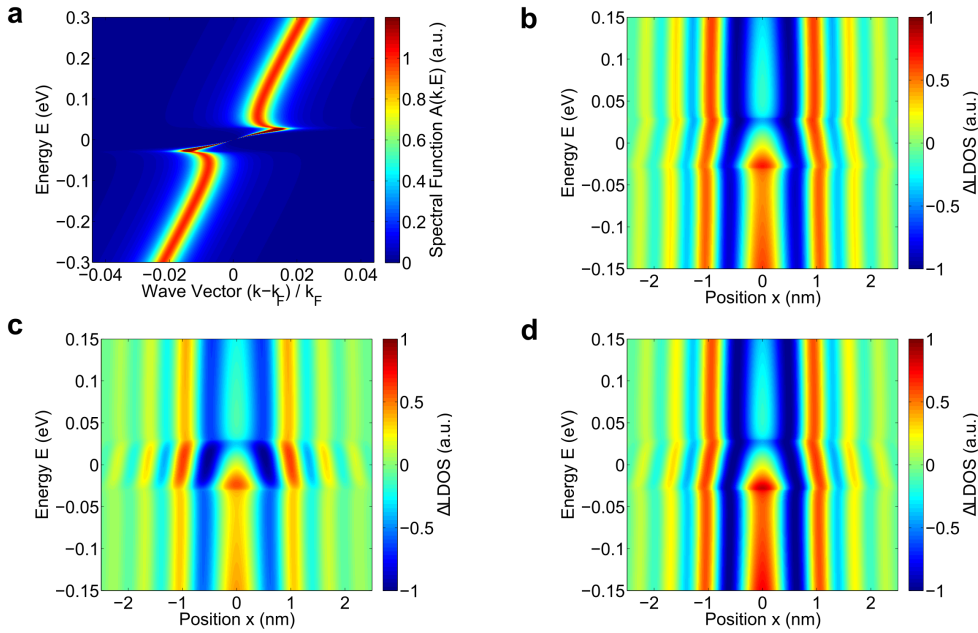
Figure 6.14: Effect of the self-energy's imaginary part on the interference patterns in a 1D toy model ($\lambda = 5.0, \hbar\omega_D = 30\,\text{meV}$) for a 7ML impurity ($\eta = 1.0\pi$). (a) Momentum space spectral function with characteristic kink from many-body interactions. (b) Real space spectroscopic pattern with $\Sigma = \text{Re}\,\Sigma$. (c) Real space spectroscopic pattern with full self-energy. (d) Same as (c) with normalization in ΔLDOS for each energy.

additional damping factor $\propto r^{-3}$ to account for the 3D propagation like in the experiment.

When only considering the real part of the self-energy, the interference pattern shows the bending in an energy interval determined by the Debye energy and a constant amplitude with energy. The decay of amplitude with distance is only given by the Friedel damping term. For the full self-energy in Fig. 6.14(c), the imaginary part reduces the signal's amplitude. Around $0\,\mathrm{eV}$, the pattern remains almost unchanged, while for $|E| > \hbar\omega_D$ the signal is attenuated by approximately 50%. When this reduction is eliminated by normalizing the ΔLDOS for each energy in Fig. 6.14(d), the pattern for the simulation with only the self-energy's real part is recovered. This shows that the positions of maxima and minima remain the same when the imaginary part is included. It only determines the signal's amplitude, but leaves the pattern shape unchanged. Therefore, it is valid to only include the real part of the self-energy into the Cu bulk calculation presented above.

6.4.3 Discussion of Electron-Phonon Parameter λ

In the analysis of the experimental data, we find that a value of $\lambda = 5.0$ reproduces well the features around zero bias. This is very high compared to the Cu bulk value $\lambda_{\mathrm{Cu}} = 0.15$ in the literature or even materials with strong electron-phonon coupling like Pb ($\lambda_{\mathrm{Pb}} \approx 1.5$) or PbBi alloys ($\lambda \approx 3.0$). For the Cu bulk value the simulated interference patterns show almost no deviations from the calculations without interactions. We do not expect the tight-binding model to exactly quantify the phenomena, as it does not consider all contributions from the solid. Nevertheless, this large deviation of approximately a factor of 30 will be discussed in the following.

The bulk value of $\lambda_{\mathrm{Cu}} = 0.15$ is a quantity that is averaged over values with a directional dependence $\lambda(\mathbf{k})$. For Cu, for different positions on the Fermi surface λ can take values between 0.08 and 0.23 [150, 167, 200]. This k-dependent variation of a factor 2 to 3 cannot account alone for the large difference between $\lambda = 5.0$ and the bulk value λ_{Cu}, although the electron focusing patterns in the experiment are constituted from specific regions of the isoenergy contour with the corresponding group velocity, and therefore k values.

Since the bulk alone cannot explain the large electron-phonon coupling parameter, we suggest the vicinity of the surface to be crucial for the enhancement of λ. At the surface, additional electronic surface states and phonon modes are available. More relevant for the bulk propagation is the missing translational symmetry that breaks

the momentum conservation perpendicular to the surface. This opens up additional scattering processes for the electronic bulk states that can interact with more bulk and surface phonon modes and that have more final electronic states available. The bulk selection rules become less strict and enable more electron-phonon interaction which would strengthen the deviations from the single-particle dispersion.

While surface-near bulk properties are only scarcely investigated, electron-phonon coupling has been studied for the bulk, e.g. by cyclotron masses [167], or for defined 2D systems like surface states. For the latter, surface-sensitive techniques like ARPES and STS have been used to analyze numerous sample systems and to determine values of the coupling parameter λ or self-energy Σ. For various surface states, Mo(110) [7], Cu(111) [8, 170, 171, 201], and Cu(110) [202] as well as the Pb(110) bulk state [201], values similar to the respective λ_{bulk} were obtained. Also in different approaches by STM, electron-phonon coupling parameters and self-energies were found in agreement with ARPES and bulk data. Grothe et al. quantified many-body effects of the Ag(111) surface state by QPI [17] and also for other 2D systems like graphene flakes on graphite [15] and the surface state of the bulk insulator PbSe [16], the literature values were reproduced by Landau level spectroscopy.

In more detail, it is found that the coupling of specific electronic states and phonon modes can show strong variations with respect to an averaged λ and shows an energy dependence [203]. The different contributions to the lifetime of surface states, i.e. scattering within the surface band, with bulk electrons, bulk phonon states as well as surface modes, have been studied for different noble metals [10–12]. For the Cu(111) surface state, the predicted influence of specific bulk phonon modes was experimentally confirmed [171]. The Eliashberg function, which characterizes the interaction with specific phonon modes, could directly be extracted without assumptions on phonon models for the Be($10\bar{1}0$) surface [9], finding an enhanced λ due to coupling to low energy surface modes that are not present in the bulk phonon spectrum. These findings were crucial for understanding the very high value of $\lambda \approx 1$ for the Be(0001) surface, four times higher the bulk value [159], that was found in ARPES measurements [204–208]. For Pd(111), it was shown that, despite weak directional anisotropy of λ, the coupling parameter significantly depends on the particular surface electronic band ($\lambda = 0.4...>1$) [209]. While these findings only relate to the respective surface in question, it becomes clear that the detailed phenomena related to electron-phonon coupling cannot necessarily be described by an average parameter λ.

Also for thin films, electron-phonon coupling was found to be dependent on the specific configuration of electronic states and phonon modes. Although these systems, like the surface-near bulk impurities in our experiment, are governed by the presence of surfaces and interfaces, it has to be noticed that the quantum well states (QWS), which exist in thin films according to their depth, differ from the bulk states that are mapped in the electron focusing interference patterns. In thin Ag films, the Fermi-level crossing of QWS for distinct film thicknesses and, thus, additional coupling to phonon modes is responsible for depth-dependent oscillations in measured values of λ [210, 211]. Also the orbital character of the QWS can contribute significantly, showing a factor of up to 35 for different states [212], and electronic transitions from a quantum well resonance into a quantum well state can enhance electron-phonon interaction probabilities [213].

All in all, it becomes apparent that for a full picture of electron-phonon coupling all possible interactions have to be taken into account on a state-specific level. This includes all available final electronic states, available phonon modes (surface and bulk) as well as the matrix elements for the corresponding scattering processes. An additional component under this aspect could be local, spatially extended lattice vibrational modes. These might be localized within a range of several nanometers around the impurity that induces them. Then, since we probe very locally, such a mode could become indistinguishable for us from a regular bulk phonon.

In our experiment, we investigate a 3D system which is determined by the bulk electronic structure with additional contributions from the vicinity of the surface and the resulting weakened selection rules for interactions. While the exact origin of the high value of the electron-phonon coupling parameter $\lambda \approx 5$ remains unclear, this can be a possible reason why it is significantly enhanced with respect to the bulk.

Despite the preceding remarks, we realize that the value of λ is unusually high. The model of electron-phonon coupling with an appropriate choice of parameters does describe the experimental data, but also another many-body electron-solid interaction with similar self-energy would be possible as cause for the low-bias features. However, we cannot identify a suitable collective excitation for the studied system for the given energy range. Therefore, we conjecture that the detected features are linked to the interaction of bulk electrons with lattice vibrations.

While previous experiments have investigated two-dimensional surface states, here, we characterize a 3D system. By the comparison of two non-magnetic species, we find the kinks in the spectra to be the real space signature of the renormalization of

Cu bulk band structure due to many-body effects.

6.5 Outlook

There is a variety of research questions that can be explored in future experiments with subsurface impurities. On the one hand, these concern the scattering process at single atomic defects, and on the other hand how impurities can be functionalized for further insights into material properties and many-body effects in a solid.

An obvious addition to the experiments presented here, is the study of further impurity species in Cu(100). For example, Si is electronically similar to Ge, including almost identical scattering phases, but is significantly lighter. Such an investigation could shed light on the role of sp contributions in the scattering process and for the interference pattern. Also, such a similar species would allow for comparisons of scattering amplitudes, i.e. topographic contrast of the surface signatures.

An intriguing candidate for investigation would be a non-magnetic impurity with a considerably different scattering phase for the d orbital than Ge or Ag. However, according to the literature [158], generally the effective scattering phase is almost always the same for all species considered. This matches with the fact that Ag and Ge, as well as the magnetic impurities Co and Fe, show relatively similar surface signatures. Larger differences for sp scattering, in both scattering phase and amplitude, would promise e.g. oxygen, sulfur, antimony or tellurium.

By the investigation of more impurities, it may be possible to find a link between the effective scattering phase shift, used in the tight-binding model, and the ab-initio KKR-DFT phase shift. Eventually, this could result in an experimental confirmation of the value of KKR scattering phase of a single impurity atom in a host matrix.

A different choice of surface, e.g. Cu(111), or another host material, typically Ag or Au, might give a different access to the scattering properties. While for the Cu(100) surface, the outmost feature is almost exclusively given by d electrons, the focusing directions for another host might allow for the characterization of different orbital characters. For the (111) noble metal surfaces, the standing wave patterns of the surface state superimpose with the signals from subsurface impurities [20].

An alternative approach to disentangle contributions from different orbital characters (and potentially different scattering phases) is the investigation of many data sets of both already familiar impurity species Ag and Ge. In general, an experimental access to these questions is highly challenging because the STM only maps a single
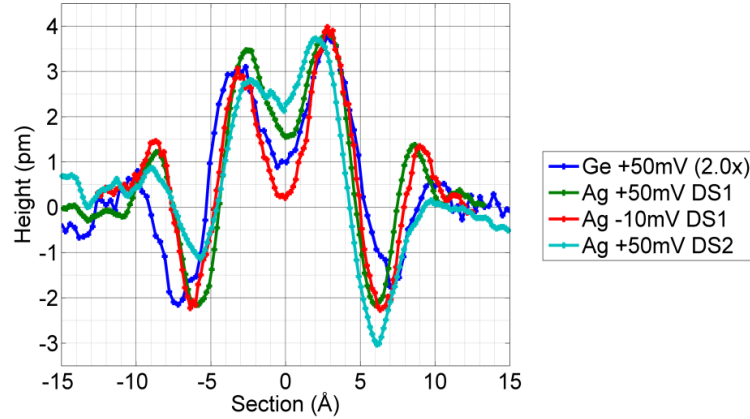
Figure 6.15: Comparison of sections for 5ML Ag and Ge impurities. Ag data (two different data sets DS1 and DS2) show similar peak positions. For Ge data set, the maxima at $x = 3\,\text{Å}$ are located similarly to Ag, the minima at $x = 7\,\text{Å}$ are further outwards. This might hint towards orbital-dependent differences in scattering phase shifts despite the similar overall effective scattering phase shift η for both species.

LDOS that is composed of all electrons whose wave function extends to the tip. We can simulate the orbital components in the tight-binding simulation, but as the model is already over-determined by its parameters, adding additional degrees of freedom, e.g. orbital-dependent scattering phases, will not yield unambiguous fit results. Yet, we know that the outmost features of the patterns are almost exclusively given by d-like electrons, so that a direct comparison of experimental patterns of two impurities of different species in the same depth can give access to differences in the d scattering phase shift. In order to obtain the data, imaging conditions, including set point and tip shape, need to be similar for both impurities so that potential differences originate with certainty from the scattering properties.

One example of such a comparison is presented in Fig. 6.15, which shows the difficulties of such an analysis. Generally, all Ag sections coincide with each other, but despite the same set point, both sections of Ag 50 mV in detail show different pattern shapes. The Ge data share the positions of the inner maximum with Ag, while at the outer minimum and maximum the peak positions shift outwards with respect to the other non-magnetic species. This could be related to a smaller effective scattering phase η for d electrons for Ge than for Ag. Such detailed analyses require very many data sets of both species with the same parameters and are a possible subject for further research.

Finally, we have shown that weak scatterers can act as probes for bulk phenomena. As the spectroscopic sections visualize the band structure in real space, we detect renormalizations due to collective excitations. These are not limited to vibrational modes, like electron-phonon coupling, but could range to interactions of magnetic or even topological kind. For example, in correlated materials like cuprates or iron pnictides the interaction with magnons could be investigated, where just recently an electron-magnon interaction of $\lambda = 6$ was suggested for $Ba_{1-x}K_xMn_2As_2$ in ARPES experiments [214]. Concerning lattice vibrations, a more quantitative analysis of the surface-near electron-phonon coupling or studying local vibrational modes of subsurface impurities or clusters are possible topics of future investigations.

7 Conclusions

In this thesis, single non-magnetic impurities buried in the bulk metal Cu have been studied to characterize their scattering properties as well as the electronic structure of the host. This is possible by analyzing the interference patterns that form on the surface by directionally propagating electrons due to electron focusing. The coherent superposition of incoming and outgoing waves leads to variations in the LDOS, which can be studied topographically and spectroscopically with the STM. These signatures are defined by the properties of the propagation through the host as well as the scattering event at the interference site.

To enable such investigations, we have identified a low temperature preparation method to reproducibly prepare dilute surface alloys of Cu and Ge suitable for investigation on the atomic scale. The interference patterns of impurity atoms up to 17 layers below the surface, corresponding to a path length of 7 nm, were successfully identified. The depths are determined using atomic resolution data as well as the lateral extent of the patterns. A plane wave tight-binding model reproduces the topographies with high accuracy and enables the identification of the depth of deeply buried impurities. We find that a single effective scattering phase shift, independent of depth and energy, describes all experimental data of one species. With $\eta_{\mathrm{Ge}} = 1.23\pi$ and $\eta_{\mathrm{Ag}} = 1.32\pi$, the values for the two compared non-magnetic elements Ge and Ag are similar, which is also reflected in resembling topographies.

A tight-binding calculation resolved by electronic orbitals reveals the different orbital characters of states on the Fermi surface and their role for electron focusing. That it is possible to describe the surface signatures with a single orbital-independent effective scattering phase shift is due to the fact that the flat electron focusing regions of the Fermi surface, and thus also the interference patterns, are dominated by a single orbital character, namely the d electrons. Moreover, a significant fraction of sp scattering as found in KKR-DFT ab-initio calculations and intuitively expected at the sp impurity Ge, is absent in the experimental data. We conclude that the corresponding scattering events occur incoherently.

Spectroscopically, the studied atomic species are inconspicuous, unlike magnetic Kondo scattering centers. Therefore, the change of the surface signatures with energy, converging ring-like structures, mainly describes the band structure of the host. We can reliably trace this progression with the tight-binding model and clearly identify it as contribution of the host rather than the impurity. Thus, the spectroscopically resolved interference pattern of a buried impurity becomes a real space signature of the electronic structure of bulk Cu.

We use this novel access to the band structure for the characterization of a bending found in the experimental data around the Fermi level. This feature occurs with similar strength for both species studied in an energy interval of $30\,\text{mV}$, so we assume its origin to be many-body interaction during electron propagation. From the clearly visible kink at zero bias, we extract a value for the electron-phonon coupling parameter $\lambda \approx 5$ that is significantly higher than the known value for the bulk or surface states. This could be explained by the fact that the probed bulk electrons interact with phonons in the vicinity of a surface, so that due to this symmetry breaking additional scattering channels are available by less strict selection rules for electron-phonon coupling. Moreover, the literature shows that for a complete description, the coupling must be considered at a state-specific level, and this implies a complex task to include all states and possible local modes for the system of a bulk defect near a surface. In summary, we find that the surface scattering patterns allow us to map the bulk band renormalization and thus provide a real space signature of many-body effects within a solid.

Resolving the electronic structure is crucial to understanding many properties of a material. In particular, the electrons around the Fermi energy are essential for its electronic, thermal and magnetic properties. For band structure measurements, the first choice are versatile photoemission experiments, yet they are limited by the occupation of states and spatial resolution. As a complementary approach, we present a local probe that can be used to study many-body effects in the electronic structure in real space. By functionalizing inherent defects that act as weak scatterers, the STM can characterize the interaction of electrons with collective excitations, such as phonons, in both bulk and surface nanostructures. In light of the continuous miniaturization of nanoelectronic devices, this technique can help understand such fundamental processes on the atomic scale.

A Influence of the Probe

The quality of the probe is crucial for the investigation of surface signatures of buried atoms in Cu. Already Sprodowski et al. discussed the role of tip sensitivity in their focusing experiments on Ag [129]. The measured apparent heights in the topography data are at the resolution limit of only a few picometers. These correspond to LDOS modulations of approximately 1% in the spectroscopic data $I(U)$. In order to analyze these small differences, the presented STS data is usually depicted as $\Delta\,\mathrm{d}I/\,\mathrm{d}U$ in comparison to the pristine Cu surface.

For high-resolution measurements of the interference patterns and their spectroscopic signatures, sharp and stable tips are an absolute necessity. A blunt tip can cause a broadening in the data, similar to a Gaussian filter, as described in [134]. This can make it difficult to distinguish clearly defined interference patterns of buried impurities from other defects like first layer impurities or adsorbates. This applies in particular to impurities in upper layers, e.g. 4ML, whose signature is mainly a simple protrusion with a surrounding depression (c.f. Fig. 5.6). Such pattern could easily be confused with the signature of a first layer defect of another species. If it is unknown what is the origin of a surface pattern, the data sets are not used for the analysis of subsurface impurities.

One example of an undefined surface pattern is depicted in Fig. A.1. On first sight, its topographic appearance reminds of an electron focusing interference pattern, whose rather large lateral size and blunt shape might be influenced by the tip shape. The spectroscopic signature for $\pm400\,\mathrm{mV}$ reveals a movement of the positions of minima and maxima towards the center which is significantly stronger than for electron focusing patterns. This leads for the larger energy scale of $\pm1\,\mathrm{V}$ in Fig. A.1(c) to multiple 'boomerangs' of minima and maxima which is in contradiction to other data, e.g., the 4ML pattern shown in Fig. 6.3(e). These discrepancies cannot be explained by simulations in the tight-binding model either, where various parameters like impurity depths were tested. Also the parameter of tip height, which has a decisive influence on the pattern shape via the lateral frequencies $k_{\parallel}$ present, could

not be tuned to reproduce the shown data set. Therefore, we assume that this surface feature is either given by a defect in the or close to the surface layer or, alternatively, could be related to a buried nanocavity, e.g. filled with sputtering gas Ar. If the surface pattern is constituted of quantum well states, then their constructive or destructive interference at the surface, as measured in the STS data, is expected to behave differently than the dispersion of electron focusing patterns.
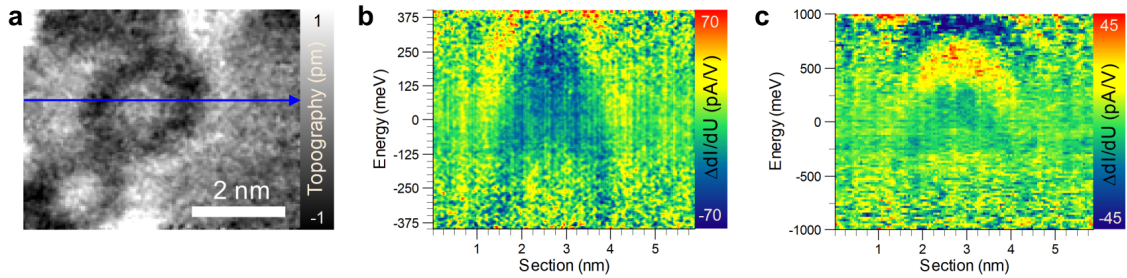

Figure A.1: Surface pattern in Cu(100) not originating from a single subsurface impurity. (a) Topography ($U = -300\,\mathrm{mV}/I = 0.4\,\mathrm{nA}$). (b,c) Spectroscopic sections along [010] direction for $U_{\mathrm{Set}} = -400\,\mathrm{mV}$ and $U_{\mathrm{Set}} = -1\,\mathrm{V}$, respectively.

The detection of many-body effects in spectroscopy data, as discussed in Sec. 6.4, is most sensitive to experimental resolution and, thus, tip quality. If strong noise interferes with the measurement, possibly only the main features are visible, e.g. the minima/maxima with overall dispersion, but the small features due to renormalization around the Fermi level are not resolved. If the signal is weak and data processing thorough, additional filters applied to the data can hide the features of a small energy range. The Ge 3ML data set shown in Fig. A.2 illustrates this behavior. While the topography and the spectroscopic data allow for a determination of the impurity depth, the signal around the Fermi level is too low in order to resolve clearly a bending as expected from electron-phonon coupling. The two data sets in Fig. A.2(d) and (e) were recorded consecutively, showing the general reproducibility of the measurement. Even if the data do not clearly confirm many-body effects, since tentative features might be identified, they do not contradict such findings either. Regardless, the overall shape, including the peak in the center becoming weaker, is reproduced by the corresponding tight-binding simulations, presented with and without self-energy for comparison. The experimental patterns show a stronger lateral weight on the outer maximum at around $x = 6\,\mathrm{Å}$ than the simulations. This can be linked to weak atomic resolution, which is found in the Fourier analysis and filtered image in Fig. A.2(b,c). This way, the tip shape adds an additional component
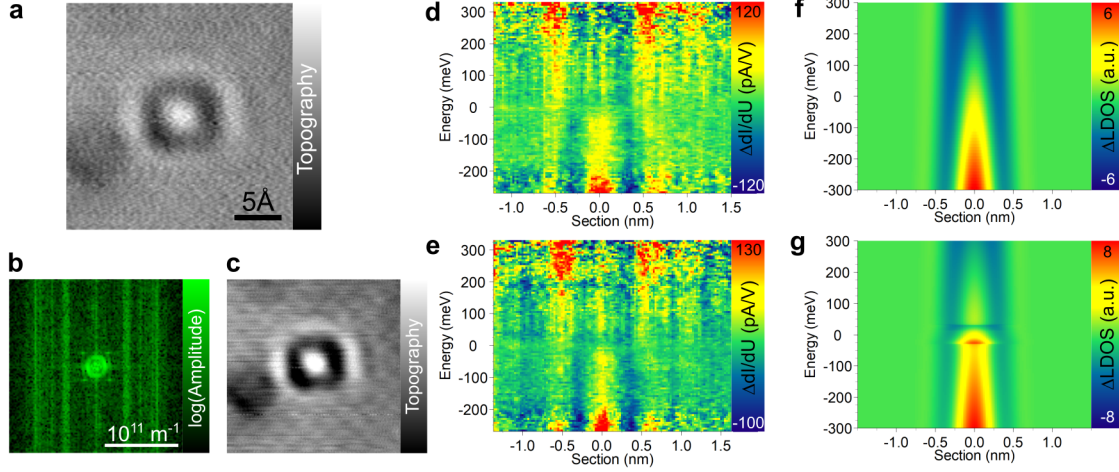
Figure A.2: Surface signature of Ge 3ML impurity. (a) Topography ($U = -25\,\mathrm{mV}/I = 0.5\,\mathrm{nA}$). (b) Fourier spectrum of (a), clearly indicating four-fold lattice periodicity. (c) Fourier-filtered topography (a) showing atomic resolution. (d,e) Spectroscopic sections recorded directly consecutively ($U_{\mathrm{Set}} = 325\,\mathrm{mV}/I = 0.4\,\mathrm{nA}$) with only tentative indications of characteristic bending at Fermi level. (f,g) Tight-binding simulations without and with electron-phonon coupling ($\lambda = 5.0, \hbar\omega_D = 30\,\mathrm{meV}$), respectively.

that has to be considered in the interpretation of the pattern.

Finally, we will briefly discuss the consequences of the tip's orbital properties. Previously, we examined the role of different electronic orbitals for the impurity scattering, the bulk propagation, and the resulting electron focusing pattern. We found that the experimental patterns for Ge impurities are mostly given by d electrons, while a significant contribution with sp character is missing despite being predicted by the ab-initio calculations. In the experiment, we use a tungsten tip covered with layers of Cu and, as discussed in Sec. 2.2.2, it images the LDOS mostly by a d_z^2 orbital which allows for atomic resolution. It could be conjectured that this leads to a preference of the transition matrix element for certain d-states over sp-states, which could cause the observed effects for Ge. However, even if we assume that the d-type components are mapped excessively, the high topographic contrast of the sp features as predicted in the calculations should be found in the experiment because of its amplitude (10 times stronger than d) and the longer decay length into the vacuum for s and p states with respect to d states. Consequently, we have no reason to assume orbital-sensitive imaging due to the tip.

Bibliography

[1] D. Shoenberg, *Magnetic Oscillations in Metals*, Cambridge Monographs on Physics (Cambridge University Press, Cambridge, 1984).

[2] S. Hüfner, *Very High Resolution Photoelectron Spectroscopy*, Lecture Notes in Physics (Springer, Berlin Heidelberg, 2007).

[3] M. F. Crommie, C. P. Lutz, and D. M. Eigler, "Imaging standing waves in a two-dimensional electron gas", *Nature* **363**, 524 (1993).

[4] Y. Hasegawa and P. Avouris, "Direct observation of standing wave formation at surface steps using scanning tunneling spectroscopy", *Phys. Rev. Lett.* **71**, 1071–1074 (1993).

[5] J. Friedel, "XIV. The distribution of electrons round impurities in monovalent metals", *London, Edinburgh, Dublin Philos. Mag. J. Sci.* **43**, 153–189 (1952).

[6] J. E. Hoffman, K. McElroy, D.-H. Lee, K. M. Lang, H. Eisaki, S. Uchida, and J. C. Davis, "Imaging Quasiparticle Interference in $Bi_2Sr_2CaCu_2O_{8+\delta}$", *Science* **297**, 1148–1151 (2002).

[7] T. Valla, A. V. Fedorov, P. D. Johnson, and S. L. Hulbert, "Many-Body Effects in Angle-Resolved Photoemission: Quasiparticle Energy and Lifetime of a Mo(110) Surface State", *Phys. Rev. Lett.* **83**, 2085–2088 (1999).

[8] B. A. McDougall, T. Balasubramanian, and E. Jensen, "Phonon contribution to quasiparticle lifetimes in Cu measured by angle-resolved photoemission", *Phys. Rev. B* **51**, 13891–13894 (1995).

[9] J. Shi, S.-J. Tang, B. Wu, P. T. Sprunger, W. L. Yang, V. Brouet, X. J. Zhou, Z. Hussain, Z.-X. Shen, Z. Zhang, and E. W. Plummer, "Direct Extraction of the Eliashberg Function for Electron-Phonon Coupling: A Case Study of $Be(10\bar{1}0)$", *Phys. Rev. Lett.* **92**, 186401 (2004).

[10] J. Li, W.-D. Schneider, R. Berndt, O. R. Bryant, and S. Crampin, "Surface-State Lifetime Measured by Scanning Tunneling Spectroscopy", *Phys. Rev. Lett.* **81**, 4464–4467 (1998).

[11] L. Bürgi, O. Jeandupeux, H. Brune, and K. Kern, "Probing Hot-Electron Dynamics at Surfaces with a Cold Scanning Tunneling Microscope", *Phys. Rev. Lett.* **82**, 4516–4519 (1999).

[12] J. Kliewer, R. Berndt, E. V. Chulkov, V. M. Silkin, P. M. Echenique, and S. Crampin, "Dimensionality Effects in the Lifetime of Surface States", *Science* **288**, 1399–1402 (2000).

[13] M. Schackert, T. Märkl, J. Jandke, M. Hölzer, S. Ostanin, E. K. U. Gross, A. Ernst, and W. Wulfhekel, "Local Measurement of the Eliashberg Function of Pb Islands: Enhancement of Electron-Phonon Coupling by Quantum Well States", *Phys. Rev. Lett.* **114**, 047002 (2015).

[14] H. Osterhage, R. Wiesendanger, and S. Krause, "Phonon-mediated tunneling into a two-dimensional electron gas on the Be(0001) surface", *Phys. Rev. B* **103**, 155428 (2021).

[15] G. Li, A. Luican, and E. Y. Andrei, "Scanning Tunneling Spectroscopy of Graphene on Graphite", *Phys. Rev. Lett.* **102**, 176804 (2009).

[16] I. Zeljkovic, K. L. Scipioni, D. Walkup, Y. Okada, W. Zhou, R. Sankar, G. Chang, Y. J. Wang, H. Lin, A. Bansil, F. Chou, Z. Wang, and V. Madhavan, "Nanoscale determination of the mass enhancement factor in the lightly doped bulk insulator lead selenide", *Nat. Commun.* **6**, 6559 (2015).

[17] S. Grothe, S. Johnston, S. Chi, P. Dosanjh, S. A. Burke, and Y. Pennec, "Quantifying Many-Body Effects by High-Resolution Fourier Transform Scanning Tunneling Spectroscopy", *Phys. Rev. Lett.* **111**, 246804 (2013).

[18] G. A. Fiete, J. S. Hersch, E. J. Heller, H. C. Manoharan, C. P. Lutz, and D. M. Eigler, "Scattering Theory of Kondo Mirages and Observation of Single Kondo Atom Phase Shift", *Phys. Rev. Lett.* **86**, 2392–2395 (2001).

[19] M. A. Schneider, L. Vitali, N. Knorr, and K. Kern, "Observing the scattering phase shift of isolated Kondo impurities at surfaces", *Phys. Rev. B* **65**, 121406 (2002).

[20] A. Weismann, M. Wenderoth, S. Lounis, P. Zahn, N. Quaas, R. G. Ulbrich, P. H. Dederichs, and S. Blügel, "Seeing the Fermi Surface in Real Space by Nanoscale Electron Focusing", *Science* **323**, 1190–1193 (2009).

[21] M. Ruby, B. W. Heinrich, J. I. Pascual, and K. J. Franke, "Experimental Demonstration of a Two-Band Superconducting State for Lead Using Scanning Tunneling Spectroscopy", *Phys. Rev. Lett.* **114**, 157001 (2015).

[22] H. Prüser, M. Wenderoth, P. E. Dargel, A. Weismann, R. Peters, T. Pruschke, and R. G. Ulbrich, "Long-range Kondo signature of a single magnetic impurity", *Nat. Phys.* **7**, 203–206 (2011).

[23] H. Prüser, M. Wenderoth, A. Weismann, and R. G. Ulbrich, "Mapping Itinerant Electrons around Kondo Impurities", *Phys. Rev. Lett.* **108**, 166604 (2012).

[24] H. Prüser, P. E. Dargel, M. Bouhassoune, R. G. Ulbrich, T. Pruschke, S. Lounis, and M. Wenderoth, "Interplay between the Kondo effect and the Ruderman–Kittel–Kasuya–Yosida interaction", *Nat. Commun.* **5**, 5417 (2014).

[25] J. O. Linde, "Elektrische Eigenschaften verdünnter Mischkristallegierungen III. Widerstand von Kupfer- und Goldlegierungen. Gesetzmäßigkeiten der Widerstandserhöhungen", *Annalen der Physik* **407**, 219–248 (1932).

[26] G. Binnig, H. Rohrer, C. Gerber, and E. Weibel, "Surface Studies by Scanning Tunneling Microscopy", *Phys. Rev. Lett.* **49**, 57–61 (1982).

[27] G. Binnig, H. Rohrer, C. Gerber, and E. Weibel, "7×7 Reconstruction on Si(111) Resolved in Real Space", *Phys. Rev. Lett.* **50**, 120–123 (1983).

[28] B. C. Stipe, M. A. Rezaei, and W. Ho, "Single-Molecule Vibrational Spectroscopy and Microscopy", *Science* **280**, 1732–1735 (1998).

[29] R. Wiesendanger, "Spin mapping at the nanoscale and atomic scale", *Rev. Mod. Phys.* **81**, 1495–1550 (2009).

[30] A. J. Heinrich, J. A. Gupta, C. P. Lutz, and D. M. Eigler, "Single-Atom Spin-Flip Spectroscopy", *Science* **306**, 466–469 (2004).

[31] S. Loth, M. Etzkorn, C. P. Lutz, D. M. Eigler, and A. J. Heinrich, "Measurement of Fast Electron Spin Relaxation Times with Atomic Resolution", *Science* **329**, 1628–1630 (2010).

[32] S. Baumann, W. Paul, T. Choi, C. P. Lutz, A. Ardavan, and A. J. Heinrich, "Electron paramagnetic resonance of individual atoms on a surface", *Science* **350**, 417–420 (2015).

[33] S. Yoshida, Y. Aizawa, Z.-h. Wang, R. Oshima, Y. Mera, E. Matsuyama, H. Oigawa, O. Takeuchi, and H. Shigekawa, "Probing ultrafast spin dynamics with optical pump–probe scanning tunnelling microscopy", *Nat. Nanotechnol.* **9**, 588–593 (2014).

[34] P. Kloth, K. Kaiser, and M. Wenderoth, "Controlling the screening process of a nanoscaled space charge region by minority carriers", *Nat. Commun.* **7**, 10108 (2016).

[35] R. Gutzler, M. Garg, C. R. Ast, K. Kuhnke, and K. Kern, "Light–matter interaction at atomic scales", *Nat. Rev. Phys.* **3**, 441–453 (2021).

[36] P. Muralt and D. W. Pohl, "Scanning tunneling potentiometry", *Appl. Phys. Lett.* **48**, 514–516 (1986).

[37] J. Homoth, "Das elektrochemische Potential auf der atomaren Skala: Untersuchung des Ladungstransports eines stromtragenden zweidimensionalen Elektronengases mit Hilfe der Raster-Tunnel-Potentiometrie", PhD Thesis (Georg-August-Universität Göttingen, Göttingen, 2008).

[38] T. Druga, M. Wenderoth, J. Homoth, M. A. Schneider, and R. G. Ulbrich, "A versatile high resolution scanning tunneling potentiometry implementation", *Rev. Sci. Instrum.* **81**, 083704 (2010).

[39] T. Kotzott, "Magnetotransport in Graphene on the Atomic Scale", Master's Thesis (Georg-August-Universität Göttingen, Göttingen, 2015).

[40] P. Willke, T. Kotzott, T. Pruschke, and M. Wenderoth, "Magnetotransport on the nano scale", *Nat. Commun.* **8**, 15283 (2017).

Bibliography

[41] A. Sinterhauf, G. A. Traeger, D. M. Pakdehi, P. Schädlich, P. Willke, F. Speck, T. Seyller, C. Tegenkamp, K. Pierz, H. W. Schumacher, and M. Wenderoth, "Substrate induced nanoscale resistance variation in epitaxial graphene", *Nat. Commun.* **11**, 1–9 (2020).

[42] G. Binnig, C. F. Quate, and C. Gerber, "Atomic Force Microscope", *Phys. Rev. Lett.* **56**, 930–933 (1986).

[43] C. J. Chen, *Introduction to Scanning Tunneling Microscopy*, 2nd ed. (Oxford University Press, Oxford New York, 2007).

[44] D. Bonnell, *Scanning Probe Microscopy and Spectroscopy: Theory, Techniques, and Applications*, 2nd ed. (John Wiley & Sons, New York, 2001).

[45] E. Meyer, H. J. Hug, and R. Bennewitz, *Scanning Probe Microscopy* (Springer, Berlin Heidelberg, 2004).

[46] J. Bardeen, "Tunnelling from a Many-Particle Point of View", *Phys. Rev. Lett.* **6**, 57–59 (1961).

[47] J. Tersoff and D. R. Hamann, "Theory and Application for the Scanning Tunneling Microscope", *Phys. Rev. Lett.* **50**, 1998–2001 (1983).

[48] R. J. Hamers, "Atomic-Resolution Surface Spectroscopy with the Scanning Tunneling Microscope", *Annu. Rev. Phys. Chem.* **40**, 531–559 (1989).

[49] M. E. Straumanis and L. S. Yu, "Lattice parameters, densities, expansion coefficients and perfection of structure of Cu and of Cu–In α phase", *Acta Crystallogr. A* **25**, 676–682 (1969).

[50] C. J. Chen, "Tunneling matrix elements in three-dimensional space: The derivative rule and the sum rule", *Phys. Rev. B* **42**, 8841–8857 (1990).

[51] A. Baratoff, "Theory of scanning tunneling microscopy — methods and approximations", *Physica B+C* **127**, 143–150 (1984).

[52] C. J. Chen, "Origin of atomic resolution on metal surfaces in scanning tunneling microscopy", *Phys. Rev. Lett.* **65**, 448–451 (1990).

[53] L. Gross, N. Moll, F. Mohn, A. Curioni, G. Meyer, F. Hanke, and M. Persson, "High-Resolution Molecular Orbital Imaging Using a p-Wave STM Tip", *Phys. Rev. Lett.* **107**, 086101 (2011).

[54] J. Repp, G. Meyer, S. M. Stojković, A. Gourdon, and C. Joachim, "Molecules on insulating films: scanning-tunneling microscopy imaging of individual molecular orbitals", *Phys. Rev. Lett.* **94**, 026803 (2005).

[55] C. J. Chen, "Effects of $m{\neq}0$ tip states in scanning tunneling microscopy: The explanations of corrugation reversal", *Phys. Rev. Lett.* **69**, 1656–1659 (1992).

[56] F. Lüpke, S. Manni, S. C. Erwin, I. I. Mazin, P. Gegenwart, and M. Wenderoth, "Highly unconventional surface reconstruction of Na_2IrO_3 with persistent energy gap", *Phys. Rev. B* **91**, 041405 (2015).

[57] R. M. Feenstra, J. A. Stroscio, and A. P. Fein, "Tunneling spectroscopy of the Si(111) 2×1 surface", *Surface Science* **181**, 295–306 (1987).

[58] J. A. Stroscio, R. M. Feenstra, and A. P. Fein, "Electronic Structure of the Si(111) 2×1 Surface by Scanning-Tunneling Microscopy", *Phys. Rev. Lett.* **57**, 2579–2582 (1986).

[59] H. Prüser, "Scanning tunneling spectroscopy of magnetic bulk impurities: From a single Kondo atom towards a coupled system", PhD Thesis (Georg-August-Universität Göttingen, Göttingen, 2013).

[60] T. Eggebrecht, "Enwicklung eines Lock-In-Verfahrens zur hochauflösenden Rastertunnelmikroskopie", Bachelor's Thesis (Georg-August-Universität Göttingen, Göttingen, 2010).

[61] R. Smoluchowski, "Anisotropy of the Electronic Work Function of Metals", *Phys. Rev.* **60**, 661–674 (1941).

[62] J. K. Garleff, M. Wenderoth, K. Sauthoff, R. G. Ulbrich, and M. Rohlfing, "2×1 reconstructed Si(111) surface: STM experiments versus ab initio calculations", *Phys. Rev. B* **70**, 245424 (2004).

[63] K. Besocke, "An easily operable scanning tunneling microscope", *Surf. Sci.* **181**, 145–153 (1987).

[64] K. Sauthoff, "Rastertunnelspektroskopie an einzelnen Donatoren und Donatorkomplexen nahe der GaAs(110)-Oberfläche", PhD thesis (Georg-August-Universität Göttingen, Göttingen, 2003).

[65] H. Schleiermacher, "Characterization of tips for scanning tunneling microscopy", Diploma Thesis (Georg-August-Universität Göttingen, Göttingen, 2006).

[66] N. W. Ashcroft and N. D. Mermin, *Festkörperphysik*, 3rd ed. (Oldenbourg Verlag, München, 2007).

[67] R. Gross and A. Marx, *Festkörperphysik*, 2nd ed. (De Gruyter Oldenbourg, München, 2014).

[68] J. Lindhard, "On the properties of a gas of charged particles", *Danske Matematisk-fysiske Meddeleiser* **28**, 1–57 (1954).

[69] M. F. Crommie, C. P. Lutz, and D. M. Eigler, "Confinement of Electrons to Quantum Corrals on a Metal Surface", *Science* **262**, 218–220 (1993).

[70] E. J. Heller, M. F. Crommie, C. P. Lutz, and D. M. Eigler, "Scattering and absorption of surface electron waves in quantum corrals", *Nature* **369**, 464–466 (1994).

[71] P. Avouris and I.-W. Lyo, "Observation of Quantum-Size Effects at Room Temperature on Metal Surfaces With STM", *Science* **264**, 942–945 (1994).

[72] H. C. Manoharan, C. P. Lutz, and D. M. Eigler, "Quantum mirages formed by coherent projection of electronic structure", *Nature* **403**, 512–515 (2000).

[73] L. Bürgi, N. Knorr, H. Brune, M. A. Schneider, and K. Kern, "Two-dimensional electron gas at noble-metal surfaces", *Appl. Phys. A* **75**, 141–145 (2002).

[74] L. Simon, C. Bena, F. Vonau, M. Cranney, and D. Aubel, "Fourier-transform scanning tunnelling spectroscopy: the possibility to obtain constant-energy maps and band dispersion using a local measurement", *J. Phys. D: Appl. Phys.* **44**, 464010 (2011).

[75] J. E. Hoffman, "Spectroscopic scanning tunneling microscopy insights into Fe-based superconductors", *Rep. Prog. Phys.* **74**, 124513 (2011).

[76] C. Bena, "Friedel oscillations: Decoding the hidden physics", *Comptes Rendus Physique* **17**, 302–321 (2016).

[77] J. Li, W.-D. Schneider, and R. Berndt, "Local density of states from spectroscopic scanning-tunneling-microscope images: Ag(111)", *Phys. Rev. B* **56**, 7656–7659 (1997).

[78] L. Bürgi, L. Petersen, H. Brune, and K. Kern, "Noble metal surface states: deviations from parabolic dispersion", *Surf. Sci.* **447**, L157–L161 (2000).

[79] O. Jeandupeux, L. Bürgi, A. Hirstein, H. Brune, and K. Kern, "Thermal damping of quantum interference patterns of surface-state electrons", *Phys. Rev. B* **59**, 15926–15934 (1999).

[80] L. Bürgi, H. Brune, O. Jeandupeux, and K. Kern, "Quantum coherence and lifetimes of surface-state electrons", *J Electron Spectros Relat Phenomena* **109**, 33–49 (2000).

[81] L. Bürgi, H. Brune, and K. Kern, "Imaging of Electron Potential Landscapes on Au(111)", *Phys. Rev. Lett.* **89**, 176801 (2002).

[82] P. T. Sprunger, L. Petersen, E. W. Plummer, E. Lægsgaard, and F. Besenbacher, "Giant Friedel Oscillations on the Beryllium(0001) Surface", *Science* **275**, 1764–1767 (1997).

[83] L. Petersen, P. T. Sprunger, P. Hofmann, E. Lægsgaard, B. G. Briner, M. Doering, H.-P. Rust, A. M. Bradshaw, F. Besenbacher, and E. W. Plummer, "Direct imaging of the two-dimensional Fermi contour: Fourier-transform STM", *Phys. Rev. B* **57**, R6858–R6861 (1998).

[84] K. McElroy, R. W. Simmonds, J. E. Hoffman, D.-H. Lee, J. Orenstein, H. Eisaki, S. Uchida, and J. C. Davis, "Relating atomic-scale electronic phenomena to wave-like quasiparticle states in superconducting $Bi_2Sr_2CaCu_2O_{8+\delta}$", *Nature* **422**, 592–596 (2003).

[85] F. Vonau, D. Aubel, G. Gewinner, C. Pirri, J. C. Peruchetti, D. Bolmont, and L. Simon, "Fermi contour imaging of the two-dimensional semimetal $ErSi_2$ by Fourier transform STM", *Phys. Rev. B* **69**, 081305 (2004).

[86] F. Vonau, D. Aubel, G. Gewinner, S. Zabrocki, J. C. Peruchetti, D. Bolmont, and L. Simon, "Evidence of Hole-Electron Quasiparticle Interference in ErSi$_2$ Semimetal by Fourier-Transform Scanning Tunneling Spectroscopy", *Phys. Rev. Lett.* **95**, 176803 (2005).

[87] J. I. Pascual, G. Bihlmayer, Y. M. Koroteev, H.-P. Rust, G. Ceballos, M. Hansmann, K. Horn, E. V. Chulkov, S. Blügel, P. M. Echenique, and P. Hofmann, "Role of Spin in Quasiparticle Interference", *Phys. Rev. Lett.* **93**, 196802 (2004).

[88] P. Roushan, J. Seo, C. V. Parker, Y. S. Hor, D. Hsieh, D. Qian, A. Richardella, M. Z. Hasan, R. J. Cava, and A. Yazdani, "Topological surface states protected from backscattering by chiral spin texture", *Nature* **460**, 1106–1109 (2009).

[89] Z. Alpichshev, J. G. Analytis, J.-H. Chu, I. R. Fisher, Y. L. Chen, Z. X. Shen, A. Fang, and A. Kapitulnik, "STM Imaging of Electronic Waves on the Surface of Bi$_2$Te$_3$: Topologically Protected Surface States and Hexagonal Warping Effects", *Phys. Rev. Lett.* **104**, 016401 (2010).

[90] L. Chen, P. Cheng, and K. Wu, "Quasiparticle interference in unconventional 2D systems", *J. Phys.: Condens. Matter* **29**, 103001 (2017).

[91] P. Mallet, I. Brihuega, V. Cherkez, J. M. Gómez-Rodríguez, and J.-Y. Veuillen, "Friedel oscillations in graphene-based systems probed by Scanning Tunneling Microscopy", *Comptes Rendus Physique* **17**, 294–301 (2016).

[92] J. Tesch, "Local electronic properties of epitaxial graphene nanoflakes on metals and semiconductors", PhD Thesis (Universität Konstanz, Konstanz, 2018).

[93] P. Hofmann, B. G. Briner, M. Doering, H.-P. Rust, E. W. Plummer, and A. M. Bradshaw, "Anisotropic Two-Dimensional Friedel Oscillations", *Phys. Rev. Lett.* **79**, 265–268 (1997).

[94] E. Wahlström, I. Ekvall, H. Olin, and L. Walldén, "Long-range interaction between adatoms at the Cu(111) surface imaged by scanning tunnelling microscopy", *Appl. Phys. A* **66**, 1107–1110 (1998).

[95] J. Repp, F. Moresco, G. Meyer, K.-H. Rieder, P. Hyldgaard, and M. Persson, "Substrate Mediated Long-Range Oscillatory Interaction between Adatoms: Cu/Cu(111)", *Phys. Rev. Lett.* **85**, 2981–2984 (2000).

[96] N. Knorr, H. Brune, M. Epple, A. Hirstein, M. A. Schneider, and K. Kern, "Long-range adsorbate interactions mediated by a two-dimensional electron gas", *Phys. Rev. B* **65**, 115420 (2002).

[97] M. Leisegang, J. Kügel, L. Klein, and M. Bode, "Analyzing the Wave Nature of Hot Electrons with a Molecular Nanoprobe", *Nano Lett.* **18**, 2165–2171 (2018).

[98] J. Kügel, M. Leisegang, M. Böhme, A. Krönlein, A. Sixta, and M. Bode, "Remote Single-Molecule Switching: Identification and Nanoengineering of Hot Electron-Induced Tautomerization", *Nano Lett.* **17**, 5106–5112 (2017).

[99] J. Li, W.-D. Schneider, R. Berndt, and B. Delley, "Kondo Scattering Observed at a Single Magnetic Impurity", *Phys. Rev. Lett.* **80**, 2893–2896 (1998).

[100] V. Madhavan, W. Chen, T. Jamneala, M. F. Crommie, and N. S. Wingreen, "Tunneling into a Single Magnetic Atom: Spectroscopic Evidence of the Kondo Resonance", *Science* **280**, 567–569 (1998).

[101] N. Knorr, M. A. Schneider, L. Diekhöner, P. Wahl, and K. Kern, "Kondo Effect of Single Co Adatoms on Cu Surfaces", *Phys. Rev. Lett.* **88**, 096804 (2002).

[102] N. Quaas, M. Wenderoth, A. Weismann, R. G. Ulbrich, and K. Schönhammer, "Kondo resonance of single Co atoms embedded in Cu(111)", *Phys. Rev. B* **69**, 201103 (2004).

[103] S. Lounis, P. Mavropoulos, P. H. Dederichs, and S. Blügel, "Surface-state scattering by adatoms on noble metals: Ab initio calculations using the Korringa-Kohn-Rostoker Green function method", *Phys. Rev. B* **73**, 195421 (2006).

[104] M. Ternes, A. J. Heinrich, and W.-D. Schneider, "Spectroscopic manifestations of the Kondo effect on single adatoms", *J. Phys.: Condens. Matter* **21**, 053001 (2008).

[105] J. Bouaziz, F. S. Mendes Guimarães, and S. Lounis, "A new view on the origin of zero-bias anomalies of Co atoms atop noble metal surfaces", *Nat. Commun.* **11**, 6112 (2020).

[106] S. Crampin, "Surface states as probes of buried impurities", *Journal of Physics: Condensed Matter* **6**, L613 (1994).

[107] L. Petersen, P. Laitenberger, E. Lægsgaard, and F. Besenbacher, "Screening waves from steps and defects on Cu(111) and Au(111) imaged with STM: Contribution from bulk electrons", *Phys. Rev. B* **58**, 7361–7366 (1998).

[108] L. Petersen, P. Hofmann, E. W. Plummer, and F. Besenbacher, "Fourier Transform–STM: determining the surface Fermi contour", *J Electron Spectros Relat Phenomena* **109**, 97–115 (2000).

[109] J. I. Pascual, A. Dick, M. Hansmann, H.-P. Rust, J. Neugebauer, and K. Horn, "Bulk Electronic Structure of Metals Resolved with Scanning Tunneling Microscopy", *Phys. Rev. Lett.* **96**, 046801 (2006).

[110] C. A. Marques, M. S. Bahramy, C. Trainer, I. Marković, M. D. Watson, F. Mazzola, A. Rajan, T. D. Raub, P. D. C. King, and P. Wahl, "Tomographic mapping of the hidden dimension in quasi-particle interference", *arXiv:2103.09282 [cond-mat]* (2021).

[111] J. A. Kubby and W. J. Greene, "Electron interferometry at a metal-semiconductor interface", *Phys. Rev. Lett.* **68**, 329–332 (1992).

[112] G. Hörmandinger and J. B. Pendry, "Quantum well resonances in scanning tunneling microscopy", *Surf. Sci.* **295**, 34–42 (1993).

[113] I. B. Altfeder, K. A. Matveev, and D. M. Chen, "Electron Fringes on a Quantum Wedge", *Phys. Rev. Lett.* **78**, 2815–2818 (1997).

[114] I. B. Altfeder, D. M. Chen, and K. A. Matveev, "Imaging Buried Interfacial Lattices with Quantized Electrons", *Phys. Rev. Lett.* **80**, 4895–4898 (1998).

[115] I. B. Altfeder, V. Narayanamurti, and D. M. Chen, "Imaging Subsurface Reflection Phase with Quantized Electrons", *Phys. Rev. Lett.* **88**, 206801 (2002).

[116] P. Kloth, M. Wenderoth, P. Willke, H. Prüser, and R. G. Ulbrich, "Quantum well states with nonvanishing parallel momentum in Cu/Co/Cu(100)", *Phys. Rev. B* **89**, 125412 (2014).

[117] M. Schmid, W. Hebenstreit, P. Varga, and S. Crampin, "Quantum Wells and Electron Interference Phenomena in Al due to Subsurface Noble Gas Bubbles", *Phys. Rev. Lett.* **76**, 2298–2301 (1996).

[118] F. J. Garcia-Vidal, P. L. de Andres, and F. Flores, "Elastic Scattering and the Lateral Resolution of Ballistic Electron Emission Microscopy: Focusing Effects on the Au/Si Interface", *Phys. Rev. Lett.* **76**, 807–810 (1996).

[119] J. Heil, M. Primke, K. U. Würz, and P. Wyder, "Real Space Imaging of Ballistic Carrier Propagation in Bi Single Crystals", *Phys. Rev. Lett.* **74**, 146–149 (1995).

[120] J. Heil, M. Primke, A. Böhm, P. Wyder, B. Wolf, J. Major, and P. Keppler, "Electron focusing in Ag and W single crystals", *Phys. Rev. B* **54**, R2280–R2283 (1996).

[121] J. Heil, A. Böhm, A. Gröger, M. Primke, P. Wyder, P. Keppler, J. Major, H. Bender, E. Schönherr, H. Wendel, B. Wolf, K. U. Würz, W. Grill, H. Herrnberger, S. Knauth, and J. Lenzner, "Electron focusing in metals and semimetals", *Physics Reports* **323**, 387–455 (2000).

[122] O. Kurnosikov, D. V. Kulikov, V. S. Kharlamov, H. J. M. Swagten, and Y. V. Trushin, "Temperature-induced evolution of subsurface nanocavities in argon-implanted copper", *Phys. Rev. B* **84**, 054109 (2011).

[123] D. V. Kulikov, O. Kurnosikov, V. S. Kharlamov, and Y. V. Trushin, "Evolution of subsurface nanocavities in copper under argon bombardment and annealing", *Appl. Surf. Sci.* **267**, 128–131 (2013).

[124] O. Kurnosikov, O. A. O. Adam, H. J. M. Swagten, W. J. M. de Jonge, and B. Koopmans, "Probing quantum wells induced above a subsurface nanocavity in copper", *Phys. Rev. B* **77**, 125429 (2008).

[125] O. Kurnosikov, J. H. Nietsch, M. Sicot, H. J. M. Swagten, and B. Koopmans, "Long-Range Electron Interferences at a Metal Surface Induced by Buried Nanocavities", *Phys. Rev. Lett.* **102**, 066101 (2009).

[126] O. Kurnosikov, H. J. M. Swagten, and B. Koopmans, "Internal Electron Diffraction from Atomically Ordered Subsurface Nanostructures in Metals", *Phys. Rev. Lett.* **106**, 196803 (2011).

[127] T. Siahaan, O. Kurnosikov, H. J. M. Swagten, and B. Koopmans, "Direct epitaxial growth of subsurface Co nanoclusters", *Phys. Rev. B* **90**, 165419 (2014).

[128] T. Siahaan, O. Kurnosikov, H. J. M. Swagten, B. Koopmans, S. V. Kolesnikov, A. M. Saletsky, and A. L. Klavsyuk, "Co diffusion in the near-surface region of Cu", *Phys. Rev. B* **94**, 195435 (2016).

[129] C. Sprodowski and K. Morgenstern, "Three types of bulk impurity induced interference patterns on the (100) and (111) faces of Ne- and Ar-doped silver", *Phys. Rev. B* **82**, 165444 (2010).

[130] S. Lounis, P. Zahn, A. Weismann, M. Wenderoth, R. G. Ulbrich, I. Mertig, P. H. Dederichs, and S. Blügel, "Theory of real space imaging of Fermi surface parts", *Phys. Rev. B* **83**, 035427 (2011).

[131] K. Kobayashi, "Scattering theory of subsurface impurities observed in scanning tunneling microscopy", *Phys. Rev. B* **54**, 17029–17038 (1996).

[132] Y. S. Avotina, Y. A. Kolesnichenko, and J. M. van Ruitenbeek, "Theory of oscillations in STM conductance caused by subsurface defects", *Low Temp. Phys.* **36**, 849–864 (2010).

[133] M. Bouhassoune, B. Zimmermann, P. Mavropoulos, D. Wortmann, P. H. Dederichs, S. Blügel, and S. Lounis, "Quantum well states and amplified spin-dependent Friedel oscillations in thin films", *Nat. Commun.* **5**, 5558 (2014).

[134] A. Weismann, "Scanning Tunnelling Spectroscopy of Subsurface Magnetic Atoms in Copper – Electron Focusing and Kondo Effect", PhD Thesis (Georg-August-Universität Göttingen, Göttingen, 2008).

[135] G. D. Mahan, *Many-Particle Physics*, 3rd ed. (Kluwer Academic/Plenum Publishers, New York, 2000).

[136] R. D. Mattuck, *A Guide to Feynman Diagrams in the Many-Body Problem*, 2nd ed. (Dover, New York, 1992).

[137] A. Gonis and W. H. Butler, *Multiple Scattering in Solids*, Graduate Texts in Contemporary Physics (Springer, New York, 2000).

[138] E. N. Economou, *Green's Functions in Quantum Physics*, 3rd ed., Springer Series in Solid-State Sciences (Springer, Berlin Heidelberg, 2006).

[139] G. Stefanucci and R. van Leeuwen, *Nonequilibrium Many-Body Theory of Quantum Systems: A Modern Introduction* (Cambridge University Press, Cambridge, 2013).

[140] P. Mavropoulos and N. Papanikolaou, "The Korringa-Kohn-Rostoker (KKR) Green Function Method - I. Electronic Structure of Periodic Systems", in *Computational Nanoscience: Do it Yourself! Winter School, 14 - 22 February 2006, Forschungszentrum Jülich, Germany - Lecture Notes*, edited by J. Grotendorst, S. Blügel, and D. Marx, NIC Series 31 (FZJ, John von Neumann Institute for Computing, Jülich, 2006).

[141] J. C. Slater and G. F. Koster, "Simplified LCAO Method for the Periodic Potential Problem", *Phys. Rev.* **94**, 1498–1524 (1954).

[142] J. C. Slater, "Interaction of Waves in Crystals", *Rev. Mod. Phys.* **30**, 197–222 (1958).

[143] D. Papaconstantopoulos, *Handbook of the band structure of elemental solids* (Plenum Press, New York, 1986).

[144] H. A. Kramers, "La diffusion de la lumière par les atomes", *Atti del Congresso Internationale dei Fisici, Como* **2**, 545–557 (1927).

[145] R. d. L. Kronig, "On the Theory of Dispersion of X-Rays", *J. Opt. Soc. Am.* **12**, 547–557 (1926).

[146] E. V. Chulkov, V. M. Silkin, and P. M. Echenique, "Image potential states on metal surfaces: binding energies and wave functions", *Surf. Sci.* **437**, 330–352 (1999).

[147] D. P. Woodruff, S. L. Hulbert, P. D. Johnson, and N. V. Smith, "Unoccupied surface resonance on Cu(100) and the effect of vacuum-level pinning", *Phys. Rev. B* **31**, 4046–4048 (1985).

[148] M. Mehta-Ajmani, I. P. Batra, E. E. Lafon, and C. S. Fadley, "Extended tight-binding calculations of bulk copper and (001) Cu film", *J. Phys. C: Solid State Phys.* **13**, 2807–2816 (1980).

[149] I. Mertig, "Transport properties of dilute alloys", *Rep. Prog. Phys.* **62**, 237–276 (1999).

[150] J. I. Mustafa, M. Bernardi, J. B. Neaton, and S. G. Louie, "Ab initio electronic relaxation times and transport in noble metals", *Phys. Rev. B* **94**, 155105 (2016).

[151] S. H. Vosko, L. Wilk, and M. Nusair, "Accurate spin-dependent electron liquid correlation energies for local spin density calculations: a critical analysis", *Can. J. Phys.* **58**, 1200–1211 (1980).

[152] N. Papanikolaou, R. Zeller, and P. H. Dederichs, "Conceptual improvements of the KKR method", *J. Phys.: Condens. Matter* **14**, 2799–2823 (2002).

[153] J. Korringa, "On the calculation of the energy of a Bloch wave in a metal", *Physica* **13**, 392–400 (1947).

[154] W. Kohn and N. Rostoker, "Solution of the Schrödinger Equation in Periodic Lattices with an Application to Metallic Lithium", *Phys. Rev.* **94**, 1111–1120 (1954).

[155] R. Zeller and P. H. Dederichs, "Electronic structure of impurities in Cu, calculated self-consistently by Korringa-Kohn-Rostoker Green's-function method", *Phys. Rev. Lett.* **42**, 1713 (1979).

[156] S. Lounis, "Theory of magnetic transition metal nanoclusters on surfaces", PhD thesis (Rheinisch-Westfälische Technische Hochschule Aachen, Aachen, 2007).

[157] H. Friedrich, *Scattering Theory*, 2nd ed. (Springer, Berlin Heidelberg, 2016).

[158] P. J. Braspenning, R. Zeller, P. H. Dederichs, and A. Lodder, "Electronic structure of non-magnetic impurities in Cu", *Journal of Physics F: Metal Physics* **12**, 105–124 (1982).

[159] G. Grimvall, *The Electron-Phonon Interaction in Metals*, Selected Topics in Solid State Physics 16 (North-Holland, Amsterdam New York Oxford, 1981).

[160] G. Rickayzen, *Green's Functions and Condensed Matter*, Reprint Edition (Dover, Mineola, New York, 2013).

[161] S. Engelsberg and J. R. Schrieffer, "Coupled Electron-Phonon System", *Phys. Rev.* **131**, 993–1008 (1963).

[162] A. Migdal, "Interaction Between Electrons And Lattice Vibrations In A Normal Metal", *Zh. Eksp. Teor. Fiz.* **34**, 1438 (1958).

[163] W. L. McMillan, "Transition Temperature of Strong-Coupled Superconductors", *Phys. Rev.* **167**, 331–344 (1968).

[164] N. A. Lanzillo, J. B. Thomas, B. Watson, M. Washington, and S. K. Nayak, "Pressure-enabled phonon engineering in metals", *PNAS* **111**, 8712–8716 (2014).

[165] S. K. Bose, "Electron–phonon coupling and spin fluctuations in 3d and 4d transition metals: implications for superconductivity and its pressure dependence", *J. Phys.: Condens. Matter* **21**, 025602 (2008).

[166] P. Hofmann, I. Y. Sklyadneva, E. D. L. Rienks, and E. V. Chulkov, "Electron–phonon coupling at surfaces and interfaces", *New J. Phys.* **11**, 125005 (2009).

[167] M. J. G. Lee, "Dynamical Properties of Quasiparticle Excitations in Metallic Copper", *Phys. Rev. B* **2**, 250–263 (1970).

[168] J. Gayone, C. Kirkegaard, J. Wells, S. Hoffmann, Z. Li, and P. Hofmann, "Determining the electron-phonon mass enhancement parameter λ on metal surfaces", *Appl. Phys. A* **80**, 943–949 (2005).

[169] P. M. Echenique, R. Berndt, E. V. Chulkov, T. Fauster, A. Goldmann, and U. Höfer, "Decay of electronic excitations at metal surfaces", *Surf. Sci. Rep.* **52**, 219–317 (2004).

[170] F. Reinert, G. Nicolay, S. Schmidt, D. Ehm, and S. Hüfner, "Direct measurements of the L-gap surface states on the (111) face of noble metals by photoelectron spectroscopy", *Phys. Rev. B* **63**, 115415 (2001).

[171] A. Tamai, W. Meevasana, P. D. C. King, C. W. Nicholson, A. de la Torre, E. Rozbicki, and F. Baumberger, "Spin-orbit splitting of the Shockley surface state on Cu(111)", *Phys. Rev. B* **87**, 075113 (2013).

[172] C. J. Arguello, E. P. Rosenthal, E. F. Andrade, W. Jin, P. C. Yeh, N. Zaki, S. Jia, R. J. Cava, R. M. Fernandes, A. J. Millis, T. Valla, R. M. Osgood, and A. N. Pasupathy, "Quasiparticle Interference, Quasiparticle Interactions, and the Origin of the Charge Density Wave in 2H-NbSe$_2$", *Phys. Rev. Lett.* **114**, 037001 (2015).

[173] M. P. Allan, K. Lee, A. W. Rost, M. H. Fischer, F. Massee, K. Kihou, C.-H. Lee, A. Iyo, H. Eisaki, T.-M. Chuang, J. C. Davis, and E.-A. Kim, "Identifying the 'fingerprint' of antiferromagnetic spin fluctuations in iron pnictide superconductors", *Nat. Phys.* **11**, 177–182 (2015).

[174] S. Choi, S. Johnston, W.-J. Jang, K. Koepernik, K. Nakatsukasa, J. M. Ok, H.-J. Lee, H. W. Choi, A. T. Lee, A. Akbari, Y. K. Semertzidis, Y. Bang, J. S. Kim, and J. Lee, "Correlation of Fe-Based Superconductivity and Electron-Phonon Coupling in an FeAs/Oxide Heterostructure", *Phys. Rev. Lett.* **119**, 107003 (2017).

[175] Z. Wang, D. Walkup, P. Derry, T. Scaffidi, M. Rak, S. Vig, A. Kogar, I. Zeljkovic, A. Husain, L. H. Santos, Y. Wang, A. Damascelli, Y. Maeno, P. Abbamonte, E. Fradkin, and V. Madhavan, "Quasiparticle interference and strong electron–mode coupling in the quasi-one-dimensional bands of Sr$_2$RuO$_4$", *Nat. Phys.* **13**, 799–805 (2017).

[176] P. Sessi, V. M. Silkin, I. A. Nechaev, T. Bathon, L. El-Kareh, E. V. Chulkov, P. M. Echenique, and M. Bode, "Direct observation of many-body charge density oscillations in a two-dimensional electron gas", *Nat. Commun.* **6**, 1–6 (2015).

[177] L. Vitali, M. A. Schneider, K. Kern, L. Wirtz, and A. Rubio, "Phonon and plasmon excitation in inelastic electron tunneling spectroscopy of graphite", *Phys. Rev. B* **69**, 121414 (2004).

[178] H. Gawronski, M. Mehlhorn, and K. Morgenstern, "Imaging Phonon Excitation with Atomic Resolution", *Science* **319**, 930–933 (2008).

[179] J. Lee, K. Fujita, K. McElroy, J. A. Slezak, M. Wang, Y. Aiura, H. Bando, M. Ishikado, T. Masui, J.-X. Zhu, A. V. Balatsky, H. Eisaki, S. Uchida, and J. C. Davis, "Interplay of electron–lattice interactions and superconductivity in Bi$_2$Sr$_2$CaCu$_2$O$_{8+\delta}$", *Nature* **442**, 546–550 (2006).

[180] N. Quaas, "Scanning Tunneling Microscopy of Co-impuried Noble Metal Surface: Kondo-Effect, Electronic Surface States and Diffusional Atom Transport", PhD thesis (Georg-August-Universität Göttingen, Göttingen, 2003).

[181] M. Schmid and P. Varga, "Segregation and surface chemical ordering - an experimental view on the atomic scale", in *Surface Alloys and Alloys Surfaces*, Vol. 10, edited by D. P. Woodruff, The Chemical Physics of Solid Surfaces (Elsevier, 2002), pp. 118–151.

[182] H. Walen, D.-J. Liu, J. Oh, H. J. Yang, P. M. Spurgeon, Y. Kim, and P. A. Thiel, "Sulfur Atoms Adsorbed on Cu(100) at Low Coverage: Characterization and Stability against Complexation", *J. Phys. Chem. B* **122**, 963–971 (2018).

[183] C. Nagl, E. Platzgummer, O. Haller, M. Schmid, and P. Varga, "Surface alloying and superstructures of Pb on Cu(100)", *Surf. Sci.* **331-333**, 831–837 (1995).

[184] G. Panaccione, J. Fujii, I. Vobornik, G. Trimarchi, N. Binggeli, A. Goldoni, R. Larciprete, and G. Rossi, "Local and long-range order of carbon impurities on Fe(100): Analysis of self-organization at a nanometer scale", *Phys. Rev. B* **73**, 035431 (2006).

[185] G. Trimarchi and N. Binggeli, "One-dimensional Fe surface states confined by self-assembled carbon chains at the Fe(001) surface", *Phys. Rev. B* **72**, 081408 (2005).

[186] G. Trimarchi and N. Binggeli, "One-dimensional surface states induced by segregated impurities at transition-metal surfaces", *Phys. Status Solidi B* **243**, 2105–2110 (2006).

[187] P. L. Rossiter, *The Electrical Resistivity of Metals and Alloys* (Cambridge University Press, Cambridge, 1987).

[188] S. Kasap, C. Koughia, and H. E. Ruda, "Electrical Conduction in Metals and Semiconductors", in *Springer Handbook of Electronic and Photonic Materials*, edited by S. Kasap and P. Capper, Springer Handbooks (Springer, Cham, 2017).

[189] A. Sommerfeld, "Zur Elektronentheorie der Metalle auf Grund der Fermischen Statistik", *Z. Physik* **47**, 1–32 (1928).

[190] L. Nordheim, "Zur Elektronentheorie der Metalle. I", *Annalen der Physik* **401**, 607–640 (1931).

[191] L. Nordheim, "Zur Elektronentheorie der Metalle. II", *Annalen der Physik* **401**, 641–678 (1931).

[192] A. L. Norbury, "The electrical resistivity of dilute metallic solid solutions", *Trans. Faraday Soc.* **16**, 570–596 (1921).

[193] I. Mertig, E. Mrosan, and P. Ziesche, *Multiple Scattering Theory of Point Defects in Metals: Electronic Properties* (Teubner, Leipzig, 1987).

[194] J. S. Galsin, *Impurity Scattering in Metallic Alloys* (Kluwer Academic/Plenum Publishers, New York, 2002).

[195] M. Schmid, S. Crampin, and P. Varga, "STM and STS of bulk electron scattering by subsurface objects", *J Electron Spectros Relat Phenomena* **109**, 71–84 (2000).

[196] I. Campillo, A. Rubio, J. M. Pitarke, A. Goldmann, and P. M. Echenique, "Hole Dynamics in Noble Metals", *Phys. Rev. Lett.* **85**, 3241–3244 (2000).

[197] E. Knoesel, A. Hotzel, and M. Wolf, "Ultrafast dynamics of hot electrons and holes in copper: Excitation, energy relaxation, and transport effects", *Phys. Rev. B* **57**, 12812–12824 (1998).

[198] N. Papanikolaou, R. Zeller, P. H. Dederichs, and N. Stefanou, "Lattice distortion in Cu-based dilute alloys: A first-principles study by the KKR Green-function method", *Phys. Rev. B* **55**, 4157–4167 (1997).

[199] T. Kotzott, "Signatur von Elektron-Phonon-Kopplung in STM-Spektren von nicht-magnetischen Atomen in Cu(111)", Bachelor's Thesis (Georg-August-Universität Göttingen, Göttingen, 2012).

[200] F. S. Khan, P. B. Allen, W. H. Butler, and F. J. Pinski, "Electron-phonon effects in copper. I. Electron scattering rate and mass enhancement", *Phys. Rev. B* **26**, 1538–1548 (1982).

[201] F. Reinert, B. Eltner, G. Nicolay, F. Forster, S. Schmidt, and S. Hüfner, "The electron–phonon self-energy of metallic systems determined by angular resolved high-resolution photoemission", *Physica B Condens. Matter* **351**, 229–234 (2004).

[202] J. Jiang, S. S. Tsirkin, K. Shimada, H. Iwasawa, M. Arita, H. Anzai, H. Namatame, M. Taniguchi, I. Y. Sklyadneva, R. Heid, K.-P. Bohnen, P. M. Echenique, and E. V. Chulkov, "Many-body interactions and Rashba splitting of the surface state on Cu(110)", *Phys. Rev. B* **89**, 085404 (2014).

[203] E. W. Plummer, J. Shi, S. .-J. Tang, E. Rotenberg, and S. D. Kevan, "Enhanced electron–phonon coupling at metal surfaces", *Prog. Surf. Sci.* **74**, 251–268 (2003).

[204] T. Balasubramanian, E. Jensen, X. L. Wu, and S. L. Hulbert, "Large value of the electron-phonon coupling parameter ($\lambda = 1.15$) and the possibility of surface superconductivity at the Be(0001) surface", *Phys. Rev. B* **57**, R6866–R6869 (1998).

[205] M. Hengsberger, D. Purdie, P. Segovia, M. Garnier, and Y. Baer, "Photoemission Study of a Strongly Coupled Electron-Phonon System", *Phys. Rev. Lett.* **83**, 592–595 (1999).

[206] S. LaShell, E. Jensen, and T. Balasubramanian, "Nonquasiparticle structure in the photoemission spectra from the Be(0001) surface and determination of the electron self energy", *Phys. Rev. B* **61**, 2371–2374 (2000).

[207] T. Chien, X. He, S.-K. Mo, M. Hashimoto, Z. Hussain, Z.-X. Shen, and E. W. Plummer, "Electron-phonon coupling in a system with broken symmetry: Surface of Be(0001)", *Phys. Rev. B* **92**, 075133 (2015).

[208] R. Li, J. Li, L. Wang, J. Liu, H. Ma, H.-F. Song, D. Li, Y. Li, and X.-Q. Chen, "Underlying Topological Dirac Nodal Line Mechanism of the Anomalously Large Electron-Phonon Coupling Strength on a Be(0001) Surface", *Phys. Rev. Lett.* **123**, 136802 (2019).

[209] I. Y. Sklyadneva, R. Heid, K.-P. Bohnen, and E. V. Chulkov, "Electron–phonon coupling in the surface electronic states on Pd(111)", *New J. Phys.* **11**, 103038 (2009).

[210] M. Kralj, A. Šiber, P. Pervan, M. Milun, T. Valla, P. D. Johnson, and D. P. Woodruff, "Temperature dependence of photoemission from quantum-well states in Ag/V(100): Moving surface-vacuum barrier effects", *Phys. Rev. B* **64**, 085411 (2001).

[211] D.-A. Luh, T. Miller, J. J. Paggel, and T.-C. Chiang, "Large Electron-Phonon Coupling at an Interface", *Phys. Rev. Lett.* **88**, 256802 (2002).

[212] J. J. Paggel, D.-A. Luh, T. Miller, and T.-C. Chiang, "Electronic-Structure Dependence of the Electron-Phonon Interaction in Ag", *Phys. Rev. Lett.* **92**, 186803 (2004).

[213] S. Mathias, M. Wiesenmayer, M. Aeschlimann, and M. Bauer, "Quantum-Well Wave-Function Localization and the Electron-Phonon Interaction in Thin Ag Nanofilms", *Phys. Rev. Lett.* **97**, 236809 (2006).

[214] T. L. Yu, R. Peng, 2. M. Xu, W. T. Yang, Y. H. Song, C. H. P. Wen, Q. Yao, X. Lou, T. Zhang, W. Li, X. Y. Wei, J. K. Bao, G. H. Cao, P. Dudin, J. D. Denlinger, V. N. Strocov, H. C. Xu, and D. L. Feng, "Colossal band renormalization and stoner ferromagnetism induced by electron-antiferromagnetic-magnon coupling", *arXiv:2011.05683 [cond-mat]* (2020).

Danksagung

Herzlich bedanken möchte ich mich bei allen, die zum Gelingen dieser Arbeit beigetragen und mich in der Zeit der Promotion unterstützt und begleitet haben.

Zunächst gilt mein großer Dank PD Dr. Martin Wenderoth, in dessen Arbeitsgruppe ich in Masterarbeit und Promotion an zwei unterschiedlichen und spannenden Projekten 'auf der atomaren Skala' arbeiten konnte. Ich danke herzlich für die gute Betreuung und die zahllosen Diskussionen über Physik und darüber hinaus. Sie haben mein Verständnis von physikalischen Fragestellungen tief geprägt und mit ihren Denkanstößen immer wieder neue Perspektiven eröffnet.

Herzlich bedanken möchte ich mich zudem bei Prof. Dr. Christian Jooß für das Erstellen des Zweitgutachtens sowie gemeinsam mit Prof. Dr. Peter Blöchl für die Begleitung meines Promotionsvorhabens im Betreuungsausschuss. Ich danke ebenfalls den weiteren Mitgliedern meiner Prüfungskommission Prof. Dr. Fabian Heidrich-Meisner, Prof. Dr. Hans Hofsäss, Prof. Dr. Stefan Mathias sowie Prof. Dr. Vasily Moshnyaga.

Des Weiteren möchte ich mich bei meinen Kollaborationspartnern bedanken, die ebenfalls die nicht-magnetischen Störstellen untersucht haben: Herzlichen Dank an Dr. Mohammed Bouhassoune und Prof. Dr. Samir Lounis für die gute Zusammenarbeit rund um die Ab-initio-Simulationen. Ebenfalls herzlicher Dank gilt Dr. Henning Prüser für die Möglichkeit, in dieser Arbeit auf die Daten von Silber-Störstellen aufbauen zu können.

Mein großer Dank gilt zudem Bernhard Spicher für seine technische Expertise und die kompetente Unterstützung in allen Angelegenheiten rund ums UHV, was für den Alltag im Labor von unermesslichem Wert ist.

Allen aktuellen und ehemaligen Mitgliedern der Arbeitsgruppe möchte ich für die schöne Zeit und freundschaftliche Atmosphäre danken, die ich in den vergangenen Jahren erleben durfte. Neben der guten Zusammenarbeit und der stets großen Hilfsbereitschaft, mit einer helfenden Hand oder guten Idee auch ein anderes Projekt voranzubringen, möchte ich mich für die unterhaltsame Gemeinschaft bedanken, sei

Acknowledgements

es beim gemeinsamen Mensa-Besuch, in der Kaffeepause, beim Grillen, oder wenn sich die Messungen in den Abend verlängert haben. Insbesondere seien erwähnt Ole, Thomas, Anna, Georg, Benjamin, Philip, Philipp, Philipp, Tim, Alexandra, Benno, Jan, Judith, Katharina, Lisa, Marlo, Máté, Simeon, Steffen und Terence. Ebenfalls herzlichen Dank an die Kolleginnen und Kollegen aus dem IV. Physikalischen Institut!

Meinen Korrekturlesern Malte Vassholz, Ole Bunjes und Anna Sinterhauf ein herzliches Dankeschön!

Ebenfalls vielen Dank an Rasit Kösker und das Team der Elektronikwerkstatt für ihre kompetente und zuverlässige Unterstützung, insbesondere bei allen Fragen rund um die Messelektronik. Außerdem danke ich den Teams der feinmechanischen Werkstätten sowie der Zentralwerkstatt. Für die findige Lösung für jede Art von bürokratischer Fragestellung danke ich Antje Spliethoff-Laiser.

Der Deutschen Forschungsgemeinschaft danke ich für die finanzielle Unterstützung im Rahmen des Projekts WE 1889/8-1.

Meinen Freunden in Göttingen und in der Ferne möchte ich von Herzen dafür danken, die Zeit von Studium und Promotion zu einer mit vielen schönen Momenten und Erinnerungen gemacht zu haben.

Zuletzt gilt mein großer Dank meiner Familie. Insbesondere möchte ich mich bei meinen Eltern bedanken, die mich auf meinem bisherigen Weg stets begleitet haben und auf deren Unterstützung ich mich immer verlassen konnte.